NASA/CR-20240005899

Extended Investigation into Fault-Tolerant Integrated Motor Drive for a Quadrotor Urban Air Mobility (UAM) Aircraft

Thomas M. Jahns and James A. Swanke III
University of Wisconsin–Madison, Madison, Wisconsin

July 2024

NASA STI Program Report Series

Since its founding, NASA has been dedicated to the advancement of aeronautics and space science. The NASA scientific and technical information (STI) program plays a key part in helping NASA maintain this important role.

The NASA STI program operates under the auspices of the Agency Chief Information Officer. It collects, organizes, provides for archiving, and disseminates NASA's STI. The NASA STI program provides access to the NTRS Registered and its public interface, the NASA Technical Reports Server, thus providing one of the largest collections of aeronautical and space science STI in the world. Results are published in both non-NASA channels and by NASA in the NASA STI Report Series, which includes the following report types:

- TECHNICAL PUBLICATION.
  Reports of completed research or a major significant phase of research that present the results of NASA Programs and include extensive data or theoretical analysis. Includes compilations of significant scientific and technical data and information deemed to be of continuing reference value. NASA counterpart of peer-reviewed formal professional papers but has less stringent limitations on manuscript length and extent of graphic presentations.

- TECHNICAL MEMORANDUM.
  Scientific and technical findings that are preliminary or of specialized interest, e.g., quick release reports, working papers, and bibliographies that contain minimal annotation. Does not contain extensive analysis.

- CONTRACTOR REPORT.
  Scientific and technical findings by NASA-sponsored contractors and grantees.

- CONTRACTOR REPORT.
  Scientific and technical findings by NASA-sponsored contractors and grantees.

- CONFERENCE PUBLICATION.
  Collected papers from scientific and technical conferences, symposia, seminars, or other meetings sponsored or co-sponsored by NASA.

- SPECIAL PUBLICATION.
  Scientific, technical, or historical information from NASA programs, projects, and missions, often concerned with subjects having substantial public interest.

- TECHNICAL TRANSLATION.
  English-language translations of foreign scientific and technical material pertinent to NASA's mission.

Specialized services also include organizing and publishing research results, distributing specialized research announcements and feeds, providing information desk and personal search support, and enabling data exchange services.

For more information about the NASA STI program, see the following:

- Access the NASA STI program home page at http://www.sti.nasa.gov

NASA/CR-20240005899

Extended Investigation into Fault-Tolerant Integrated Motor Drive for a Quadrotor Urban Air Mobility (UAM) Aircraft

Thomas M. Jahns and James A. Swanke III
University of Wisconsin–Madison, Madison, Wisconsin

Prepared under Contract 80NSSC22k1726

National Aeronautics and
Space Administration

Glenn Research Center
Cleveland, Ohio 44135

July 2024

Acknowledgments

The authors wish to express their appreciation to the many people who were instrumental in the development of this Contractor Report. We especially want to thank Linda Taylor, Thomas Tallerico, Timothy Krantz, Mark Valco, Patrick Hanlon, David Sadey, and Nuha Nawash, all from NASA Glenn Research Center. We also wish to express our appreciation to Patrick Darmstadt from The Boeing Company and Hao Zeng, Xiaoyuan Zhang, Ken Chen, Kyle Hanson, and Pia Strampp from University of Wisconsin–Madison.

This work was sponsored by the Advanced Air Vehicles Program at the NASA Glenn Research Center.

Level of Review: This material has been technically reviewed by NASA expert reviewer(s).

This report is available in electronic form at https://www.sti.nasa.gov/ and https://ntrs.nasa.gov/

NASA STI Program/Mail Stop 050
NASA Langley Research Center
Hampton, VA 23681-2199

Executive Summary

Electric propulsor machines and their associated power electronics have been identified in past studies as low-reliability components in emerging Urban Air Mobility (UAM) Vertical Takeoff and Landing (VTOL) vehicles that raise their predicted catastrophic failure rates. This research effort extends previously presented work investigating the use of fault-tolerant (FT) motor drives in quadrotor aircraft as a promising approach to significantly increase their mean-time-to-failure (MTTF). In particular, fault-tolerant *modular* motor drives (FT-MMDs) are identified as strong candidates for closing the electric propulsor reliability gap. These FT-MMDs divide a machine drive into multiple redundant modules, each consisting of three-phase stator windings and power electronics units, enabling continued machine operation after a module failure. Achieving the highest possible isolation between modules (physical, magnetic, thermal, electrical) is critically important in FT-MMDs to prevent the propagation of any failure between modules. Key additional requirements for achieving the highest possible reliability characteristics with FT-MMDs are high repair rates and aggressive suppression of all single-point failures.

Previously-reported research carried out by the authors developed the design of a four-module 70 kW machine for a quadrotor aircraft application, utilizing specialized electromagnetic and thermal isolation features between modules. Electromagnetic isolation features include the use of stator yoke cavities and modified stator tooth tips to prevent magnetic interactions between phases. In-slot cooling is utilized to achieve high levels of power density and to thermally isolate each winding coil from adjacent coils. This FT-MMD architecture was evaluated under a variety of machine and power electronics faults to assess its reliability characteristics. These faults include terminal three-phase open- and short- circuit faults applied to module terminals. Short-circuit faults are more severe, and the presented analysis shows the developed FT-MMD can withstand continuous short-circuit current with minimal demagnetization and safe post-fault operating temperatures. The results of this preceding research are briefly summarized in this report.

Higher severity faults have also been evaluated for inclusion in this report, including winding internal turn-to-turn faults that pose particularly high risks for permanent magnet (PM) machines. Analytical and simulation results show the machine's isolation features protect healthy phases and modules from the thermal impact of these failures on a transient basis, providing sufficient time for fault detection to activate the suppression of high circulating currents in the faulted phase turns. Finally, open- and short-circuit faults in the power electronics have been assessed. Fault responses with voltage-source inverters (VSIs) and current-source inverters (CSIs) have been compared, highlighting the advantages of CSIs for suppressing high fault currents in PM machine drives following short-circuit failures of individual inverter switch devices.

The FT-MMD thermal and electromagnetic isolation features were evaluated at both megawatt and low-power (<10 kW) levels to evaluate scalability. The results show that the electromagnetic and thermal isolation features scale well to both high and low power levels. However, the in-slot cooling technique loses effectiveness at high power levels due to well-known geometric scaling laws that result in poor heat transfer to the coolant. In contrast, the low-power FT-MMD study showed that in-slot cooling effectiveness can be retained using simplified schemes such as readily-available thermally-conductive ceramic tubes.

A low-power 7 kW FT-MMD demonstrator unit was fabricated and tested under a variety of conditions. Robust isolation and fault response characteristics were confirmed after applying three-phase terminal open- and short-circuit faults. Controllable internal turn-to-turn faults were also applied to the machine, confirming the demo unit's desirable transient thermal isolation capabilities. The experimental results exhibited close agreement with models, validating the technical soundness of the proposed FT-MMD architecture.

Finally, a set of FT figures of merit (FoMs) were developed that enable high-level quantitative comparisons of alternative FT motor drive topologies. These include metrics that evaluate reliability

benefits offset by performance penalties, as well as FoMs quantifying reliability dependence on key parameters such as repair rates. Enhanced mathematical tools for rapidly assessing the FoM metrics using Markov chains are derived. The value of these FT-FoMs is demonstrated using a case study that compares several FT topologies. The results confirm the strong potential of FT-MMDs to address the identified UAM reliability gap by combining increased levels of modularity, high repair rates, and the eradication of single-point-failure sources.

Contents

List of Acronyms and Symbols

Acronym	Description
CSI	Current Source Inverter
EM	Electromagnetic
FEA	Finite Element Analysis
FoM	Figure of Merit
FSCW	Fractional Slot Concentrated Winding
FT	Fault Tolerance
IMD	Integrated Motor Drive
IMMD	Integrated Modular Motor Drive
IPM	Interior Permanent Magnet
MIR	Module Isolation Ratio
MMD	Modular Motor Drives
MTTF	Mean Time to Failure
NASA	National Aeronautics and Space Administration
PE	Power Electronics
PM	Permanent Magnet
PMSM	Permanent Magnet Synchronous Machine
OC	Open Circuit
SC	Short Circuit
SP	Single Point
SPM	Surface Permanent Magnet
UAM	Urban Air Mobility
VSI	Voltage Source Inverter
VTOL	Vertical Takeoff and Landing
λ	Failure rate [1/hours]
μ	Repair Rate [1/hours]

Extended Investigation into Fault-Tolerant Integrated Motor Drive for a Quadrotor Urban Air Mobility (UAM) Aircraft

Thomas M. Jahns and James A. Swanke III
University of Wisconsin–Madison
Madison, Wisconsin 53706

1.0 Introduction

Lightweight and reliable machine-drives are critical for emerging electrified aircraft such as the six-passenger quadcopter aircraft illustrated in Figure 1-1(a). However, recent reliability studies in References 1 and 2 have highlighted the fact that conventional electrical machines and drives have typical failure rates several orders of magnitude higher than the 10^{-9} failures/hour target for catastrophic failures of commercial wide-body aircraft defined by Reference 3 and illustrated in Figure 1-1(b).

Poor propulsor reliability can be addressed in several ways such as the introduction of a mechanical cross-shaft or redundant propulsors (Figure 1-1(a)) that enable continued flight after the loss of a propulsor. Alternatively, fault-tolerance (FT) features can be incorporated into the propulsor machine-drive itself, decoupling the failure-rates of the motor drive from those of the overall aircraft.

More specifically, FT machine-drives allow for continued machine operation after the failure of machine windings or power electronics. The implementation of FT can take numerous forms, several of which are discussed in the six-passenger quadcopter context in Reference 4. Overall, FT machine-drives have three-basic requirements: (1) current limiting features to limit fault currents in the event of a failure—especially critical for permanent magnet synchronous machines (PMSMs); (2) redundant power-flow channels to the propulsor which can take the form of redundant motor drives, windings, or phase legs allowing for continued operation after failure; and (3) isolation between power-flow channels. Isolation takes the form of physical, thermal, magnetic, and galvanic isolation between redundant channels.

The use of modular motor drives (MMD) is a promising approach to realize FT, where the stator and power electronics are divided into modular three-phase winding and power electronics sectors as shown in Figure 1-1(c), enabling superior fault-coverage and weight tradeoffs compared to direct-redundant configurations. In the event of a failed module, the remaining healthy modules increase their current output to maintain torque.

This final report is an extension of an earlier study report (Ref. 4) in which the topic of power-dense FT motor drives is a central topic. A detailed four-module quadcopter motor drive design utilizing new forms of electromagnetic and thermal isolation is presented in Reference 4 and used as a baseline to study MMD propulsor reliability. This final report elaborates on the presented design fault response discussed in the earlier study report and experimentally validates the presented concepts. In addition, this report presents the results of studies into the power-scalability of the developed isolation features, as well as metrics for generating comparisons between FT topologies.

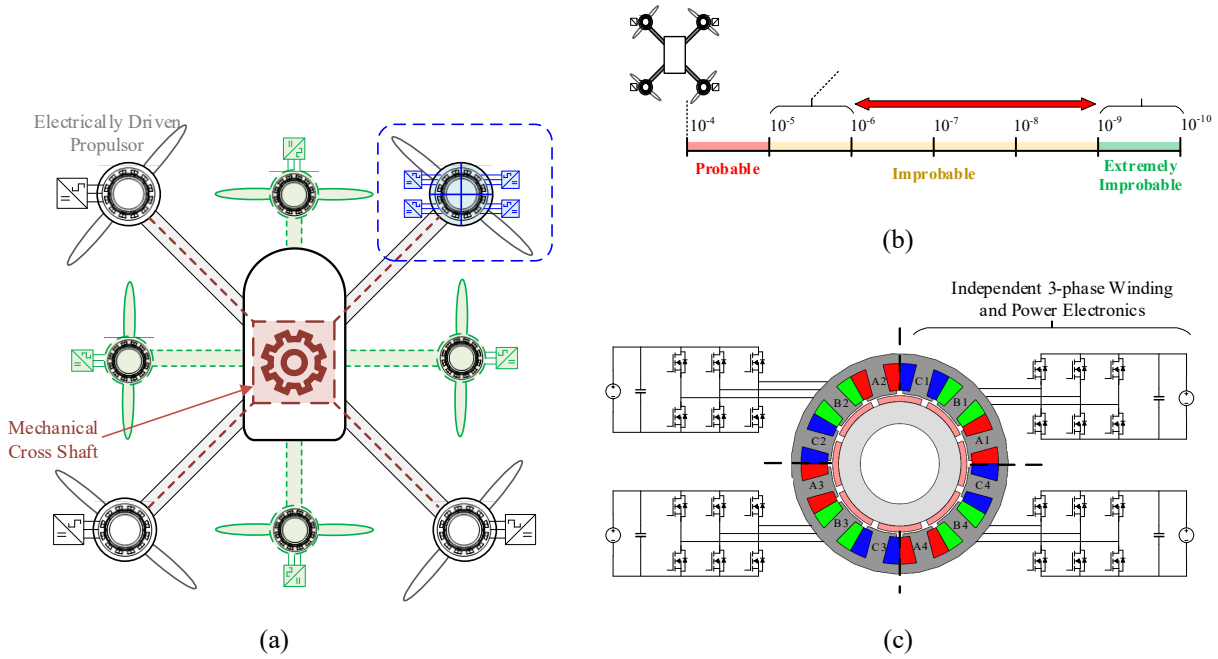

Figure 1-1.—(a) Baseline quadrotor propulsor architecture with variants highlighted: propulsor cross shafting (red), redundant propulsor (green), and modular fault-tolerant propulsors (blue); (b) failure rate continuum with propulsor motor drive reliability gap highlighted; (c) example of modular motor drive proposed for use in fault-tolerant propulsors.

1.1 Quadcopter Fault-Tolerant Propulsor Evaluation

Quadrotor machine-drive study conclusions from the earlier report (Ref. 4) are summarized here for convenience. First, the results of a study of various commonly used modular PMSM FT motor drive implementations was presented considering tradeoffs between machine performance, isolation, and power densities. These include single-layer, multi-phase, spacer-tooth, and conventional flux barrier implementations. Overall, the study identified substantial performance and power-density penalties using conventional techniques.

Alternative forms of magnetic and thermal isolation were considered to reduce the observed FT power-density tradeoff. The Modular Isolation Ratio (MIR) is the primary metric that was defined for assessing magnetic isolation (i.e., measure of relative electromagnetic coupling between phases and modules) as follows:

$$\mathrm{MIR} = \frac{\max(\lambda_m)}{\lambda_s} = \frac{M_{lkg} + M}{L} \tag{1.1}$$

with mutual coil flux linkage λ_m and self coil flux linkage λ_s. Equivalently, the MIR can be represented by mutual leakage and synchronous inductances M_{lkg} and M, and total self-inductance L.

The selected alternative magnetic isolation approach is illustrated in Figure 1-2. Specifically, the special selection of slot-pole combination, the introduction of flux-barriers between phases in the back-iron, and the removal of inter-phase tooth tips allows the use of double-layer windings with negligible mutual coupling between phases (MIR < 3 percent). The intra-phase tooth magnetics that carries the magnetic flux highlighted in Figure 1-2 with the red dashed lines is sized to ensure that the machine winding has sufficient inductance to limit short-circuit currents.

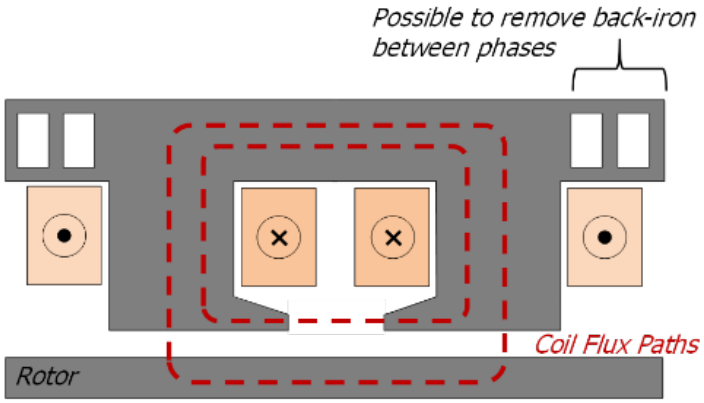

Figure 1-2.—Single phase representation of developed magnetic isolation approach where machine flux linkage is localized preventing mutual coupling between phases.

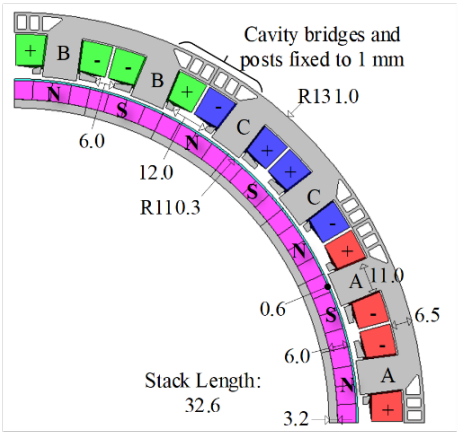

(a)

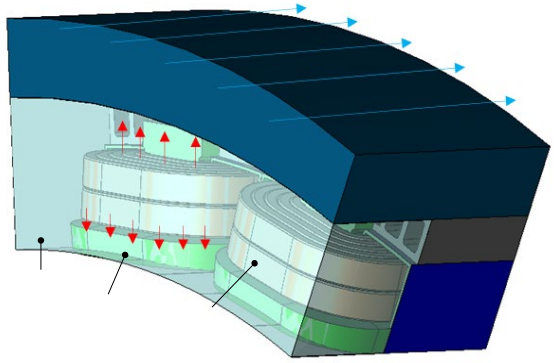

(b)

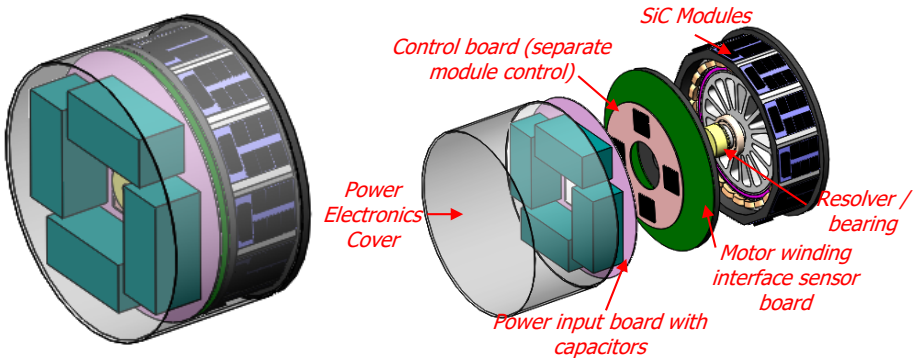

(c)

Figure 1-3.—Developed quadrotor modular motor drive: (a) single electromagnetic module (of four) with isolation features and dimensions; (b) stator thermal management system; and (c) power electronics integration scheme.

This developed magnetic isolation approach was applied to a 70 kW rated machine for a quadrotor application. This machine features fractional-slot, concentrated windings (FSCW) with 24-slots and a surface permanent magnet (SPM) rotor with 28-poles utilizing a Halbach magnet array. Key machine dimensions and electromagnetic features are shown in Figure 1-3(a). Overall, the active power density of the machine is 14.1 kW/kg at peak continuous power, achieving the objective electromagnetic weight for the quadcopter application.

Critical to the developed design is its thermal management system shown in Figure 1-3(b). This design uses in-slot cooling channels embedded in a coil bobbin and a thermally conductive potted channel from the machine end windings to the stator cooling jacket, which is shared with integrated power electronics. The combination of thermal features used in this stator cooling design was critical for realizing the desired power density.

The modular power electronics were developed using paralleled silicon-carbide switches in a baseline 2-level voltage source inverter (VSI). Each of the four modular VSIs is connected in series at their dc links to reduce the voltage stress on each module. The power electronics are integrated into the machine, enabling shared cooling in the integrated modular motor drive (IMMD) configuration shown in Figure 1-3(c). This design achieved a predicted full-load drive efficiency of 98.4 percent and overall system efficiency of 94.3 percent.

The developed motor drive model was evaluated for three-phase terminal faults on the modules. This included both three-phase open- and short-circuit fault scenarios. The results showed that the machine is fully capable of operation after a terminal level failure. Furthermore, the IMMD is capable of maintaining full torque by increasing the current in the remaining healthy modules with the penalty of reduced thermal margins inside the stator. Further details about the machine fault modes are provided in this report.

The detailed machine design in Figure 1-3 provided the foundations for deeper investigations of machine component healthy and faulted stressors which are needed to inform a reliability analysis. Markov chain analysis was selected as the tool of choice to perform the reliability analysis, defining healthy, faulted, and failed states based on the identified failure modes. Failure rate data was collected from component datasheets and from the literature and modified to consider the evaluated stresses. These failure rates were used to investigate transitions between healthy, faulted, and failed states. The system repair rate, or expected time to respond to a module fault, was also considered as a variable. In totality, the values of these variables enable the calculation of the Mean Time to Failure (MTTF) for the IMMD system.

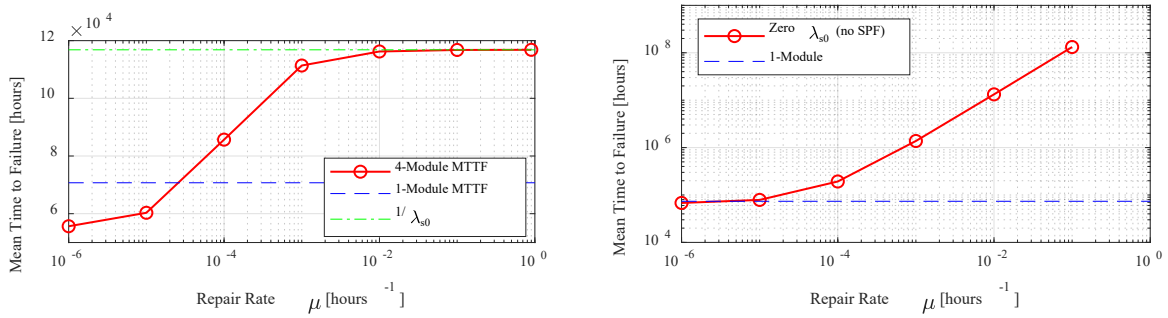

(a) (b)

Figure 1-4.—Summary of Markov chain reliability study results with variable repair rates: (a) baseline four-module IMMD; and (b) MTTF with single-point failure removed.

Select results from the completed reliability study are highlighted in Figure 1-4 for variable repair rate. The results in Figure 1-4(a) show that modularity in combination with a high repair rate can realize a 65 percent increase in the system MTTF compared to a baseline single-module motor drive. Furthermore, the study showed the upper bound of the MTTF is capped by the single point failure rate, yielding the relationship:

$$\mathrm{MTTF}_{\mu\to 1} = \frac{1}{\lambda_{s0}} \tag{1.2}$$

The key result in Equation (1.2) highlights a general strategy for improving reliability of modular systems: reducing the response time to module failures, and mitigating all single point failures to the maximum possible extent. The effectiveness of this strategy is illustrated in Figure 1-4(b) for which all single point failures are eliminated, resulting in a massive 1000x increase in the system MTTF that identifies a promising pathway for closing the identified reliability gap.

1.2 Report Objectives

The objectives of this report extend those defined in Reference 4, and can be categorized in three overarching topics:

Obj. #1: *Investigate proposed modular machine configurations under the most demanding fault conditions*. Original evaluations of the developed quadrotor machine focused on the terminal level faults and associated response. This study is extended to consider other types of terminal faults as well as alternative fault modes including turn-to-turn faults.

Obj. #2: *Comparative evaluation of alternative fault-tolerant motor drive concepts.* Comparative metrics for FT systems found in the literature are minimal. This study has generated a new set of metrics that allows users to perform high-level comparisons of different types of FT implementations.

Obj. #3: *Experimental demonstration of most promising modular motor drive concepts.* This project has experimentally demonstrated both magnetic and thermal isolation techniques that were described in the above quadcopter propulsor machine drive.

1.3 Report Structure and Scope

This report is structured to address the objectives presented in Section 1.2. Section 2.0 provides a more detailed summary of the described quadcopter machine, with a focus on new analyses covering the IMMD fault characteristics. This includes investigations into rotor demagnetization, stator turn-to-turn failures, and switch open- and short-circuit failures. Finally, considerations for alternative implementations of the modular machine are considered including the current source inverter (CSI) which has offers improved FT characteristics.

Section 3.0 provides deeper insights into the developed quadcopter machine by considering the scaling characteristics of the developed thermal and stator isolation features. This includes consideration of a 2 MW rated machine intended for larger commercial aircraft, as well as a smaller 7 kW rated machine that takes into consideration practical limitations of the developed features. A low-power demonstrator version of FT modular motor drive has been fabricated and tested, with design details and experimental results presented in Section 4.0.

New Figure of Merit (FoM) metrics for comparing FT motor drives are provided in Section 5.0 that attempt to capture the tradeoffs between increased reliability (e.g., MTTF) and performance metric penalties that can include component overrating and increased weight. Additionally, analytical formulations for MTTF are provided, enabling direct calculation of the presented FT-FoMs. Finally, an abbreviated case study is presented to illustrate the usefulness of these FoM metrics.

This report concludes with a summary of key conclusions related to FT motor drives for aerospace applications.

2.0 Four-Module Integrated Modular Machine Drive (IMMD) for a Quadcopter Evaluation

The analysis presented for the FT motor drive described in Reference 4 is briefly summarized and extended to consider broader fault modes and effects. The reader is referred to the original report for deeper discussions on the machine and power electronics analyses. New insights provided in this report include studies surround demagnetization, turn-to-turn faults, and switch failures.

2.1 Selected Motor drive Architecture and Features

The developed quadrotor specifications are developed in consultation with NASA. The primary operating point of interest is the machine corner point which occurs at 8,000 rev/min and 70 kW shaft output power—or 83.6 N-m. These specifications must exceed a target power density of 13.3 kW/kg active mass. From a fault-tolerance perspective, the IMMD is expected to continue operation after the failure of a maximum of two modules as illustrated in Figure 2-1. The IMMD is expected to deliver full torque after a single module failure.

A MMD architecture is selected to meet the FT specifications shown in Figure 2-1. Further, a double-layer FSCW stator with a SPM rotor topology is selected due to inherent low mass characteristics. A 24-slot 28-pole stator topology is chosen due to its inherent localized phase flux path shown in Figure 1-2. Magnetic isolation features are introduced to the stator including modified tooth tips flux barriers as highlighted in Figure 1-2. Cobalt-iron VAC48 laminations are assumed for the stator and rotor cores due to high saturation flux and low-loss capability. Samarium-Cobalt Recoma 35E is assumed for the magnets due to good balance between temperature capability, remanence, and coercivity. Rectangular litz wire is assumed for the machine windings to minimize AC loss effects.

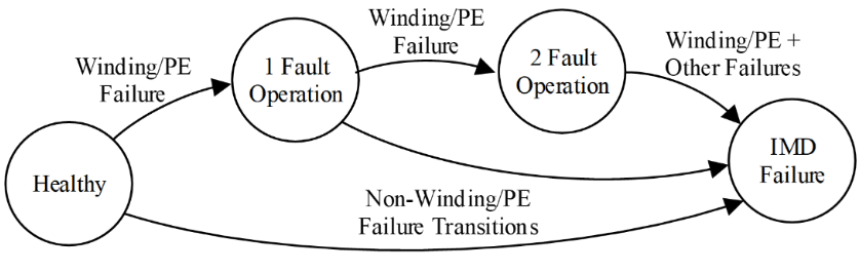

Figure 2-1.—Specified fault tolerance operation state diagram for developed quadcopter motor drive system.

Thermal isolation between phases is achieved using in-slot cooling and specialized insulation design. The use of in-slot cooling is critical for the selected design, allowing for higher machine current density and therefore smaller stator slots. Specifically, a thermally conductive alumina bobbin is assumed as shown in Figure 1-3(b), allowing for direct cooling of the windings. The entire stator is potted using a thermally conductive two-part epoxy to improve the thermal characteristics of the winding and the heat transfer to the bobbin.

A single machine module is shown in Figure 2-2 including the VSI power electronics. Each module is connected in series, reducing the voltage requirements per module. In the event of a module failure, the failed module is bypassed with its voltage redistributed to the remaining healthy module.

2.2 Healthy Performance Characteristics

Machine sizing equations and 2D electromagnetic finite element analysis (FEA) are used to optimize the machine electromagnetics. Machine final performance is assessed using 3D FEA with full-load flux contours shown in Figure 2-3, indicating high levels of saturation in the implemented flux barriers. This high saturation contributes to elevated core loss. Overall machine losses equal 2.96 kW. Power electronics are modeled using PLECs with overall drive losses of 1.14 kW, leading to an overall system efficiency of 94.3 percent. A breakdown of MMD losses is given in Figure 2-3(b), showing stator winding losses contribute to 58 percent of the machine overall loss.

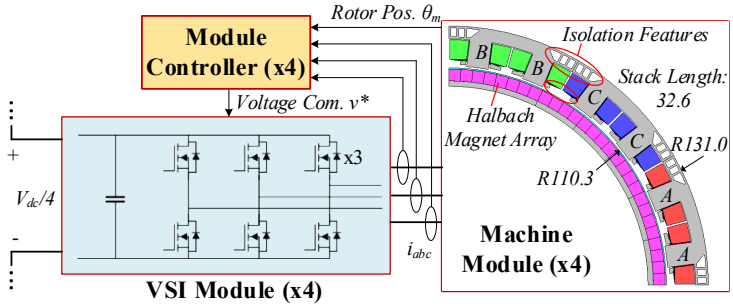

Figure 2-2.—Developed quadcopter IMMD single module and machine dimensions in millimeters.

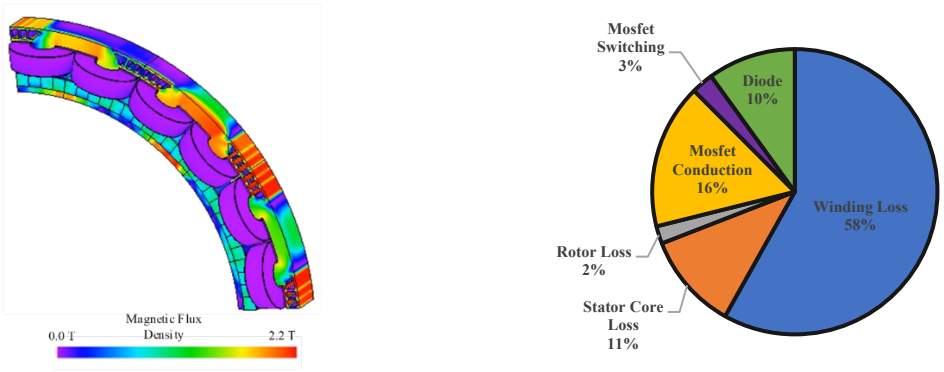

(a) (b)

Figure 2-3.—Healthy MMD characteristics: (a) full-load flux density contours; and (b) full-load loss component loss distribution.

In-slot cooling is used to manage the significant level of machine loss as indicated in Figure 2-3(b). Litz wire turns are homogenized as described in Reference 5 to achieve equivalent thermal conductivities for the 3D thermal FEA model. Heat transfer coefficients on wetted surfaces are estimated using internal flow correlations and assume 80 °C fluid. Winding temperature results for full-load stator losses (2.3 kW in the windings) and 33 percent overloaded conditions (2.9 kW in the windings) are given in Figure 2-4. Maximum coil temperatures are 156 °C for healthy conditions and 204 °C for overloaded conditions.

The two-coil thermal model shown in Figure 2-4 is used to assess the thermal isolation of the proposed in-slot cooling method. The model is modified to assign a faulted and healthy coil. The faulted coil loss is increased relative to the healthy coil and the change in healthy coil temperature is monitored. Initial isolation study results show only a 6 °C temperature rise in healthy coil maximum temperature for nearly 2x increase in faulted coil loss.

2.3 Terminal-Fault Response

The designed motor drive system must be capable of full-torque operation after a module failure. The general response to any failure is to bypass the module dc link followed by either open-circuiting or short-circuiting the module machine windings depending on the nature of the failure. Machine performance under both terminal fault conditions is considered with steady-state flux density contours shown in Figure 2-5 for single module open- or short-circuited and increased healthy module current (by a factor of 4/3 or 33 percent) to maintain operating torque. This overloading comes at the expense of decreased thermal margins as highlighted in the thermal FEA contours in Figure 2-4.

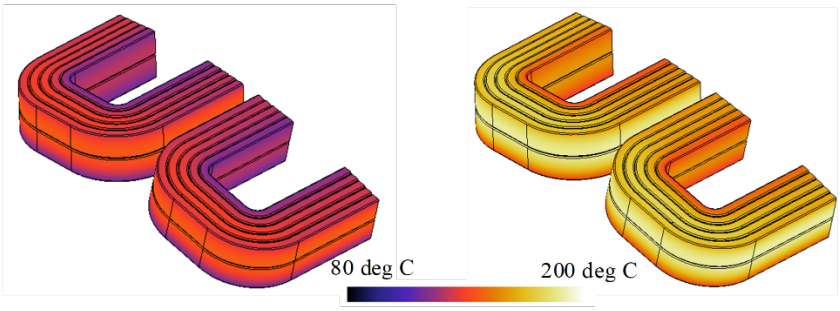

Figure 2-4.—Predicted steady-state coil temperature contours for healthy (left) and overloaded coil conditions. Predict maximum temperature of 156 and 204 °C for healthy and overloaded conditions, respectively.

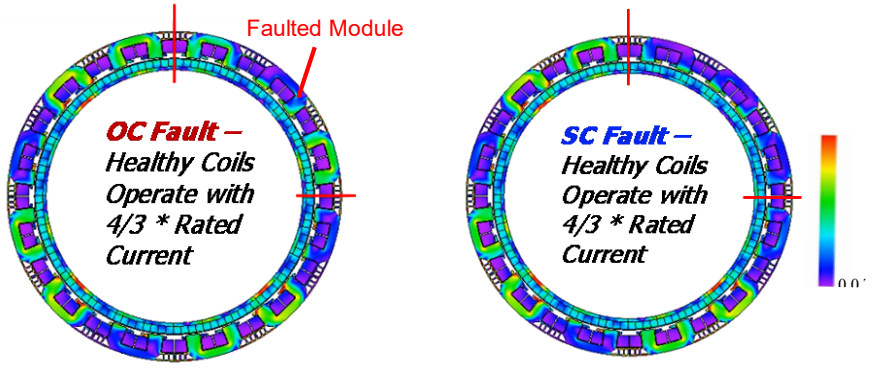

Figure 2-5.—Steady state magnetic flux density contours for open and short-circuit failures with maintained output torque.

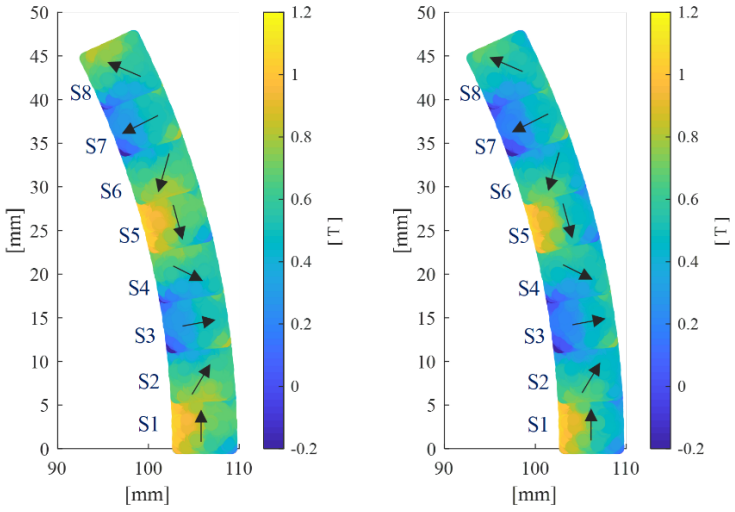

Figure 2-6.—Demagnetization study results with minimum magnet flux density contours shown in the direction of the magnet-segment magnetization for a Recoma 35E magnet at 200 °C: (a) healthy conditions with i_q = 126.2 A and i_d = 0.0 A; and (b) faulted conditions with i_q = 0.0 A and i_d = –252.4 A.

A quadrant arrangement is assumed for the modular FT machine shown in Figure 2-5 which offers convenient placement of coils per module and improved isolation due to fewer point of contact between module windings. However, this arrangement comes with post-fault tradeoffs where an unbalanced magnetic pull (UMP) is developed due to magnetic asymmetries. For the cases described in Figure 2-5, a single module failure results in a dc-offset and 2x electrical frequency force on the rotor and stator which can contribute to premature bearing failure. Further discussion regarding this UMP can be found in the original report (Ref. 4).

Another fault mode of the developed FT quadrotor machine is demagnetization of the rotor magnets after a fault. To simulate a fault scenario, FEA was used to apply simulated fault currents of 2x rated current to the negative d-axis of the machine, and the resulting magnet demagnetization was observed and compared to a healthy operation scenario. Figure 2-6 compares minimum magnet flux densities in localized areas across the magnet cross-sectional surface over the course of a fundamental cycle in the direction of the magnetization for both healthy and faulted scenarios. If the flux density is less than the knee point of the magnet (approximately –0.2 T for Recoma 35E magnet at 200 °C) then the associated element is considered partially demagnetized.

Even under healthy conditions, a small amount demagnetization is observed at the inner corners of the S3 and S7 magnet segment shown in Figure 2-6(a). This demagnetization region increases slightly during the fault scenario, although the demagnetized area is small compared to the total magnet cross-sectional area.

2.4 Turn-to-Turn Fault Response

The previous section focused on relatively benign terminal faults, but there are other machine fault modes that can lead to catastrophic failures. In particular, internal turn-to-turn faults in the stator windings can be especially damaging to PMSMs. It is necessary to develop turn-to-turn fault models for the quadrotor FT machine to assess the possibility of fault propagation and to establish fault detection requirements for a turn-to-turn fault scenario.

Due to the severity of the turn-to-turn failure, numerous papers have been published on the modeling of this type of fault (Refs. 6 to 10). An analytical turn-level model of the developed quadrotor machine is presented to aid with the evaluation process. This model has been validated using electromagnetic FEA.

2.4.1 Analytical Turn-to-Turn Fault Model

Based on the developed design, only a single machine phase needs to be analyzed due to the electromagnetic isolation between the phases. Each machine coil and phase can be modeled based on turn, sub-turns, and fault paths as shown in Figure 2-7(a). Each turn segment has a back-emf, inductance, and resistance associated with it. This coil can be rolled out to form a developed model with each turn modeled as a lumped element as shown in Figure 2-7(b). An internal turn-to-turn fault occurs when a connection is formed between turns, which can result in substantial current in the faulted turns and localized heating.

Many of the surveyed turn-to-turn fault papers use lumped turn and coil models, like the one shown in Figure 2-7, to estimate fault current levels. This type of approach is inflexible as new models need to be developed for different faulted turn locations. The model used to study turn-to-turn faults in the quadrotor machine shares similarities with the model in Figure 2-7(b), but it has been generalized to provide greater flexibility for analyzing different fault locations and winding configurations. Specifically, fault resistances are inserted between every turn-node as shown in Figure 2-8. The value of these resistances can be adjusted to assess the winding during both healthy or turn-to-turn fault conditions.

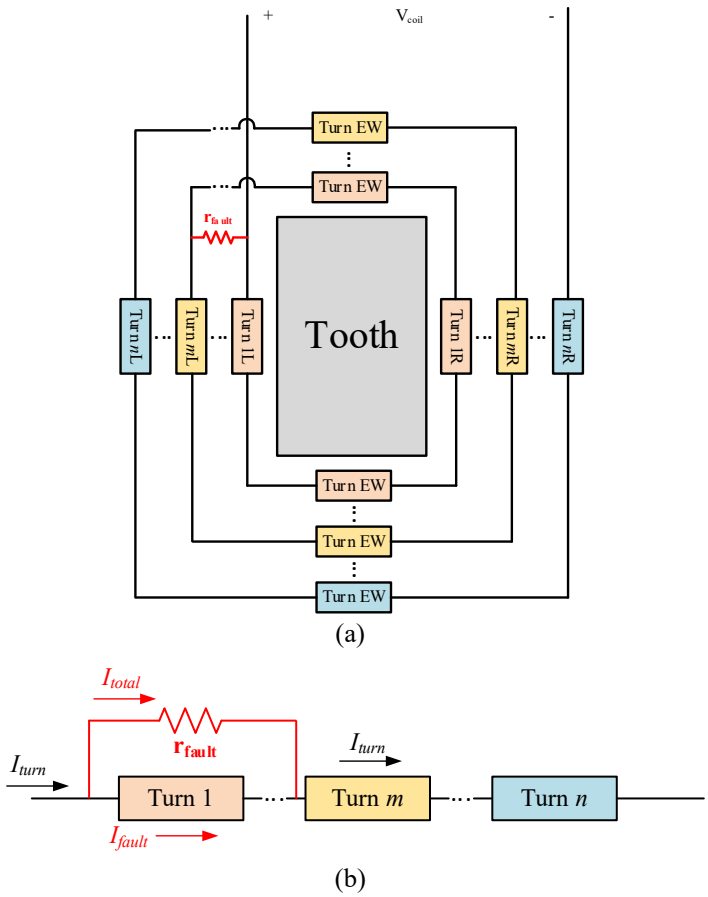

Figure 2-7.—Isolated phase model with a turn-to-turn fault: (a) phase model with coils modeled on the turn and sub-turn level; and (b) rolled out model with lumped turns and fault currents defined.

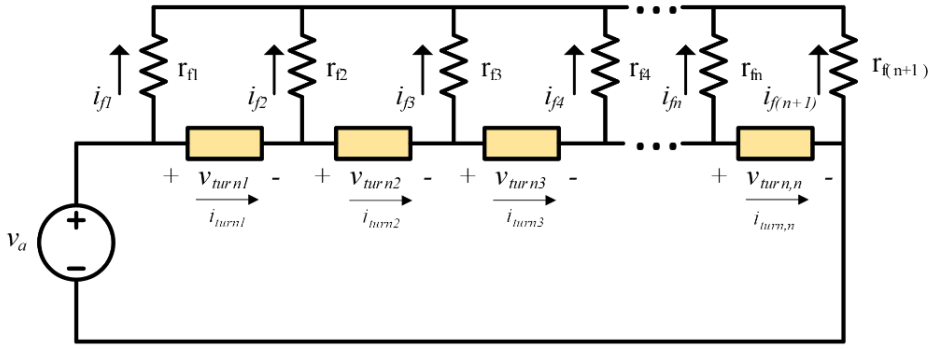

Figure 2-8.—Isolated phase turn-to-turn fault model.

A system of equations can be developed to describe the Figure 2-8 circuit. There are n voltage-loop equations resulting from Kirchoff's Voltage Law (KVL), one associated with each of the n turns in the machine in Equation (2.1), which resemble a traditional machine model with turn resistance r_s, turn inductances L_{mk}, and turn magnet flux linkage λ_{pm}. The quadrotor machine has 20 turns per phase with each turn being modeled as a 0.935 mΩ resistance with approximately 0.41 mWb magnet flux linkage. In addition, each turn has a self and mutual inductance of approximately 2.5 μH. Once again, the ρ operator represents the time derivative d/dt.

$$v_{\text{turn},m} = r_s \cdot i_{\text{turn},m} + \sum_{k=1}^{n} \left(L_{mk} \cdot \rho \cdot i_{\text{turn},k} \right) + \rho \cdot \lambda_{\text{pm},m} \tag{2.1}$$

Anther n-1 equations are needed to express Kirchhoff's Current Law (KCL) at each of the turn nodes consisting of turn currents i_{turn} and fault current i_f.

$$0 = i_{fm} + i_{\text{turn},m} + \ldots + i_{\text{turn},m-1} \tag{2.2}$$

And one final equation is generating by applying KCL at the common fault-path node:

$$0 = i_{f1} + i_{f2} + \ldots + i_{f(n+1)} \tag{2.3}$$

These equations have been implemented in MATLAB Simulink and results for a single-turn fault are shown here (specifically, shorting turn-1 via r_{f1} and r_{f2} in Figure 2-8). Fault resistances for healthy turns are set to 1 MΩ. In this single-turn fault example, the total fault resistance R_f is defined by

$$R_f = r_{f1} + r_{f2} \tag{2.4}$$

Steady-state healthy (e.g., i_{turn2}) and faulted (i_{turn1}) turn currents for given fault path resistances are shown in Figure 2-9. For sufficiently high fault resistance (R_f = 10 kΩ), there is little difference in current between healthy and faulted sections. Interestingly, the faulted-turn current drops relative to the healthy current for a 100 mΩ fault resistance R_f, but the fault current increasingly exceeds the healthy turn current as the fault resistance is progressively reduced. This result reaffirms previous observations in the literature that the fault resistance has a significant impact on the expected fault current.

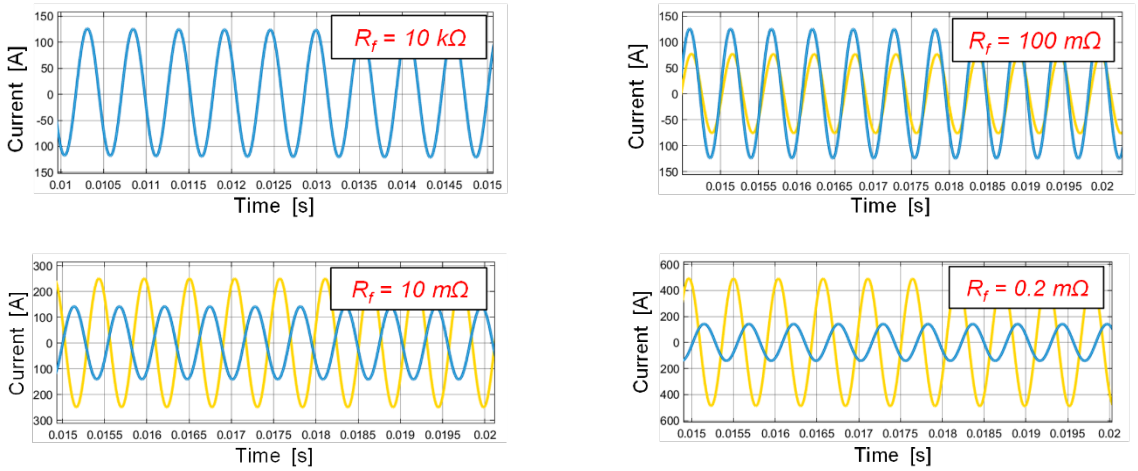

Figure 2-9.—Simulated healthy (blue, i_{turn2}) and faulted (yellow, i_{turn1}) currents for varying fault resistance levels for single turn fault at 8,000 rpm.

2.4.2 FEA Validation of Turn-to-Turn Fault Model

A turn-level electromagnetic FEA model of the quadrotor machine has been developed to validate the analytical turn-to-turn fault model as shown in Figure 2-10. A single fault resistance R_f is placed in parallel to turn-1 in the FEA model circuit. This resistance is varied and the turn-fault (i_{turn1}) and fault resistance current (i_{f1}) is calculated. Results from the FEA are compared against the developed model calculation in Figure 2-11.

The results show reasonable agreement for high levels of fault resistance (i.e., under healthy conditions). For small fault resistance values (e.g., 1e-6 Ω), the developed analytical model underestimates the fault resistance current by 34 A or 5.9 percent compared to the FEA model. For medium fault resistances (1e-3 to 1 Ω), the Figure 2-11 curves agree in terms of shape and both models show a dip in turn-fault currents. However, the FEA model results appear shifted compared to the analytical model. The differences in results can likely be attributed to approximated machine parameters.

2.4.3 Thermal Isolation During Turn-to-Turn Fault Event

I^2R losses in the faulted turn and resistance can be estimated using the calculated currents and the specified resistances. Calculated losses associated to the analytical model for a single-turn short-circuit fault are plotted in Figure 2-12 and show that the losses in the fault-resistance can be considerable. Specifically, a fault-resistance loss of around 1000 W is expected at a 10 mΩ fault resistance level. Significant losses are expected in the faulted turn during a complete short scenario (i.e., $R_f = 0$ Ω) with losses exceeding 100 W.

The developed stator thermal models described in a previous section can be reapplied and modified to assess the turn losses during a complete turn-to-turn short scenario. The model has been modified to carry out a transient thermal analysis, and increased losses are applied to a single turn as shown in Figure 2-13. A more complicated model is required to include the concentrated heat flux associated with the fault-resistance.

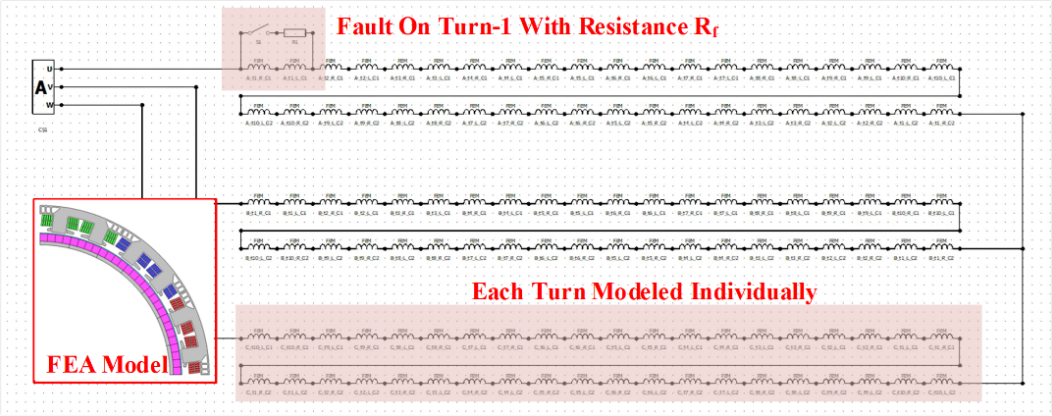

Figure 2-10.—Turn-level electromagnetic FEA circuit model showing turn-1 fault.

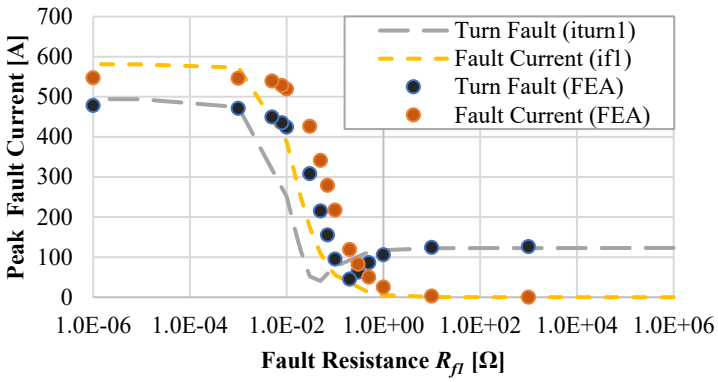

Figure 2-11.—Developed single-turn fault model with variable resistance fault currents compared against FEA model for a single-turn short circuit.

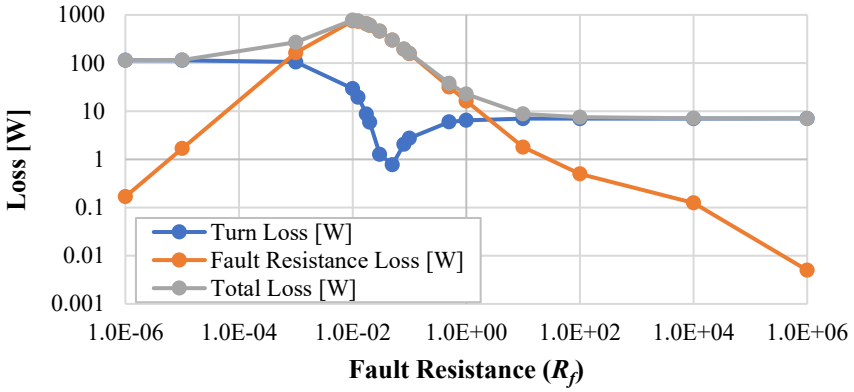

Figure 2-12.—Faulted turn and fault resistance losses for varying fault resistances R_f.

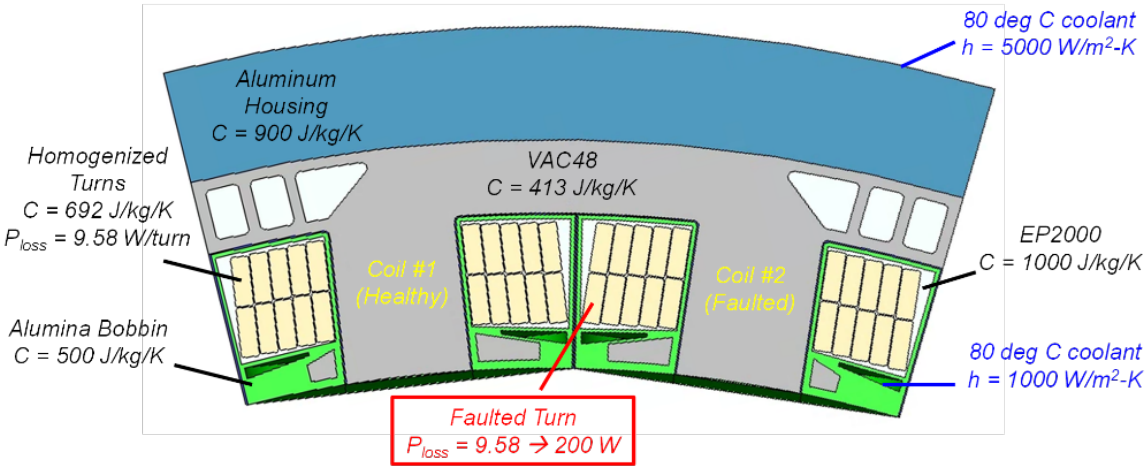

Figure 2-13.—Transient thermal study model parameters.

As suggested by Figure 2-13, the loss in the assigned faulted turn was varied from its loss value during rated healthy operation (~9 W) up to 200 W to simulate the faulted turn loss in a dead-short scenario. Transient maximum coil temperatures for faulted turn losses values of 40 W (~4x rated), 100 W (~10x rated), and 200 W (~20x rated) are provided in Figure 2-14. For a 40 W turn-loss condition, both the healthy and faulted coil maximum temperatures reach steady state below the 200 °C insulation limit, although the faulted coil peak temperature is near 180 °C which places it in the vicinity of the maximum safe operating temperature for the wire insulation.

Next, the 100 W turn-loss condition shows the faulted-coil maximum-temperature exceeding the insulation temperature rating of the machine by approximately 40 °C after a minute, which may be acceptable for short-time durations. A gradual increase in the healthy coil temperature is also observed, but it is below the insulation temperature limit for the plotted time scale up to 60 s. Similar observations can be made for the 200 W turn-loss condition, albeit on a shorter timescale. Specifically, the maximum faulted coil temperature approaches 290 °C at 20 s, while the temperature of the healthy coil reaches approx. 165 °C after 20 s, still within the insulation's maximum temperature limit.

The results in Figure 2-14 suggest that the developed stator slot structure and cooling method can thermally isolate healthy coils on short timescales, providing time for triggering a turn-to-turn fault detection scheme and remedial response (e.g., three-phase short circuit application to the faulted module terminals). However, the large change in the faulted coil temperature will raise the value of the faulted turn resistance and the expected heat load. More complex models are needed to account for the changing temperature of the faulted turn and to incorporate the concentrated loss associated with the fault resistance.

2.5 Switch Failure Response

Machine fault modes have been the primary source of discussion in the previous subsections. This subsection considers switch fault modes which manifest as either open or short circuits. Primary switch failure discussions surround a VSI model shown in Figure 2-15(a) though discussions around the CSI in Figure 2-15(b) are provided due to idealized fault response to shorted switches (Refs. 11 and 12). A summary of CSI and VSI comparisons and tradeoffs in given in Table 2-1.

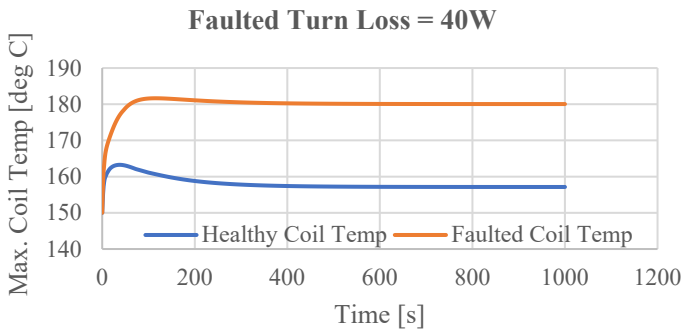

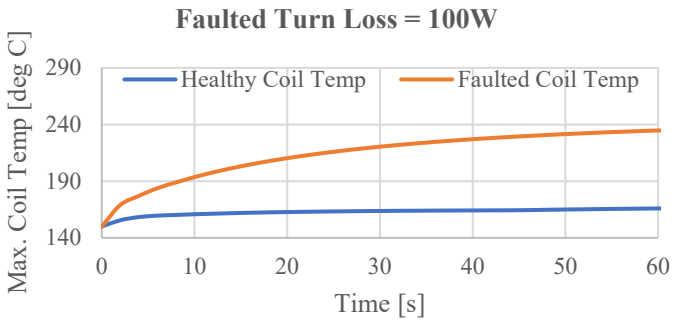

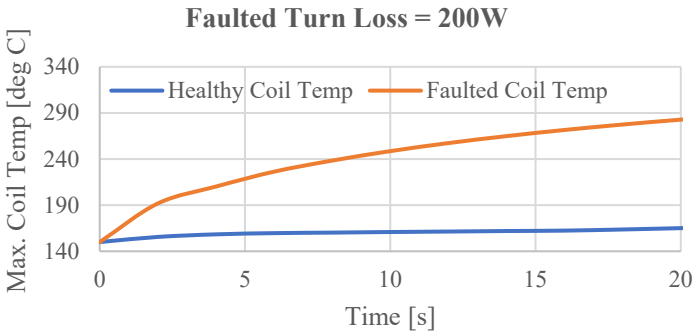

Figure 2-14.—Transient thermal study for varying levels of faulted turn losses.

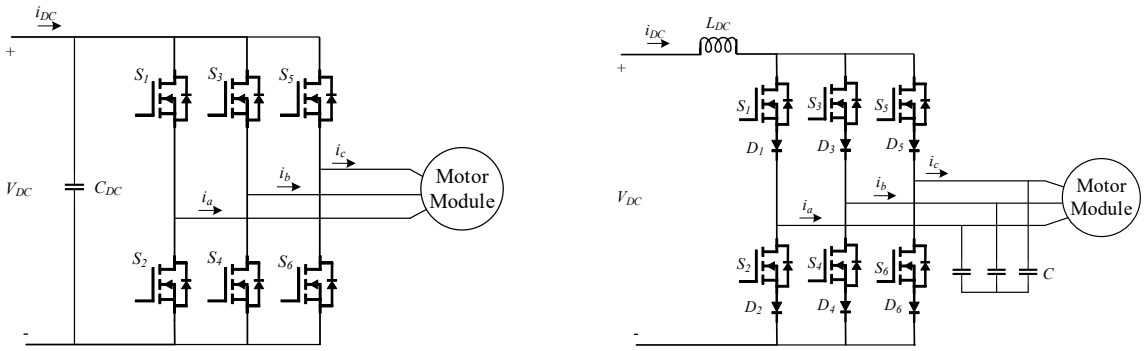

(a) (b)

Figure 2-15.—VSI converter model (a), and CSI converter model (b).

TABLE 2-1.—COMPARISON BETWEEN VSI AND CSI

Comparison	VSI	CSI
Output Filtering	dv/dt filtering often required to minimize voltage overshoot and insulation stress (LC filter)	Small output terminal capacitors are sufficient to deliver smooth sinusoidal output voltage and current waveforms
EMI	Common-mode EMI suppression typically requires addition of LC filters at the 3 output phase terminals	DC bus inductor serves as low-pass filter in combination with output capacitors to suppress common-mode EMI
Switching Frequency	- Higher SF reduces capacitor size, though often limited by capacitor current - dv/dt issues with faster switching	Higher SFs using WBG switches are critical for minimizing passive component mass and volumes
Output Voltage	Maximum output voltage limited by DC bus voltage (buck)	Inherent boost capability
Device Availability	SiC or GaN MOSFET devices readily available	Monolithic RB switches are unavailable; currently requires either series MOSFET-diode or 2 MOSFETS in anti-series
Temperature/Robustness	Film capacitors for dc link typically limited to 125 °C	Inductors are rugged and capable of 200+ °C operation
Additional Components	Output LC filters often required to prevent serious voltage overshoot at machine terminals	- DC link switch can reduce losses in 6 CSI switch switches - Series diode or MOSFET added for RB capability
Switch SC Fault	VSIs are highly vulnerable to serious SC faults that will demagnetize motor magnets if only one VSI switch fails short	Absence of anti-parallel diode in CSI switches makes it much less vulnerable to serious SC faults than VSI
Switch OC Fault	Significantly less dangerous than SC fault, but still troublesome due to presence of anti-parallel switch diodes	Little risk of motor or inverter damage with proper protection features

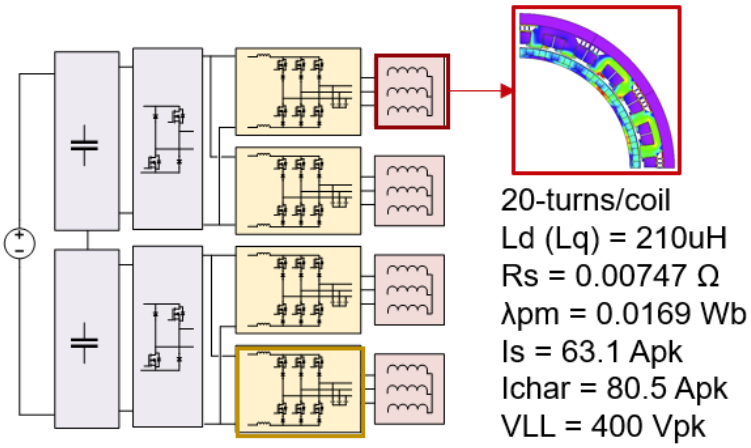

Figure 2-16.—Two-series two-parallel CSI modular connection with modified machine module parameters.

2.5.1 Modified Module Connections

The series connected module configuration described in Section 2.1 is modified to allow for better CSI component sizing (e.g., dc link inductor, etc.). As such, a two-series two-parallel modular configuration is adopted as shown in Figure 2-16 for a CSI design. The machine must be modified to accommodate the new connection scheme resulting in a doubling in the number of turns per coil (20 turns total) and reduced phase currents. No change to the core or magnet geometry is necessary. Adjusted module parameters are summarized in Figure 2-16. To minimize CSI passive components the switching frequency is doubled from the VSI configuration to 54 kHz.

The VSI design is modified to assume the same two-series two-parallel connection for better comparisons between the VSI and CSI. Further, increasing the parallelism in the machine has benefits reducing the phase currents of the machine and improving the power electronics conduction losses highlighted in Figure 2-3(b).

2.5.2 VSI Switch Failure and Response

The developed VSI PLECS model is modified to allow for the implementation of short- and open-circuit switch faults (switch S_1 in Figure 2-15(a)). A switch open-circuit failure is the most benign failure mode for the VSI. During this failure mode the ideal response to open the remaining switches. This process is illustrated in Figure 2-17 for a single module where the fault response is assumed to occur 1 ms after the initial failure. Immediately after the failure, only two-phase currents flow resulting in a substantial torque ripple until the fault response opening all remaining module switches.

The more insidious failure mode for the VSI is the switch short circuit. An open-circuit fault response is shown in Figure 2-18(a). After the failure a major current transient is observed. Apply an open circuit on the remaining switches results in phase currents continuing to flow and substantial torque ripple. Most prominent on the faulted phase, a persistent dc current offset is observed.

The better response to this type of failure is shorting all remaining healthy switches in the module (or all upper or lower switches) in Figure 2-18(b). Similar to the previous case, a large current and torque ripple transient is observed. However, after the application of a short-circuit, the machine characteristic current flows in the module producing a small drag torque with minimal ripple. In general, a short-circuit response is the preferred VSI response to most stator and power electronics failures.

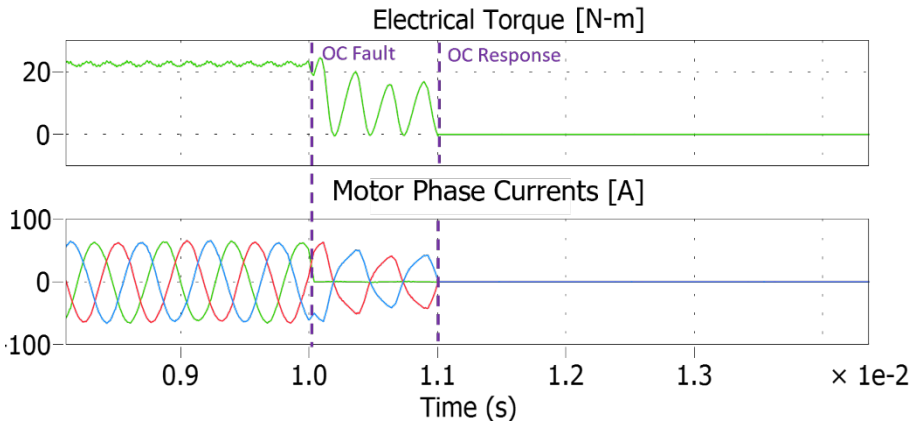

Figure 2-17.—VSI OC switch failure and response.

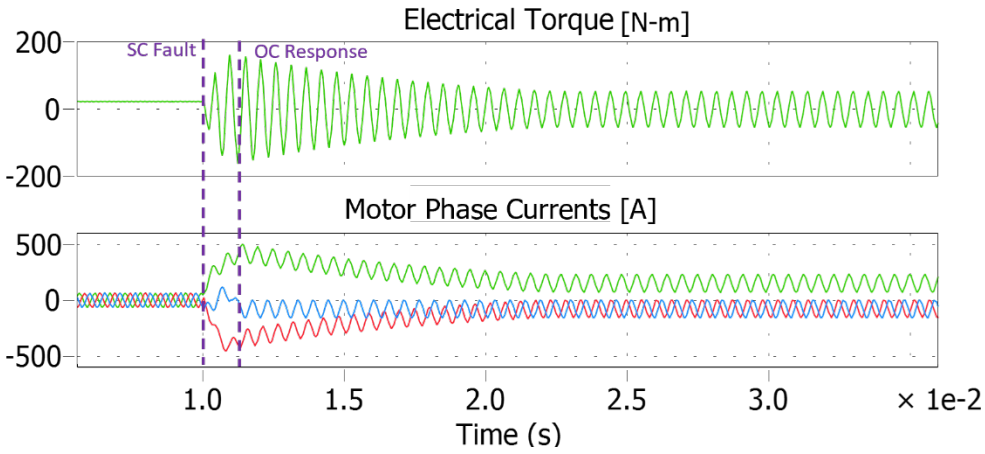

(a)

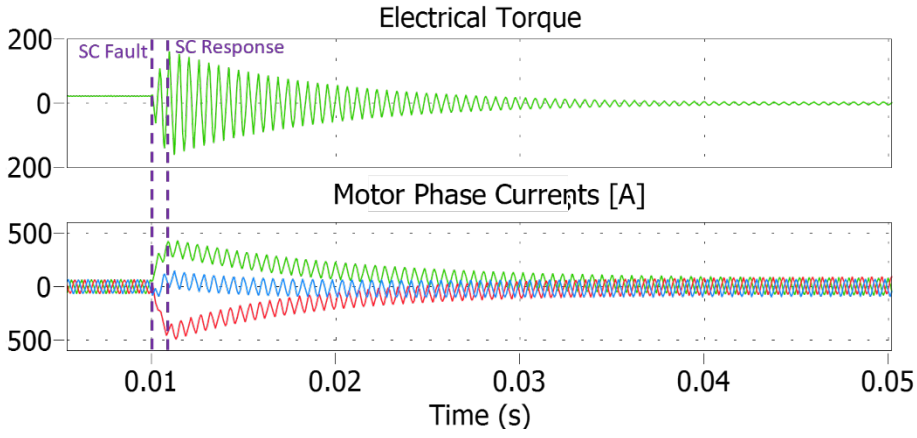

(b)

Figure 2-18.—VSI switch short-circuit response: (a) healthy switches open circuit; and (b) healthy switches short circuit.

2.5.3 CSI Switch Failure Response

The developed PLECS model was modified to match the CSI model shown in Figure 2-15(b), using a series connected diode to block reverse polarity currents. CSI passive components (dc link inductors) have been sized using the sizing equations provided in Reference 13 resulting in a dc link inductance of 81.7 μH and output filter capacitance of 9.3 μF. The dc link current shown in Figure 2-15(c) was selected to match the characteristic current of the module (80.5 A) to suppress transient currents related to the switch short-circuit fault mode.

The results of the simulated CSI response to a short-circuit switch failure including the torque and phase current are provided in Figure 2-19. Compared to the VSI short-circuit scenario, a much smaller transient current peak is observed immediately after the failure due to the selected dc link current level. After the fault, the CSI phase currents exhibit minimal current transients compared to the VSI, quickly transitioning to safe current amplitudes only modestly higher than the rated machine current. The module torque drops

The more serious fault mode for the CSI is a circuit open-circuit fault caused by either a switch or diode device. This failure could result in major voltage spikes across devices unless special circuitry is added to protect against overvoltage events. This can take the form of a dc link inductor crowbar circuit that immediately redirects the dc link current into a path where it can safely decay to zero after an OC failure occurs.

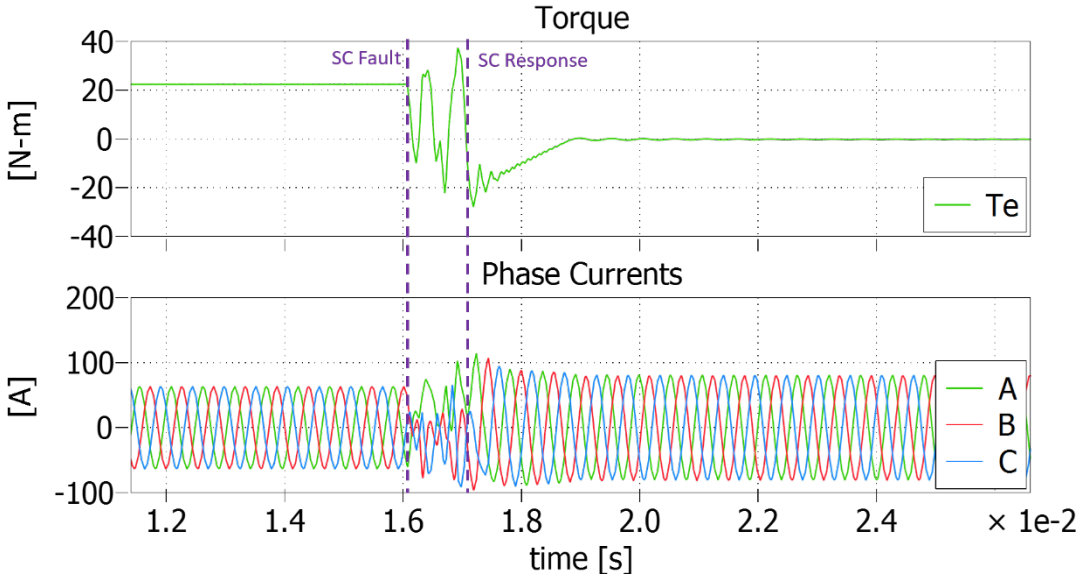

Figure 2-19.—CSI switch short-circuit failure and terminal short-circuit response.

2.6 Summary

A brief review of the proposed FT motor drive for a quadcopter application described previously in Reference 4 is presented, highlighting key features and performance characteristics. This includes re-introducing specialized isolation features such as back-iron cavities and modified tooth-tips, as well as the selected in-slot cooling method. Machine performance and terminal fault characteristics are summarized.

The previous analysis in Reference 4 has been expanded to consider additional fault modes of the presented MMD. This includes investigation of possible rotor demagnetization after a fault event. The results indicate minimal expected demagnetization as well as the capability of withstanding significant transient currents after a failure. Next, an analytical model for estimating turn-to-turn fault failures has been developed and applied to the quadrotor machine. This analytical model predicts fault currents that are very similar to those predicted by finite element analysis, but differing slightly due to the machine parameter estimation.

This developed model enables the estimation of fault-related losses that are subsequently applied to a transient thermal model. This model predicts very large increases in the faulted winding temperature during a turn-to-turn fault. However, the model also shows that the developed in-slot cooling method provides effective transient thermal isolation characteristics for the adjacent healthy winding. This transient thermal isolation provides sufficient time for a turn-to-turn fault detection scheme to identify the fault and take remedial action before the healthy winding overheats.

Finally, switch fault modes have been investigated for the developed power electronics. This evaluation was carried out for a modified modular configuration consisting of two-series, two-parallel modules (replacing the previous four-series-modules configuration). The evaluation shows that open-circuit faults are the most benign fault type for the VSI. Alternatively, short-circuit failures can result in massive current transients producing major torque ripple. This fault response is contrasted with the simulated response of a CSI implementation that exhibits and appealing capability of suppressing the current transients during a switch short-circuit fault.

3.0 Fault-Tolerant Machine Features Scalability

The power scalability of the developed magnetic and thermal isolation features presented in the preceding section are evaluated for both megawatt-scale and low-power (<10 kW) machine designs. A four-module 2 MW-rated fractional-slot, concentrated winding (FSCW) machine is presented that is designed to meet the direct-drive aerospace propulsion requirements defined by ARPA-E in Reference 14. The power-density sizing equations presented in Reference 4 are applied to provide initial machine dimensions, which are further optimized using electromagnetic finite element analysis (FEA). A final electromagnetic machine design is presented along with FEA results. Magnetic and thermal isolation is assessed using FEA.

The second half of this section focuses on the design of a 7 kW rated two-module demonstrator utilizing the developed isolation features. This design applies practical considerations to the machine design (flux barrier and in-slot cooling design) in preparation for later fabrication and testing of this machine (see Section 4.0 for details). The tradeoffs associated with this cooling system are discussed, extending beyond the design of the coolant channel itself.

3.1 Megawatt-Scale Scalability

The scalability of the developed electrical and thermal isolation features is studied for conceptual megawatt power machine for aerospace propulsion. Machine requirements and characteristics are defined followed by magnet and thermal FEA results, including evaluations of magnetic isolation capability. For

brevity specific design and performance steps will be neglected in favor of focus on results due to commonality with the steps presented in Section 2.0. Differing from the Section design, post-fault capability or derating is not considered to focus on general scaling trends. Finally, result discussions are stator-focused due to the nature of the developed isolation technique.

3.1.1 Megawatt Propulsion Requirements and Sizing

Requirements for the 2 MW machine study are guided by the ongoing ARPA-E ASCEND research program (Ref. 14). High level specifications based on ASCEND program target and selected system design requirements are provided in Table 3-1. For comparison, these are contrasted against the 1 MW rated machine from the NASA ULI program discussed (Ref. 15). To achieve FT capability, the developed MMD is assumed to have four-modules like the quadrotor machine described in Section 2.0. Requirements related to the machine-propulsor integration are neglected.

The power density targets defined in Table 3-1 are more aggressive than the NASA ULI program. Achieving this level of power density is further complicated by the direct-drive speed requirement, four times lower than the NASA ULI program. Besides speed, machine materials (CoFe laminations, etc.) and rotor topology are held constant. Other commonalities include machine target metrics like shear stress and tip speed and magnetic loading. Flexibility in machine pole-count is allowed in order to utilize a slot-pole combination that fits the four-module topology, the selected magnetic isolation approach, and similar operating fundamental frequency. Ultimately the 48-slot, 40 pole (SPP = 2/5) topology is selected meeting all of these criteria.

Details related to the magnetic design are shared in the following subsection with system level results related to the defined specifications given here. Key machine metrics after the machine sizing and 3D FEA study is summarized in Table 3-2. Notably, the torque average torque given in Table 3-2 is slightly lower than the spec in Table 3-1 taking into account machine end effects. Relatedly, the presented active power density is lower than the spec in Table 3-1 due to lower output torque related to end-effects and higher machine saturation—items not captured in the generalized sizing equations in Reference 4.

None the less, the developed isolated 2 MW design still reaches active power density levels comparable to the NASA ULI machine. This is not surprising since similar key metrics like tip-speed and shear stress are held constant. Differences in current density and slot fill factor reflect the decisions related to the differing in-slot cooling methods. Overall, the developed 2 MW machine it is a suitable representation of a megawatt-rated machine for aerospace propulsion and is used to evaluate the developed isolation features. A rendering of the developed design and its slot layout is provided in Figure 3-1.

TABLE 3-1.—SELECTED 2 MW MACHINE SPECIFICATIONS AND NASA ULI PROGRAM COMPARISONS

Specification	Isolated 2 MW Concept	NASA ULI Machine	Units
Max. Power	2,000	1,000	kW
Speed	5,000	20,000	RPM
Torque	3819	477.5	N-m
DC Bus Volt/Module	1,100	667	V
Min. Assembled Power Density	20	----	kW/kg
Active Power Density Target	30	22.7	kW/kg
Module Number	4	6	---------
Stator Cooling Method	Cooling Bobbin and Stator Jacket	Flooded Stator and Cooling Jacket	---------
Rotor Topology	Radial Flux SPM	Radial Flux SPM	---------

TABLE 3-2.—COMPARISON OF FINAL 2 MW CONCEPT AGAINST NASA ULI MACHINE

Machine Metric	Isolated 2 MW Concept	NASA ULI Machine	Units
Current Rating Per Module	794	445.1	A_{pk}
Slot/Pole	48/40	18/12	-
Fundamental Frequency	1,666.7	2,000	Hz
Avg. Torque	3710.1	477.5	N-m
Tip Speed	197.3	200	m/s
Rotor Diameter	753.6	190	mm
Stack Length	86	155	mm
Current Density	21.0	35.6	A_{rms}/mm^2
Shear Stress	48.4	54.3	kPa
Magnet Loading	0.7	0.7	T
Electric Loading	138.2	155	kA/m
Physical Airgap (total with sleeving)	1.0 (3.5)	1.5 (4.7)	mm
Active Power Density	23.5	22.6	kW/kg
Turns per coil	5	7	---------
Slot Fill Factor	0.46	0.26	---------

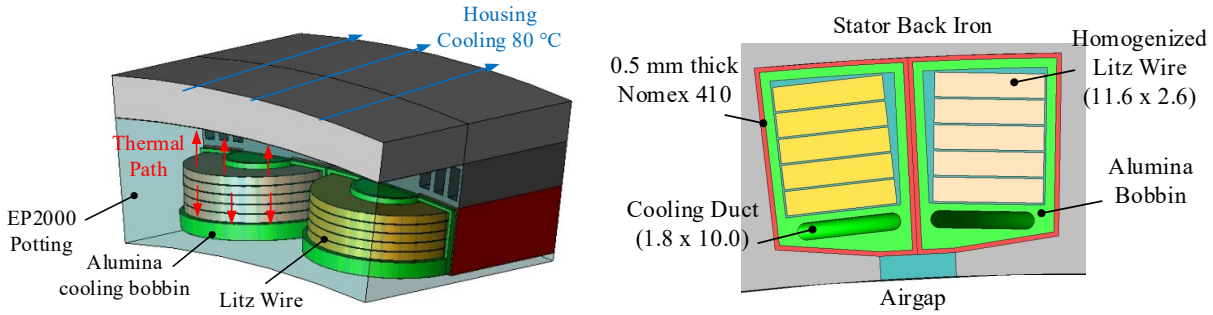

Figure 3-1.—Developed 2 MW stator concept with both back-iron isolation features and in-slot cooling bobbin (left), and slot layout with intra-phase tooth tips shown (right).

3.1.2 Electromagnetic FEA Design Summary

Machine electromagnetic features and machine design approach match what is described in Section 2.0 including the use of cobalt-iron laminations (VAC48), high temperature samarium-cobalt magnets (Recoma 35E) in a Halbach magnet array, and thermally conductive potting material (EP2000). Rotor magnets are assumed to sufficiently segmented resulting in small levels of losses relative to other components (e.g., stator and rotor core losses). Similarly, the carbon fiber retaining sleeve is assumed to have minimal loss. Last, for further simplification AC losses related to high frequency fields are ignored due to the use of rectangular type-8 litz (with dimension 11.6 by 2.6 mm) wire with fine strands.

A transient electromagnetic analysis is completed using JMAG Designer to evaluate the full load characteristics of the machine. Final 2 MW machine dimensions and associated full-load flux density FEA results are provided in Figure 3-2. Machine 3D electromagnetic performance results and machine parameters are summarized in Table 3-3 and Table 3-4, respectively.

3.1.2.1 Evaluation of Tooth Tips Design and Electromagnetic Isolation

Interphase tooth tips are removed in the Figure 3-2 design to assess their associated inductance benefits. Without the tooth tips the module inductance drops to 45.8 μH or a 11.6 percent reduction in machine inductance compared to the inductance value provided Table 3-4. It is clear this inductance contribution

could increase by closing the 8 mm gap between tooth tips in Figure 3-2. This notable change in machine inductance highlights the importance of the leakage inductance associated with these tooth-tips and the potential design hazards of completely removing all tooth tips to reduced current unbalance caused by mutual leakage inductance between adjacent phases. Further, increased self-inductance via this tooth-tip leakage will improve MIR metrics. In this design the inclusion of these tooth tip features is critical for realizing high inductance and low characteristic current.

The previously used Module Isolation Ratio (MIR) can be used to assess the magnetic isolation of the developed 2 MW design. This ratio is determined by calculating the ratio self- and mutual- flux linkages between adjacent machine phases. A MIR metric of 2.1 percent is calculated for the presented 2 MW design indicating good magnetic isolation between modules. This compares to the original quadcopter design in Section 2.0 which has an MIR factor of 2.7 percent. As such, the developed 2 MW design confirms the effectiveness of the developed magnetic isolation approach at high power levels.

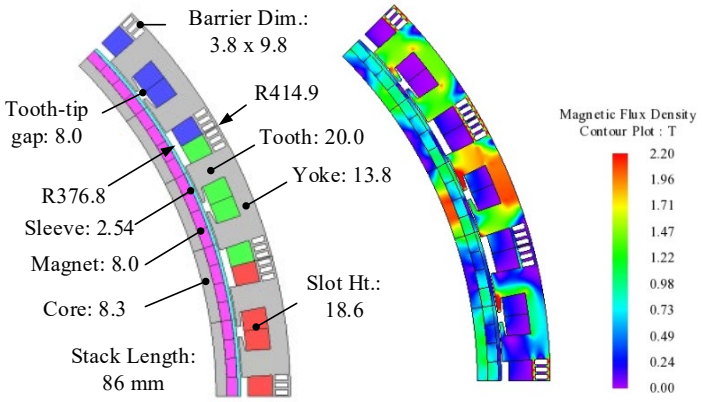

Figure 3-2.—Machine electromagnetic dimensions and full-load flux density contours for single three-phase winding in a four-module 48-slot 40-pole design.

TABLE 3-3.—ELECTROMAGNETIC PERFORMANCE OF A 2 MW ISOLATED PMSM

Specification	Value	Units
Torque	3710	N-m
Speed	5000	rpm
Shaft Power	1942.7	kW
Torque Ripple	5.2	%
Winding Loss	27.7	kW
Core Loss	11.2 (S), 1.2 (R)	kW
Total Active Mass	82.6	kg
Power Density	23.5	kW/kg

TABLE 3-4.—CALCULATED 2 MW RATED MACHINE MODULE PARAMETERS

Machine Module Metric	Quantity
Rated Module Phase Current [A_{pk}]	794
Rated Module Phase Voltage [V_{pk}]	742.5
Module flux linkage with 200 °C Magnets [Wb]	0.0414
Module Phase Inductance [µH]	51.8
Characteristic Current [A_{pk}]	658.2
Module DC Phase Resistance [mΩ]	7.325

3.1.3 Thermal FEA Summary

The steady-state thermal performance of the bobbin cooling system described in Figure 3-1 is evaluated using JMAG Designer's 3D FEA thermal package. This evaluation uses materials and associated properties matching those provided in Reference 4. Homogenized litz wire thermal conductivities are estimated using (Ref. 5). Last, cooling surfaces on the machine outer housing and bobbin cooling channel surfaces (shown in Figure 3-1) are cooled by 80 °C fluid. Contact resistances between components are neglected in this conceptual study.

Loss densities for each of the stator components are provided in Table 3-5, along with full-load loss densities associated with the 70 kW design from Section 2.0. Utilizing the same heat transfer coefficients from Reference 4 (1000 W/m^2-K for coolant channel surfaces and 5000 W/m^2-K for housing channel surfaces) results in a calculated steady state maximum winding temperature of 277.7 °C—well beyond the target maximum of 180 °C. The previously stated thermal assumptions are reconsidered to determine the circumstances where the proposed cooling would work.

First, the EP2000 potting is replaced with an ideal potting material with thermal conductivity of 10 W/m-K (nearly 5x larger), which is also applied to the turn homogenization. This potting assumption is aspirational as it extends beyond typical stand-alone encapsulant material capabilities (Ref. 16). Next, heat transfer coefficients are adjusted until the coil temperature is below the strand insulation limit of 180 °C. These correspond to a convection coefficient of 10,000 W/m^2-K for the housing cooled surface and 2,000 W/m^2-K for the cooling duct channels (a 2x increase from the 70 kW machine). Temperature contours of the 2 MW machine under rated loads with enhanced materials is shown in Figure 3-3 with the top-most turn located in the center of the stack showing a peak temperature of 171.2 °C.

TABLE 3-5.—COMPONENT THERMAL LOSS DENSITIES USED IN 2 MW THERMAL STUDY

Component	2 MW Design	70 kW Design	Ratio
Stator Core Loss Density [W/m^3]	2.10e6	1.52e6	1.38
Winding Loss Density [W/m^3]	1.33e7	1.11e7	1.20

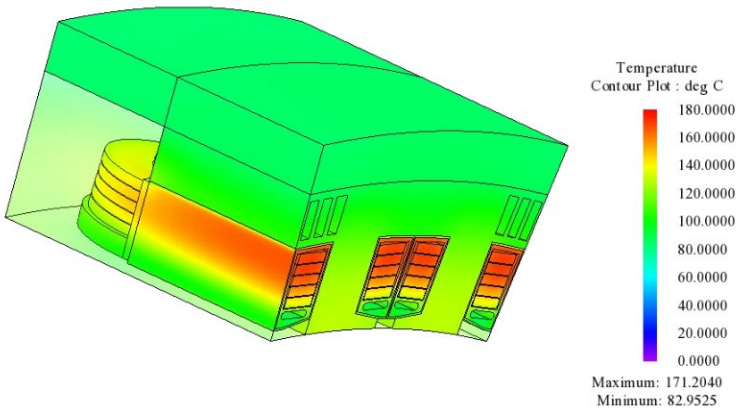

Figure 3-3.—Temperature contours for 2 MW machine under full-load loss contours. Enhanced potting and cooling applied in order to meet 180 °C target.

3.1.3.1 Limitations of Proposed In-Slot Cooling Method

Clearly the need for enhanced potting materials and cooled surfaces for the Figure 3-3 analysis exposes the limitations of the proposed in-slot cooling method. Several observations can be made to understand why this cooling scheme is less capable for megawatt scale cooling compared to the 70 kW design:

1. Higher loss densities in the winding (Table 3-5) increasing cooling requirements.
2. A thicker slot liner insulation is used for the 2 MW design to reflect higher operating voltages (x5 times thicker compared to 70 kW design) effectively eliminating the cooling path through the stator back-iron.
3. Larger overall machine dimensions and associated thermal paths to cooled surfaces. The potted channel cooling distance (from end windings to housing) is 2.1x larger than the 70 kW design. Further, the slot height is also 2.1x larger increasing the thermal path from the topmost turn to the cooling duct in the bottom of the slot. Last, the machine stack length is 2.6x longer, reducing the effectiveness of end-winding oriented cooling like the potted channel approach.

The above reasons summarize the scaling limitations of the proposed cooling bobbin approach, beyond enhanced potting material availability. Certainly, its effectiveness could be better utilized for different megawatt machine geometries with high tip speeds (larger diameters and shorter stack lengths), shallower stator slots, or perhaps modified housing geometries to reduce the potted channel length. In general, more intimate cooling techniques that cool turns individual, like the direct cooling approaches investigated for the NASA ULI machine should be considered (Ref. 17).

3.1.3.2 Megawatt Scale Thermal Isolation Using In-Slot Cooling

The developed model with enhanced potting material is used in a thermal isolation study, where one coil is assigned healthy and the other faulted. The faulted coil loss is increased relative to healthy coil and maximum coil temperatures are recorded. Results of the study are shown in Figure 3-4 highlighting this proposed in-slot cooling with advanced material still achieves good thermal isolation between modules. Overall, only a 10 °C temperature rise is observed for a 2x increase in loss in the faulted coil and corresponding 95 °C rise.

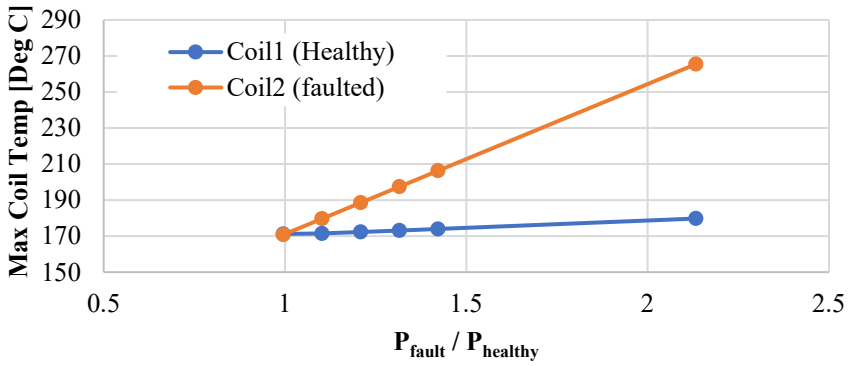

Figure 3-4.—The 2 MW thermal isolation study coil maximum temperatures for varying faulted coil loss quantities.

3.1.4 2 MW Design Conclusions

Presented in this section is a 2 MW rated design with high-power density oriented towards a direct drive propulsion application. This machine possesses the magnetic and thermal isolation features that were previously presented in Section 2.0 for a 70 kW rated design, which are assessed for the 2 MW power level. The electromagnetic design for the 2 MW design is summarized and is shown to have an MIR of 2.1 percent indicating good isolation between modules—confirming the scalability of the proposed magnetic isolation approach. Last, it is identified the use of intra-phase tooth tips can increase the machine phase inductance by > 10 percent.

The losses calculated in the electromagnetic study are applied to a steady state thermal analysis. The proposed cooling method is shown to be ineffective using similar material properties and cooling conditions as the 70 kW reference design. This is attributed to increased loss densities to realize higher power density and general machine geometry increases related to scaling from 70 kW to 2 MW. The use of high thermal conductivity potting materials along with increase convection coefficients can assist with thermal feasibility, though the availability of such materials is questionable. The model using idealized potting is used in a thermal isolation model, confirming the effectiveness of in-slot cooling methods isolating phases from one another.

3.2 Design and Evaluation of Low-Power Modular Motor Drives With Enhanced Isolation Features

The previous section presented a high-power FSCW SPM utilizing isolation features similar to the Section 2.0 quadcopter design. This scaling study is now repeated for machines at lower power levels (<10 kW). This analysis is presented in the context of the development of a low-power FT PMSM demonstrator machine. Instead of a power density focus, this machine design is motivated for fabrication at low cost and speed which is reflected in the design decisions. The fabrication and test of this machine is presented in Section 4.0.

3.2.1 Machine Specifications and Overview

The lower power demonstrator design seeks to incorporate the 70 kW quadcopter machine FT features into a smaller 7 kW rated package with reduced complexity. The objective of this machine is to demonstrate the developed magnetic and thermal isolation features, using readily available materials and existing sample designs through the WEMPEC lab. An IEC100 frame-size design reference is selected as a starting point, which is illustrated in Figure 3-5. Note reference machine dimensions are illustrative of the general scaling and not a representation of the final design.

High level machine specifications are defined based on the selected reference design geometry and available dyne equipment in the WEMPEC lab. Notably the availability of high-speed dynes up to 8,000 is limited so this design assumes the use of a self-dyne test which utilizes the modularity of the machine, circulating power between machine modules. Assuming a self-dyne test, the machine speed rating is set for 8,000 rpm at peak power of 7 kW. Due to the shrinking size of the machine in Figure 3-5, only two three-phase winding sets are considered for geometry reasons, leading to the decision to use a 12-slot 14-pole machine design which is compatible with presented isolation features.

Further, the developed machine is to be designed to operate in both healthy and faulted-module states. Faulted states include three-phase terminal open- and short-circuit faults, and internal short circuits to demonstrate both thermal and magnetic isolation. Overall machine specifications are summarized in Table 3-6.

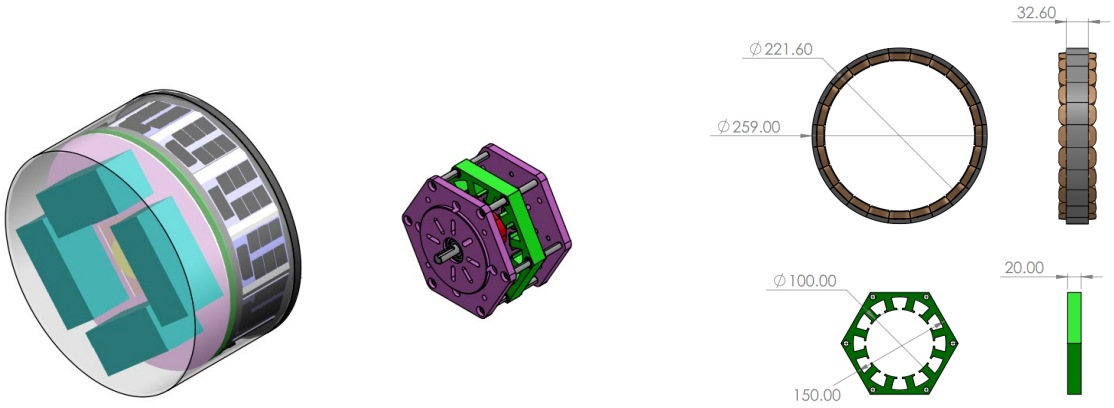

Figure 3-5.—To-scale comparisons of the developed quadrotor machine and identified sample design: (a) housing integration; and (b) stator dimensions in millimeters. Note the final demonstrator dimensions vary from those shared above.

TABLE 3-6.—DEMONSTRATOR METRICS DEFINED BY MACHINE TEST PARAMETERS

Specification [units]	Value	Notes
Slot/Pole	12/14	Similar topology to quadrotor machine design
Torque Rating [N-m]	8.3	Approximately 10% of quadrotor rating
Number of Modules	2	Three-phase modules
Peak Shaft Power Coupled [kW]	2.6	Directly measurable using dyne setup
Peak Speed Coupled [rev/min]	3000	Fundamental = 350 Hz
Peak Power Self-Dyne [kW]	6.9	3.5 kW per module to be measured using voltage and current measurements
Peak Speed Self-Dyne [rev/min]	8000	Fundamental = 933.3 Hz
DC Bus Limit [VDC]	350	Target parameters set in advance for both power electronics and machine.
Rated Current [A]	15.3	

The shared target ratings are modified after taking into consideration 3D effects and manufacturing requirements, later reducing the power rating of the machine to 5.6 kW at 8,000 rpm. This rated power reduction is further discussed in the subsections below.

3.2.1.1 Electromagnetic Material Selection

Electromagnetic components (laminations, magnet wire, and magnets) are selected based on availability and cost point. Both lamination material and magnet wire are available in the WEMPEC lab and are shared in Table 3-7.

The selection of magnetic materials is complicated by the need for both low-cost and availability. As such the use of a Halbach magnet array, custom magnets, or high-performance magnet materials are infeasible. Standard NdFeB rectangular magnet geometries from K&J Magnetics were considered in combination with varying rotor topologies leading to the selection of the K&J B842SH magnet—a high temperature NdFeB magnet (grade N42SH) with dimension 1/2 by 1/4 by 1/8 in. thickness. The lamination stack length is increased to 1 in. (25.4 mm) to accommodate the length of the magnet (the 1/4 in. dimension) requiring four magnets stacked axially per magnet slot.

Last, a Nomex 410 slot liner with 0.070 in. thickness is selected to provide insulation between coil strands and the stator core. Table 3-7 gives a summary of the materials related to the electromagnetic design.

TABLE 3-7.—ELECTROMAGNETIC AND THERMAL MATERIALS USED IN ANALYSIS OF A LOW POWER DEMONSTRATOR

Machine Component	Manufacturer	MFG PN	Relevant Characteristics
Magnet Wire	Essex Brownell	GP/MR-200	• NEMA MW 35-C, polyester amide-imide (200 °C) • 20 AWG (copper diameter 0.813 mm, insulated diameter 0.892 mm)
Lam. Steel Stack	----------	----------	• 29 Ga C5 M19 NGO Steel, 0.356 mm total thickness • C5 film thickness ~6 μm • Assumed stacking factor: 96% • Saturation flux density: ~1.8 T
Magnets	K&J Magnetics	B842SH	• NdFeB (grade N42SH), rated 150 °C, • Dim. 0.5 by 0.25 by 0.125 in. • B_r = 1.31 T, H_c = ~1100 kA/m • Reduce model B_r by 4% to reflect magnet stacking factor
Slot Liner	Nomex	410	• 0.007 in. thickness (0.139 W/m-K thermal conductivity) • 180 °C temperature rating
Alumina Tubing	McMaster Carr	8746K312	• Tube OD and ID: 1/8 in. and 0.063 in., respectively • Dielectric strength 220 V/mil • Thermal conductivity 28.0 W/m-K • Resistivity > 10^{14} Ω-cm
Winding Encapsulant	Epic Resins	S7527	• Thermal conductivity 0.77 W/m-K • Dielectric strength 450 V/mil • Dielectric constant 3.8

3.2.1.2 Dimensional Constraints

Machine stator outer dimensions and hexagonal shape are fixed by the selected WEMPEC reference design, which are shared in Figure 3-7. Holes are placed in the stator back iron to accommodate 8 mm diameter stator support shafts that are used to connect the stator to the machine endbells as illustrated in Figure 3-5. Remaining holes in the stator back-iron represent the selected flux barrier geometry separating phases.

An initial rotor diameter of 100 mm is chosen (see Figure 3-5), though this is later reduced to 87 mm to allow for more reasonable magnet wire sizes and lower winding loss as illustrated in Figure 3-6. The rotor bore dimensions is set to accommodate a 30 mm shaft and key. Other notable dimensional constraints include the inclusion of small holes (x6) in the rotor back iron to be used for the attachment of an axial clamping plate to help axially-support the lamination and magnet stacks. Last, it should be noted this machine has a relatively large airgap of 1.5 mm for its size as shown in Figure 3-6. This was selected to minimize assembly risks associated with this being a student-made machine and the related component tolerance risks.

3.2.1.3 Selection of V-shape IPM Rotor

Alternative rotor topologies including inset SPM, spoke interior permanent magnet (IPM), and v-shape IPM were considered for their ability to best accommodate the planned 14 rotor poles and the limited rectangular magnet sizes available at the desired grade and temperature. The inset-SPM topology is appealing due to commonality with previously shared designs, though is limited by the available magnet grades and dimension, 1.5 mm physical airgap, and further penalized by the supporting magnetic bridges.

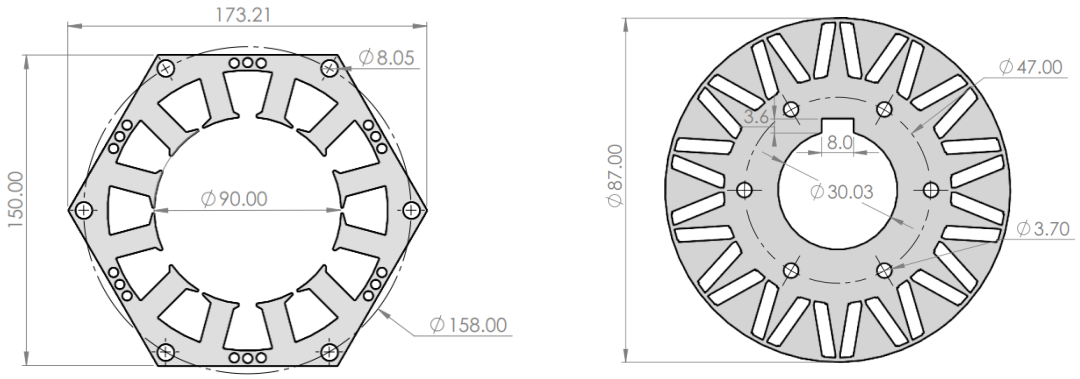

Figure 3-6.—Dimensional constraints in mm for low-power demonstrator: stator (left) and rotor (right).

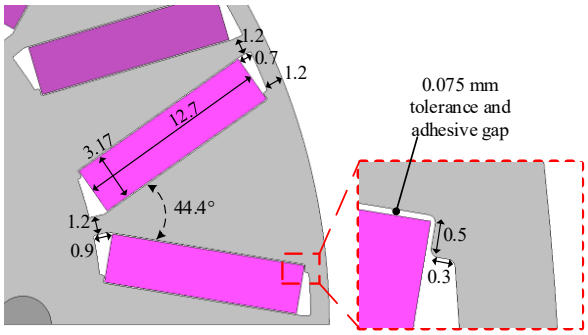

Figure 3-7.—Final IPM magnet dimensions and associated manufacturing features.

The spoke IPM and v-shape IPM are desirable for their flux focusing features allowing for higher airgap flux densities. The flux focusing effect (when the IPM airgap flux B_g exceeds that of an SPM with same thickness h_m and magnet material) is realized by manipulating angle of the v-magnet allowing the magnet width w_m to increase so the total length of the v-shape magnets ($2 \cdot w_m$) is greater than of a half a pole pitch ($\tau_p/2$) leading to the flux focusing requirement:

$$\frac{B_{g,ipm}}{B_{g,spm}} = \frac{4 \cdot w_m}{\tau_p} > 1 \tag{3.1}$$

The above ratio excludes impacts of bridges and posts supporting the magnet and core saturation, which blunts the flux focusing effect. Further, the spoke IPM can be considered an extreme version of v-shape IPM with magnet width w_m only constrained by the rotor radii and pole count of the spoke IPM. Ultimately, the v-shape IPM is selected due to available magnet geometries and simplified bridge design. This leads to an angle of 44.4° between pole-facing magnets leading to a flux focusing ratio of 1.3 and no-load airgap flux density of B_{g1} = 0.78 T (80 °C magnet) and B_{g1} = 0.84 T (20 °C magnet), which is comparable to the previously discussed 70 kW and 2 MW designs using thick high-grade magnets in Halbach magnet arrays.

The selected v-shape geometry in Figure 3-7 is highlighted along with the selected post and bridge thicknesses. These bridge and post thickness are confirmed using structural FEA and indicate significant safety margins on the rotor steel (>10x) at 8,000 rpm. Note a 0.075 mm gap between the magnets and laminations is shown reflecting the lamination and purchased magnets tolerancing, and for spacing for the

magnet adhesive bonding material. Also shown in Figure 3-7 is a small shoulder that is used to locate the position of the rotor magnet. The impact of this gap and shoulder is discussed in a later subsection.

3.2.1.4 In-Slot Cooling Implementation

The previously studied in-slot cooling techniques involved using a 3D printed bobbin made out of highly thermally conductive alumina. Companies like Ceramco offer custom 3D printed alumina and ceramic components. Unfortunately, lead-times associated to these parts is extensive (>10 weeks at the time of this writing) along with significant geometric constraints related to fabrication. As a result, alternative simplified in-slot cooling methods were investigated.

In-slot cooling using alumina rectangular tubes was considered, though the ready availability of custom and standard rectangular tubing is limited. Ultimately, it was decided to use standard alumina tubing available through CoorsTek or McMaster Carr. An alumina tube with a 1/8 in. outer diameter tube with a 0.063 in. inner diameter is selected. A thick wall thickness (0.031 in.) is chosen to improve robustness during assembly and testing. Relevant material properties for the selected alumina tube are provided in Table 3-7.

These alumina tubes are cut to a length of 95 mm and assembled into a six-tube stack. This stack is inserted between all machine coils as shown in Figure 3-8. Slot space is budgeted between coils to account for these tubes in the machine design and analysis. Coolant flows in parallel between the six tubes. In totality, this in-slot method is the only active cooling implemented for this machine. External connections between the stacks and associated tradeoffs are discussed in a later section.

Critical to the in-slot cooling is the choice of winding potting materials. The lead time and cost of previously presented EP2000 (thermal conductivity of 1.9 W/m-K) disqualified it from consideration. To save cost, potting samples were requested from several distributors. As a result, Epic Resins S7527 2-part urethane potting (thermal conductivity of 0.77 W/m-K) is used in this machine analysis and build. Material properties for both the S7527 potting and the alumina tubing are provided in Table 3-7.

Last, a propylene glycol mixture (Koolance 705) is selected for the machine coolant due to is good fluid electrical conductivity (approximately two orders of magnitude lower than typical tap water) which is necessary due to coolant proximity to energized coils. This fluid is also compatible with available pump ERM-3K3UA. Supplier given properties of Koolance 705 are compared against water in Table 3-8.

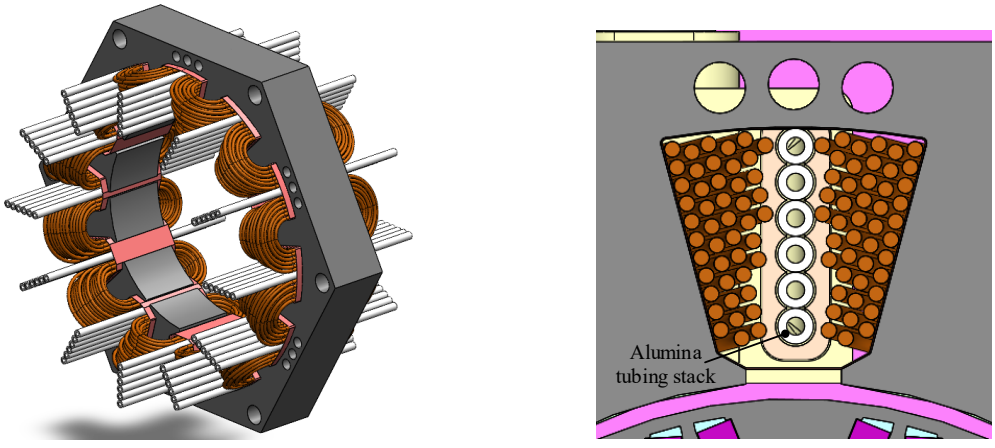

Figure 3-8.—Integration of alumina tubing into stator (left), and slot cross section (right).

TABLE 3-8.—PROPYLENE GLYCOL THERMAL PROPERTIES COMPARED TO WATER AT 20 °C

Property (symbol)	Water	Koolance 705 (propylene glycol)	Units
Dyn. Viscosity (μ)	1.0016	4.300	mPa-s
Kin. Viscosity (ν)	1.0034	3.956	mm^2/s
Density (ρ)	998.2	1087	kg/m^3
Specific Heat (c_p)	4180	3600	J/kg-K
Thermal Cond. (k)	0.58	0.38	W/m-K
Elec. Conductivity	200-800 (tap)	3	μS/cm

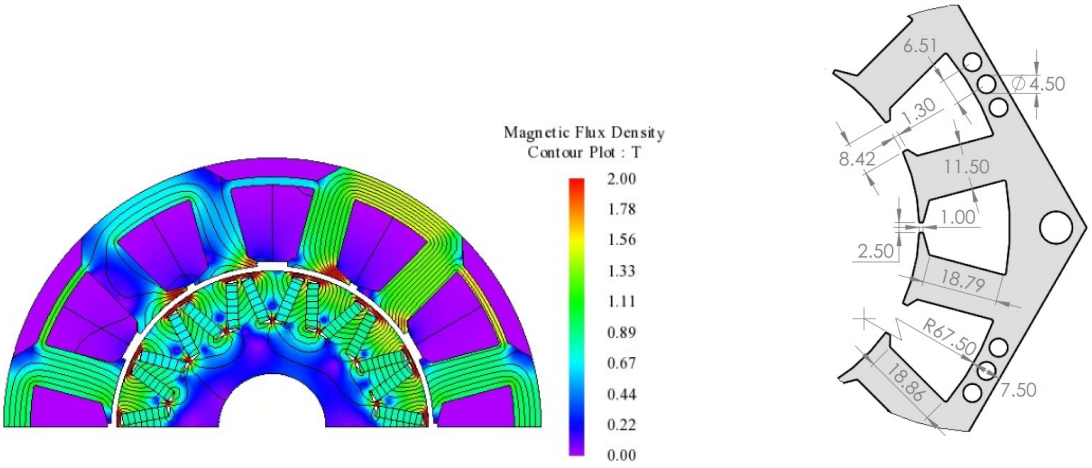

(a) (b)

Figure 3-9.—Final 2D stator optimization: (a) 2D tooth tip optimization result and full load flux density contours with simplified geometry and idealized stator back iron flux barriers; and (b) final machine dimensions with manufacturing and assembly considerations included.

3.2.2 Electromagnetic Analysis

The described geometric constraints above define key stator and rotor dimensions related to machine diameters and magnet placement. Remaining geometric optimization is oriented towards finalizing stator tooth width, tooth tips (both inter- and intra-phase), and back iron thickness for maximum torque and inductance, and minimal torque ripple for a fixed 15.3 A q-axis input current and 350 Vdc bus limit shown in Table 3-6. This optimization utilized an idealized model of the machine (e.g., no gap between magnets and rotor core in Figure 3-7, negligible end-effects, etc.) and idealized flux barriers (majority removal of back-iron material).

This optimization was completed using built-in JMAG optimization tools resulting in the dimensions described in Figure 3-9(a). Notably a stub tooth is added between non-alike coils to keep torque ripple to a minimum. Last, the Figure 3-9(b) drawing reflects updated stator back-iron flux barriers set at a diameter of 4.5 mm (60 percent of the overall back-iron thickness) to maintain the structural integrity of the stator. Ideally more back-iron material would be removed to improve isolation and torque performance.

Initial 2D evaluations show torque performance degrade to 7.6 N-m from the target 8.3 N-m with fixed current and an 80 °C magnet temperature. This analysis also finalized the machine turn count to 47-turns per coil. Further torque performance degradations are observed when additional non-ideal effects are captured in the analysis. These torque reductions are determined acceptable since this machine is a demonstration of the developed isolation features—not of torque performance. In other instances, further

design iterations would be required to recover this lost performance. These non-idealities are summarized below in combination with the expected machine performance.

3.2.2.1 Modified Performance Considering Impact of End Effects and Manufacturing Considerations

Initial idealized machine optimization was performed using 2D FEA for ease of evaluation. However, performance from the idealized 2D optimization degrades once 3D end effects and manufacturing constraints are considered. This subsection summarizes the final machine performance including machine end-effects and updated lamination geometry reflecting the as-built design.

The developed 3D machine model and corresponding full load flux density contours are provided in Figure 3-10. The combined effect of these non-idealities lowers the expected machine output torque to 7.2 N-m (20 °C magnet) or 6.7 N-m (80 °C magnet).

The developed 3D model is used to calculated other machine loss components similar to the procedure described in Reference 4. Machine core loss contours at 8,000 rpm (933 Hz fundamental) and full-current (15.3 A) are shown in Figure 3-11(a). Peak rotor core loss is identified in the rotor post closest to the airgap. In total, a full load core loss of 140.2 and 18.9 W is expected for the stator and rotor, respectively.

A single 1/4 in. magnet segment is modeled to assess magnet joule losses. Full load loss joule loss density contours are shown in Figure 3-11(b). Each magnet segment is estimated to have an average loss of 0.095 W, leading to a total full load magnet loss of 10.6 W (112 magnet segments total).

A similar full-load joule loss study is performed to evaluate eddy current losses in structural components near magnetic components. Considered structural components are highlighted in Figure 3-11(c) and induced current density (corresponding to loss locations) in Figure 3-11(d). Overall, these loss contributions are quite low at 5.7 W, with most of this loss coming from the 1/16 in. thick stainless-steel plate supporting the magnet and lamination stacks.

The largest contributor to machine loss comes from the windings—specifically from the dc resistance. Each coil consists of 47 turns of two-in-hand (two parallel strands) 20 AWG copper strands. Initial machine calculations assumed an end-winding geometry resembling what is described in Figure 3-10 where the end-windings arc around the tooth in a perfect circle leading to a coil resistance calculation of 0.0974 Ω/coil at 20 °C.

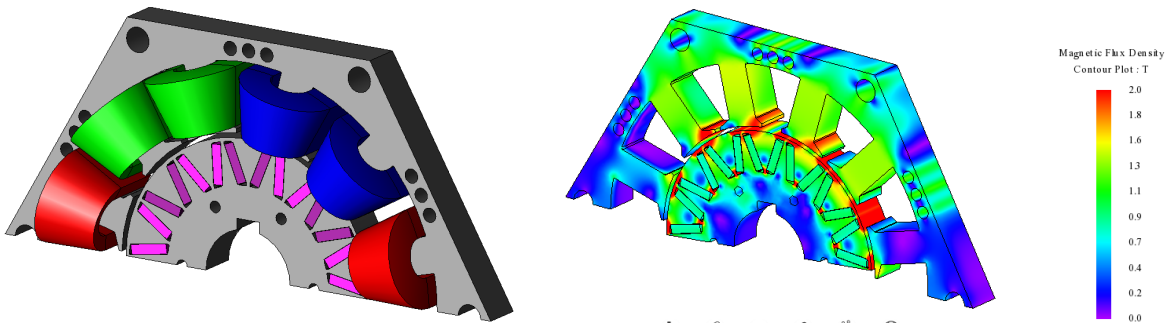

Figure 3-10.—Updated 3D FEA of the demonstrator machine with non-ideal geometry considerations and corresponding full load flux density (20 °C magnet).

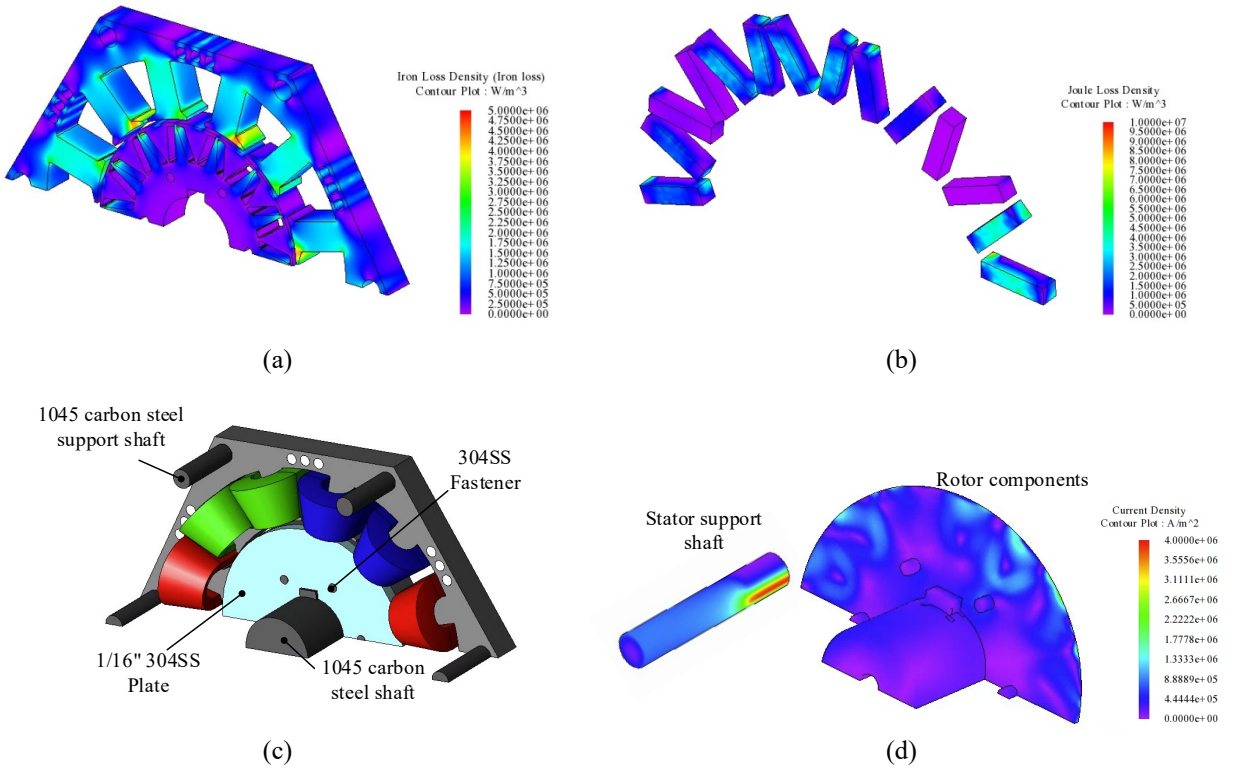

Figure 3-11.—Full-load and speed (933 Hz fundamental) loss studies: (a) core loss; (b) 1/4 in. magnet segment loss; (c) model capturing structural components surrounding the machine; and (d) structural current densities.

In reality, the machine end windings were much flatter against the stator tooth following the contours of the stator geometry. This is reflected in the as-wound resistance of 0.0900 Ω/coil at 20 °C or 0.1251 Ω/coil at 120 °C. The associated dc loss related to the as-wound condition is 126.4 W (20 °C) or 175.7 W (120 °C). The as-wound 150 °C loss metric will be used for the machine efficiency calculation. Last, the developed rated dc current density is 10.4 A_{rms}/mm^2. This corresponds to a copper fill factor of 37.2 percent considering only the wound area and 25.4 percent considering the entire slot area including coolant channel and slot liner space.

Next, ac losses are evaluated for the machine winding considering the high fundamental operating frequency of 933 Hz and for the use of non-transposed magnet wire. To evaluate the impact of high frequency losses, a single machine slot is modeled with each turn set as a conductor with resistivity of 2.34e-8 Ω-m (120 °C).

Four FEA test cases are completed to assess ac losses. Case 1 is a baseline case with full load current in the machine winding at low speed (100 rpm, 11.7 Hz) to confirm expected dc loss performance. Case 2 is a no-load case at full speed at 8,000 rpm (933.3 Hz). Case 3 is a 50 percent load (7.5 A) case at full-speed, and Case 4 is a 100 percent load (15.3 A) at full-speed.

For each case the in-slot losses (both dc and ac combined) are calculated using FEA. The end-winding loss is calculated separately using the dc end winding resistance (0.071 Ω/coil total at 120 °C). These are combined into a total power loss value containing ac losses P_{ac} allowing for the determination of ac loss factors (ACLF):

$$\mathrm{ACLF} = \frac{P_{\mathrm{total}}}{P_{\mathrm{dc}}} \tag{3.2}$$

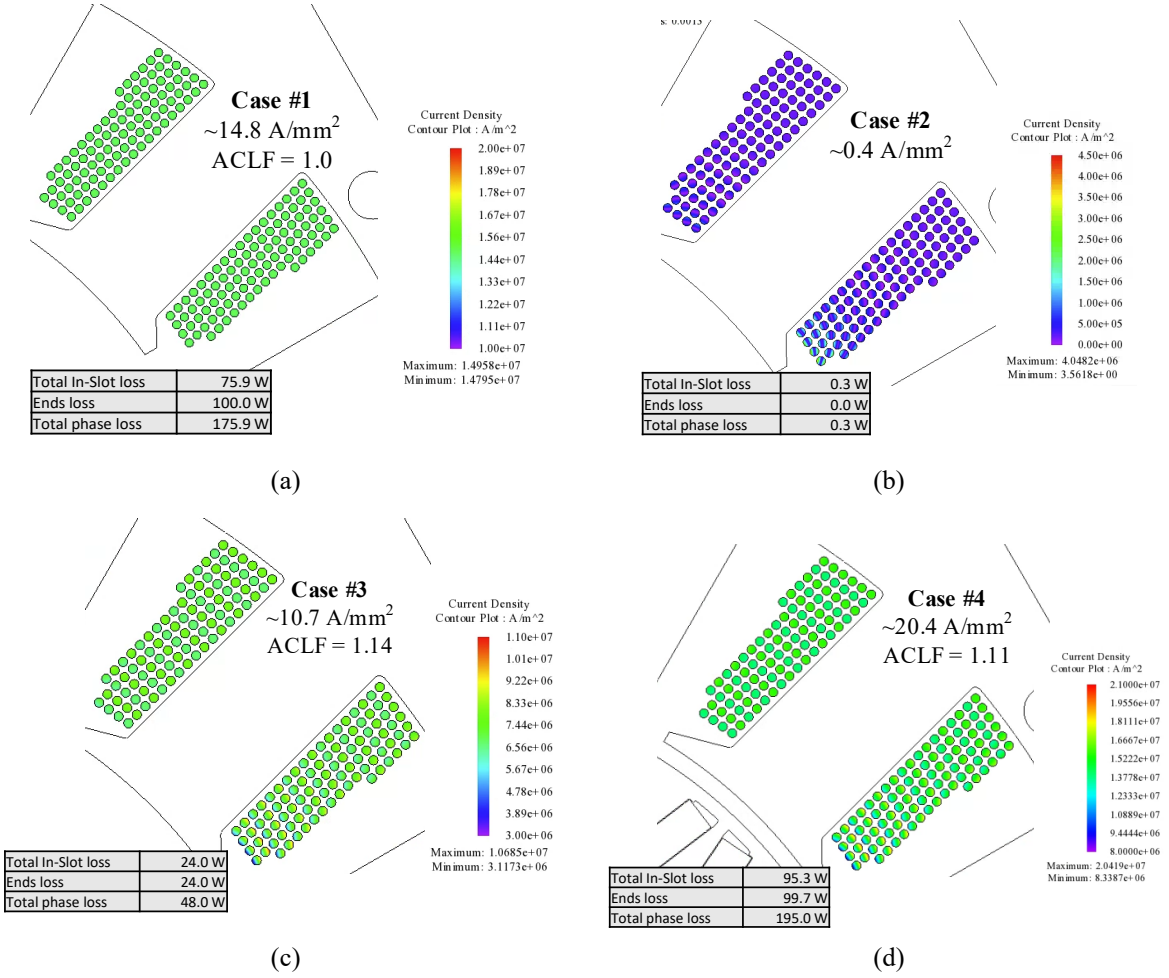

Figure 3-12.—Current density at varying loads and loss: (a) 100 rpm, 15.3 A phase current; (b) 8000 rpm, 0 A phase current; (c) 8000 rpm, 7.5 A phase current; (d) 8000 rpm, 15.3 A phase current.

Current density contours at peak phase current for each of the defined cases are provided in Figure 3-12 along peak current density, loss summary, and ACLFs. As expected, the FEA calculated current density and losses match the expected dc levels previously discussed for case 1. For the high-speed no-load condition (case 2), minimal winding losses related to the radial rotor fields are observed. What minimal current density is observed is limited to the strands nearest the airgap on the side of the slot with the stub tooth.

The effect of proximity losses becomes more apparent with increased current loading as observed in cases 3 and 4. For 50 percent current load the ACLF increases to 1.14. As current increases to 100% rating, the dc losses dominate causing the ACLF to decrease to 1.11 corresponding to a total winding loss of 195.0 W.

Total machine performance is summarized in Table 3-9 including the results above. Total machine efficiency is 93.9 percent at the maximum operating point. Rated power factor is 0.662 at the peak operating point. This poor power factor is a reflection of the degraded output torque discussed above. As mentioned, the purpose of this machine is not to maximize performance but rather demonstrate the developed FT features. Machine efficiency improves up to 95 percent for the lower temperature operating points in Table 3-9.

TABLE 3-9.—SUMMARY OF MACHINE PERFORMANCE AT VARYING OPERATING POINTS

Metric	3,000 rpm (20 °C)	8,000 rpm (20 °C)	3,000 rpm (T_{rated})	8,000 rpm (T_{rated})	Notes
Speed [rev/min]	3000	8000	3000	8000	Coupled (low speed) and uncoupled (high speed)
Avg. Torque [N-m]	7.2		6.7		Rated 80 °C magnets
Power [kW]	2.3	6.0	2.1	5.6	End effects considered
Module Line-Line Voltage [$V_{ll,pk}$]	144.3	370.5	130.1	339.8	Module Terminal Values Number of turns per coil = 47
Module Current [A_{pk}]	15.3				10.4 A_{rms}/mm^2
Winding Loss [W]	126.4		175.7		Rated 120 °C winding temp.
AC Winding Loss [W]	3.3	19.3	3.3	19.3	Assume approximately equal losses at 20 °C
Stator Core Loss [W]	29.5	140.2	29.5	140.2	Higher performance core materials available
Rotor Core Loss [W]	4.0	18.9	4.0	18.9	----------
3D Magnet Loss [W]	0.5	3.3	0.5	3.3	1/4 in. magnet segments
Structure Loss [W]	---	5.7	---	5.7	1/16 in. 304SS plate dominate
Efficiency [%]	93.4%	95.0%	90.8%	93.9%	----------
Power Factor	0.644	0.643	0.671	0.662	----------

Performance numbers related to the full-torque 3,000 rpm operating point are provided since this will be the highest-power coupled operating point. Further, room temperature operating point data (for both magnets and windings) is provided, which is useful for evaluating the Section 4.0 test results. For simplicity, ac losses are assumed equal for both temperatures even though the results would change with lower winding resistivity and stronger fields from the rotor magnets.

3.2.2.2 Machine Module Equivalent Circuit Parameters

Module equivalent circuit parameters related to the presented machine are summarized below for both room temperature windings and magnets, and for rated operating temperatures (120 °C windings, 80 °C magnets). Characteristic current values are determined by applying negative d-axis currents to the 3D model until zero d-axis flux linkage is reached. Note the low characteristic current relative to rated current. This is expected due to the low power factors in Table 3-9.

While low power factor (and therefore characteristic current) is generally undesirable due to the increased kVA requirements for the power electronics, it is beneficial from a FT perspective to have high inductance to limit fault currents. This is especially true for PMSMs which are vulnerable to demagnetization related to fault transients and high characteristic currents. To evaluate demagnetization risks, a negative d-axis current is applied to the model. Following the demagnetization evaluation method outlined in Section 2.0, negligible demagnetization is observed for 3x rated current (45.9 A) on the negative d-axis with an 80 °C magnet.

TABLE 3-10.—CALCULATED DEMONSTRATOR EQUIVALENT CIRCUIT MACHINE PARAMETERS

Machine Module Metric	Quantity (20 °C)	Quantity (T_{rated})
Rated Module Phase Current [A_{pk}]	15.3	15.3
Rated Module Phase Voltage [V_{pk}]	213.9	196.2
Module flux linkage Magnets [Wb]	0.0231	0.0216
Module q-axis Inductance [mH]	1.69	1.72
Module d-axis Inductance [mH]	1.88	1.91
Characteristic Current [A_{pk}]	11.5	10.6
Module DC Phase Resistance [mΩ]	180.0	250.2

3.2.2.3 Evaluation of Magnetic Isolation and Tooth Tip Inductance Contribution

Interphase tooth tips are removed in the Figure 3-10 model to assess the associated inductance benefits. Without the tooth tips, the module d- and q-axis inductances drop respectively by 0.24 mH (12.6 percent) and 0.25 mH (14.5 percent) compared to the rated temperature inductances given Table 3-10. This change in inductance is in similar proportion to the previously presented 2 MW design further highlighting its capability to influence overall machine inductance.

Magnetic isolation of the demonstrator design is assessed using the Module Isolation Ratio (MIR). Once again, this ratio is determined by calculating the ratio of mutual- and self- flux linkages between adjacent machine phases. A MIR metric of 1.7 percent is calculated indicating exceptional isolation between modules—significantly lower than the previous studied machines.

3.2.3 Thermal Evaluation

The loss calculations from the previous section are used in a stator steady-state thermal FEA model to assess the cooling capability of the proposed in-slot method. The developed two-coil stator cooling model, assumptions, and material properties is shown Figure 3-13. For simplicity, contact resistance between components are neglected. Anisotropic stator properties for the stator lamination stack are estimated using (Ref. 18). A thermal conductivity of 23 W/m-K is used for in the lamination plane and 1.63 W/m-K is used for the perpendicular axis. A homogenized coil is shown with winding and perpendicular direction thermal conductivities estimated using (Ref. 5), the copper fill factors, insulation dimensions defined above, and the potting thermal conductivity (0.77 W/m-K). This leads to a coil direction thermal conductivity of 141.8 and 1.50 W/m-K for the perpendicular direction.

A 3D printed 4 mm thick endplate made from Onyx (Markforged) material is included to better represent the final machine assembly. Anisotropic material properties for Onyx are given in Reference 19 which are based on the direction of the print extrusion. For model simplicity, an isotropic material with the lower-bound thermal conductivity of 0.3 W/m-K is assumed. Other material properties are summarized in Table 3-7.

3.2.3.1 Cooled Surfaces Heat Transfer Coefficients

Cooled surfaces in the Figure 3-13 include surfaces of the alumina tubes and ambient air convection on the stator and endplate exposed surfaces. Both 20 °C air and Koolance 705 inlet fluid is assumed (see Table 3-8 for fluid properties). For simplicity, a heat transfer coefficient of 5 W/m^2-K is assumed for surfaces exposed to ambient air. Interior duct flow correlations are used estimate reasonable heat transfer coefficients for tube inner surfaces. The reader is referred to Reference 20 for further discussions about these internal flow calculations.

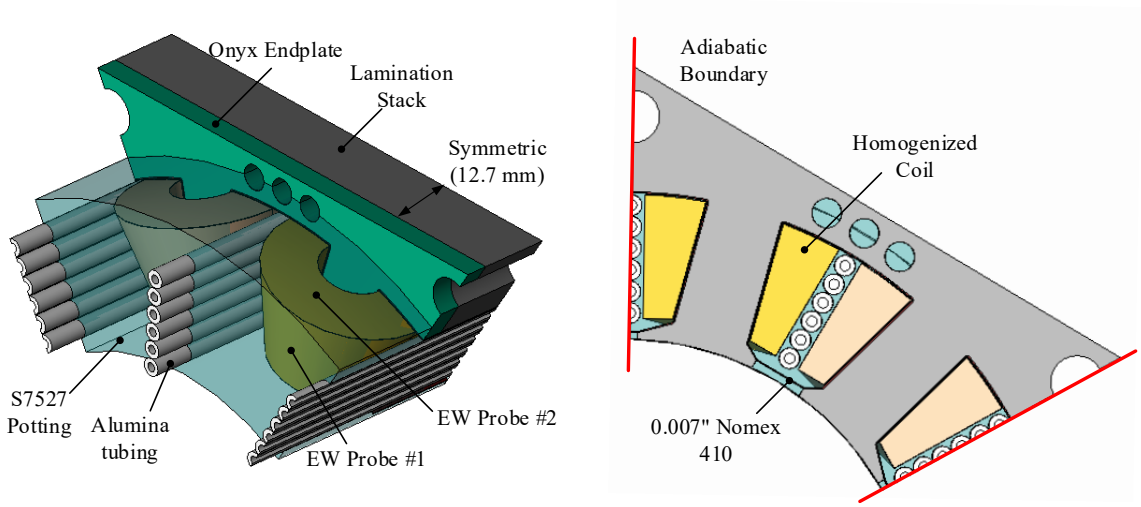

Figure 3-13.—Steady stator model used in the thermal analysis for the developed demonstrator machine.

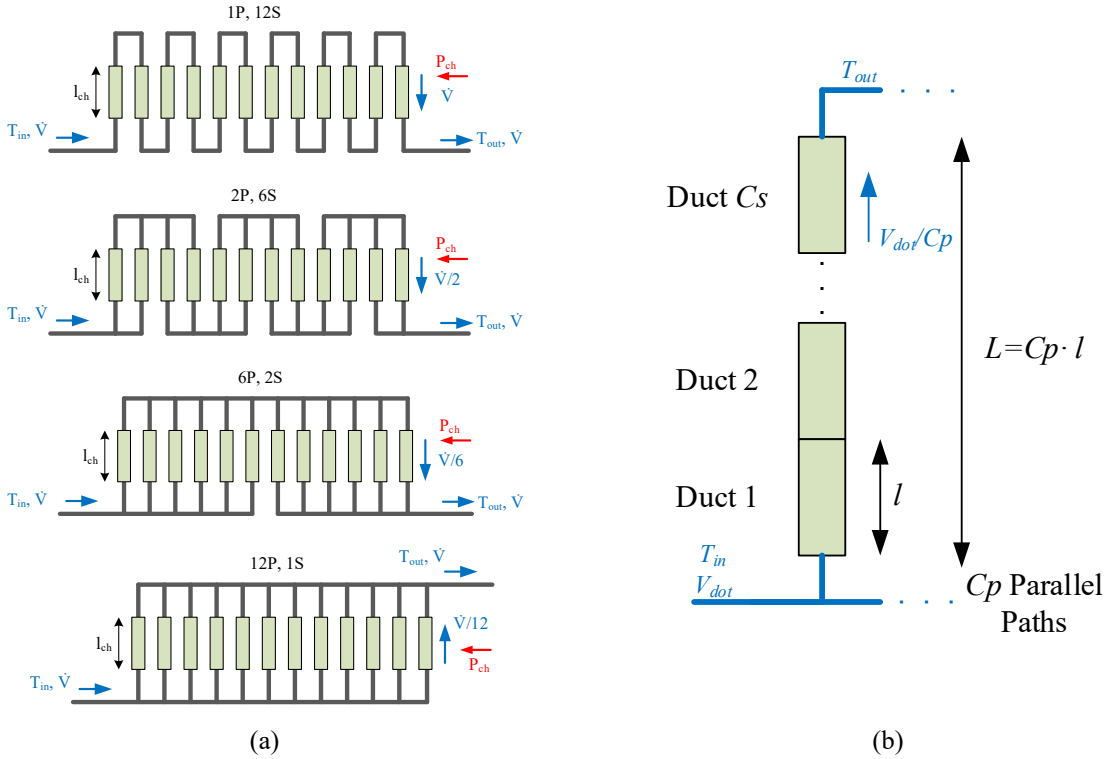

Figure 3-14.—Series and parallel in-slot cooling connection diagrams (a); and straight-line duct model for correlations analysis (b) with variables duct length *l*, number of series and parallel connected ducts *Cs* and *Cp*, respectively.

The evaluation is expanded to consider the hydraulic connections between in-slot cooling channels and the related tradeoffs from a connection complexity and FT-implication standpoint. In total, this stator possesses twelve cooling ducts (corresponding to 12 coils and slots) which can be connected in series, parallel or some combination. Possible coolant connection schemes are shown in Figure 3-14(a) which are compatible with the two-module machine.

The selected connection scheme must take into consideration both machine and thermal system tradeoffs. A series connected system has system power density advantages with less hardware and fittings compared to a parallel system (e.g., manifolding, balancing valves, hoses, etc.). The obvious disadvantage

to a series connected system is high operating pressures and related constricted flow affecting the pump decision. It may be necessary to increase cooling duct dimensions to accommodate higher flows, though this is at the expense of valuable slot area that would otherwise be occupied by copper. Further, the series connected system is penalized due to fluid temperature rise ΔT related to loss Q and mass flow $\dot{m}$

$$\Delta T = \frac{Q}{\dot{m} \cdot c_p} \tag{3.3}$$

Without sufficient flow, downstream components will have higher inlet fluid temperatures from upstream heating, degrading thermal performance of coils nearest the outlet. Mitigation can be realized by increasing the mass flow rate, exacerbating the identified pressure-flow problem. The all-series connected system also has disadvantages from a FT thermal isolation perspective. Heat related to a fault event in an upstream coil will affect inlet fluid temperatures of healthy coils downstream.

As stated, a parallel system allows for lower operating pressures and potentially smaller ducts creating opportunities for greater amounts of slot copper and reduced winding losses. The obvious implication is the increased number of components related to the paralleled systems which will affect cost and number of failure points. Further, a parallel system has greater thermal isolation benefits due to decoupled inlet fluid temperatures. The isolation problem is shifted to the heat exchanger and its ability to reject additional heat related to the winding failure and post-fault overload operation to maintain torque. The heat exchanger and pump must be oversized to manage these increased loads. Last, a parallel system does have redundancy benefits where a channel can clog without failing the entire cooling loop.

Clearly both series and paralleled cooling connections have distinct tradeoffs with likely optimum solution using a combination of parallel and series fluid paths. The selection of the series parallel connection must consider the modularity of the stator to maintain better thermal isolation between modules. Compatible two-module series and parallel flow paths for the 12-slot design are given in Figure 3-14(a).

In an ideal FT system, redundancy could be applied the thermal management system improving thermal isolation between modules at the expense of higher component counts. Ultimately the selection of connection scheme must be made in-combination with pump sizing. In general, a series connected system must have a pump with high-pressure, low-flow characteristics. Conversely a more parallel system must have a pump system with low-pressure, high-flow characteristics. Pressure flow calculations using correlations for each of the Figure 3-14(a) connections are made assuming a single line diagram in Figure 3-14(b). The calculated pressure will be underestimated as it excludes bends between tube connections and pressure-losses related to cooling-loop components. For this demonstrator test, a Koolance ERM-3K3U reservoir-pump is used with maximum speed-setting pump curve given in Figure 3-15 against the calculated pressure flow characteristics of the identified duct configurations.

All of the flow points shown in Figure 3-15 are for laminar flow. Expected flow operating points occur at the intersection of the pump curve in Figure 3-15, further highlighting the tradeoffs between series and parallel connections. A 2-series 6-parallel connection is selected allowing two-series ducts-per-coil, reducing thermal interactions between phases. The expected operating point for this configuration is 7 LPM. For this analysis the expected flow rate is reduced to 3.5 LPM (a 2x safety factor reduction) to reflect the non-idealities not captured in the analysis and the later reduced pump operating speed during the test. As a result, a heat transfer coefficient of 1,800 W/m^2-K is used for tube surfaces based on correlation calculations.

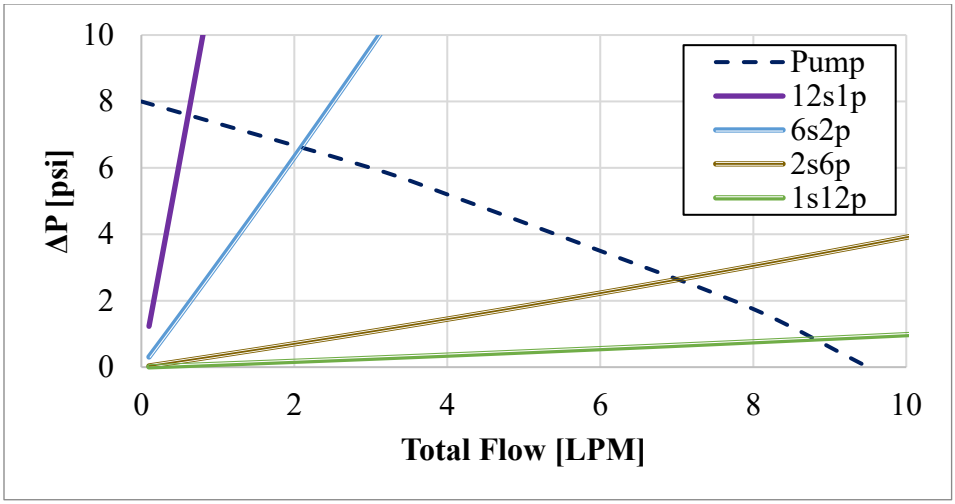

Figure 3-15.—Straight line pressure-flow characteristics of the identified duct connections and selected pump maximum-speed pump curve.

3.2.3.2 Steady State Thermal Analysis

Seven steady thermal operating point are considered to evaluate the developed cooling system. Cases 1 and 2 refer to 50 and 100 percent current-load levels with room-temperature windings at low speed (minimal core loss). These points will be useful for evaluating the machine thermal performance in Section 4.0. Cases 3 and 4 are for the full-current 3,000 rpm operating speed and room-temperature winding losses from Table 3-9. Case 5 captures the 8,000 rpm full-load operating point in Table 3-9 at rated temperature. Case 6 corresponds to an overload test condition discussed in Section 4.0. Last, the limits of the developed cooling system are evaluated in case 7 with current density pushed up to 20 A_{rms}/mm^2 and maximum stator core loss. All losses are assumed evenly distributed in the shown geometry.

These cases are summarized in Table 3-11 along with corresponding steady state FEA results. These include maximum coil temperatures, maximum core temperatures, and end winding surface probe temperatures defined in Figure 3-13. Temperature contours related to cases 5 and 7 are given in Figure 3-16.

Overall, the simulated cooling scheme meets the material thermal limits defined in Table 3-7 (< 155 °C) for all cases. Even under the highest loss-load scenario of 609 W (case 7) the peak calculated winding temperature is 92.1 °C (or a 72.1 °C temperature rise)—nearly a 63 °C margin on material limits highlighting the effectiveness of the developed in-slot cooling method. Certainly, greater increases in current density are feasible due to the extensive thermal margin. Next, the results suggest the winding losses presented in Table 3-9 as overly conservative and can be updated with an iterative loss and thermal analysis.

The FEA temperature contours in Figure 3-16 highlight the maximum winding temperature located the upper corner of the stator slot at the portion of the coil furthest from the cooling ducts. Further, the maximum stator core temperature tracks well with the maximum coil temperature as indicated in the temperature FEA contours and Table 3-11. As observed in the FEA contours and in the Table 3-11 summary, thermal gradients exist in the end winding which may cause variation in the measured temperature.

3.2.3.3 Thermal Isolation Evaluation

Thermal isolation is assessed by assigning healthy and faulted coils to the two-coil thermal FEA model. Losses in the faulted coil are increased relative to the healthy coil, and the corresponding maximum temperature rise is recorded. Steady state thermal FEA results are given in Figure 3-17 summarizing the

isolation study. For a 3x increase in loss, the faulted coil temperature increases 42.2 °C compared to only an 8.7 °C rise in the healthy coil indicating reasonable thermal isolation between phase coils confirm the low-power scalability of the proposed thermal isolation feature.

TABLE 3-11.—STEADY STATE FEA STUDY RESULTS (20 °C FLUID)

Case	Case Description	Total Coil Loss, (W)	Total Core Loss, (W)	Max. Coil Temp., (°C)	Max. Core Temp., (°C)	EW #1 Probe Temp., (°C)	EW #2 Probe Temp., (°C)
1	50% current, low speed	31.2	0	24.1	23.6	22.3	23.9
2	100% current, low speed	126	0	36.2	34.0	29.7	35.3
3	3,000 rpm, 100% current, low temp. coil	129.3	29.5	39.1	37.2	30.8	38.0
4	3,000 rpm, 100% current, high temp. coil	179	29.5	45.4	42.7	34.6	43.9
5	8,000 rpm, 100% current, high temp. coil	195	140.2	58.2	58.0	39.4	55.2
6	Low-speed 37% overload	238.1	0	50.6	46.3	38.2	48.7
7	20 A_{rms} /mm^2 overload and full core loss	468.8	140.2	92.1	85.8	60.1	87.7

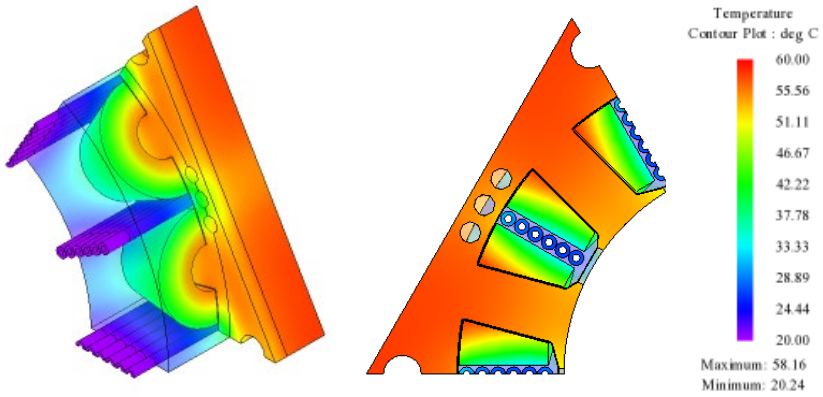

(a)

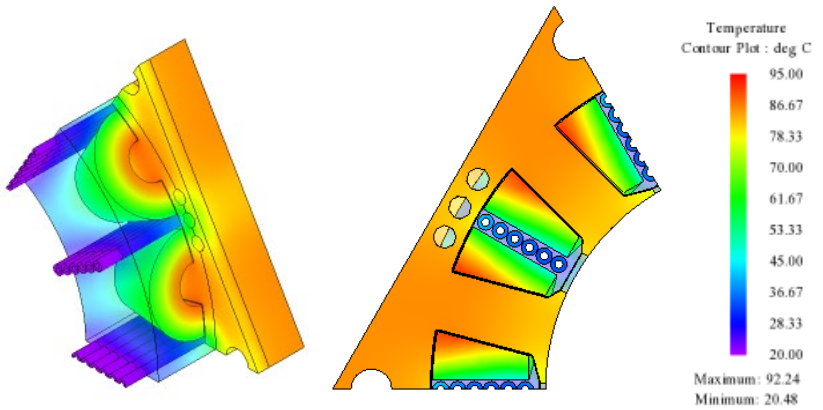

(b)

Figure 3-16.—Steady state FEA flux density contours: (a) case 5 peak loss condition; and (b) case 7 peak overload condition.

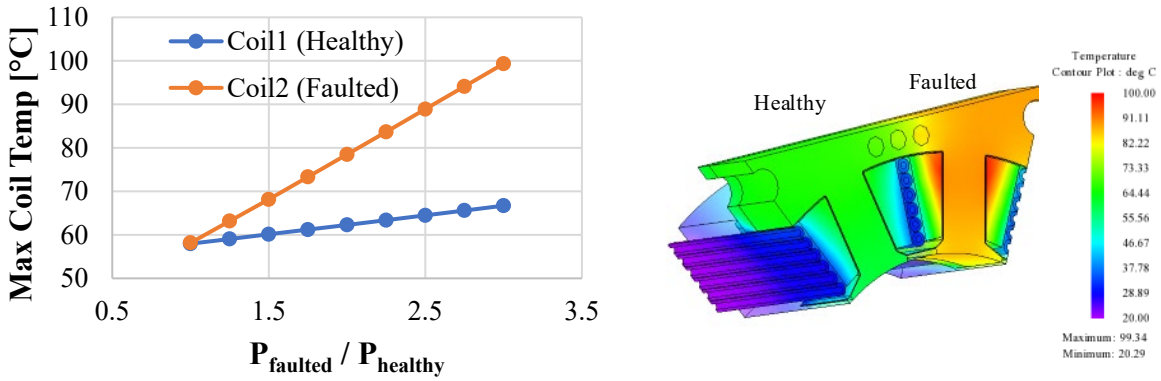

Figure 3-17.—Thermal isolation summary of the demonstrator machine (left) showing healthy and faulted maximum coil temperatures against relative faulted coil loss increase and steady state temperature contour showing healthy and faulted coil temperatures at 3x loss condition.

3.3 Summary

This section has presented the results of an investigation addressing the power scalability of the magnetic isolation features and in-slot cooling configuration developed for FT modular machines. Flux barriers, modified stator tooth tips, and in-slot cooling have been studied for magnetic and thermal isolation scaling capabilities up to 2 MW and down to 7 kW power levels. The objective of this isolation system scaling is to develop representative machines with these features at the power levels of interest, and then calculating relevant isolation performance metrics.

The 2 MW design was guided by electrified propulsion criteria provided by ARPA-E (5000 rpm direct drive, 12 kW/kg total power density for both machines and drives). Other design sizing criteria are inspired by the NASA ULI 1MW machine described in Reference 4 that informed an initial sizing analysis of a 48-slot, 40-pole design that incorporates the developed isolation features. After FEA optimization, the machine exhibits a reasonable active power density of 23.5 kW/kg, on par with the presented NASA ULI design.

A magnetic isolation study of the 2 MW design predicts an MIR isolation rating of 2.7 percent, demonstrating that the proposed magnetic isolation features scales well to higher power levels. The same study shows the inductance boosting capability of the innermost-tooth tip on the overall inductance. Removing these tooth tips from the design result in an 11.6 percent reduction in machine inductance.

The 2 MW machine design has been evaluated for its thermal performance using the same ceramic bobbin and potted channel cooling approach introduced in Section 2.0. The cooling capability of the bobbin approach exhibits limited ability to effectively cool the 2 MW winding, requiring highly thermally conductive potting materials in order to realize reasonable temperatures. This difficulty can be traced to general loss density increases due to the high-power density requirements and the well-known geometric scaling laws expected for megawatt-scale designs. In general, the cooling bobbin technique does not scale well at megawatt power levels without enhanced materials or significant co-optimization between the electromagnetic and thermal designs to improve the heat transfer to the coolant. In addition, effective thermal isolation between shared coils in a slot has been confirmed, even though the steady-state performance of the in-slot cooling technique is poor.

The second half of this chapter introduces a 7 kW demonstrator utilizing the previously described isolation features. Differing from the previous studied machines, this design was developed to be fabricated and tested in order to experimentally confirm the FT isolation features. Performance requirements for the machine have been outlined, reflecting the need for compatibility with readily available materials and ease

of fabrication. As a result of these practical considerations, a 12-slot, 14-pole design with a V-shaped IPM rotor topology was selected that is compatible with two three-phase modules.

The predicted electromagnetic performance of the 7 kW machine has been presented. The analysis shows degradation in the machine torque performance and power factor due to manufacturing considerations (e.g., tolerancing, etc.) and 3D effects that are significant for the short stack-length of this machine. A complete 3D FEA loss analysis has been presented. At rated load and temperatures, the machine is expected to achieve a 93.9 percent efficiency.

The developed electromagnetic models were then assessed for magnetic isolation and a MIR value of 1.7 percent has been calculated, confirming the scalability of the magnetic isolation features to lower power levels. In addition, the contribution of the inner-most tooth tips has been assessed, indicating a 12.6 percent contribution to the total inductance—a similar value to that calculated for the scaled 2 MW machine.

The calculated losses were applied to a steady-state thermal model using FEA. Differing from the other designs, this machine utilizes in-slot cooling via alumina tubes positioned along the radial centerline of the slot. For rated conditions, this machine exhibits exceptional cooling with a calculated 38 °C maximum temperature rise. The thermal limits of this machine have been assessed, and simulations indicate 20 A_{rms}/mm^2 continuous current density is feasible with maximum coil temperatures below 100 °C. The developed model was then used for a thermal isolation study. The proposed cooling channels exhibit very good thermal isolation between machine phases, confirming the scalability of the thermal isolation technique to lower-power machines.

4.0 Fabrication and Experimental Evaluation of Fault-Tolerant Low-Power Demonstrator Machine

The low-power demonstrator machine discussed in Section 3.2 has been fabricated and tested to evaluate the developed model and proposed isolation approach. This chapter presents a comprehensive summary of machine fabrication and testing work for this machine including both healthy and faulted module operation. In general, both healthy and faulted test data aligns extremely well with the simulated results presented in Section 3.0. Faulted module tests include terminal open- and short-circuit testing. Additionally, turn-to-turn faults are built into one of the machine phases, enabling the external application of turn-to-turn short-circuits faults. In addition, the electromagnetic isolation achieved with this machine has been evaluated statically by exciting the modules at high frequency with a stationary rotor, confirming the low mutual coupling between the two modules.

4.1 Demonstrator Machine Description and Test Objectives

The demonstrator machine that was designed and built is a double layer (DL) 12-slot 14-pole fractional slot concentrated wound (FSCW) stator with a v-shape interior permanent magnet (IPM) rotor topology. The stator is modularized into two three-phase winding sets allowing for the loss of a module without loss of torque operation. Machine phases are isolated from one another using a combination of stator flux barriers and modified stator tooth tips. The winding is directly cooled by flowing a low-electrical-conductivity coolant through tubes placed between coils. Doing so provides physical separation between coils and isolates coils from thermal interactions between phases—both desirable features for FT machines. Machine outer dimensions and feature summary are given in Figure 4-1. The overall core stack length of the machine is 25.4 mm. Greater details related to machine magnetic and thermal performance can be found in Section 3.0.

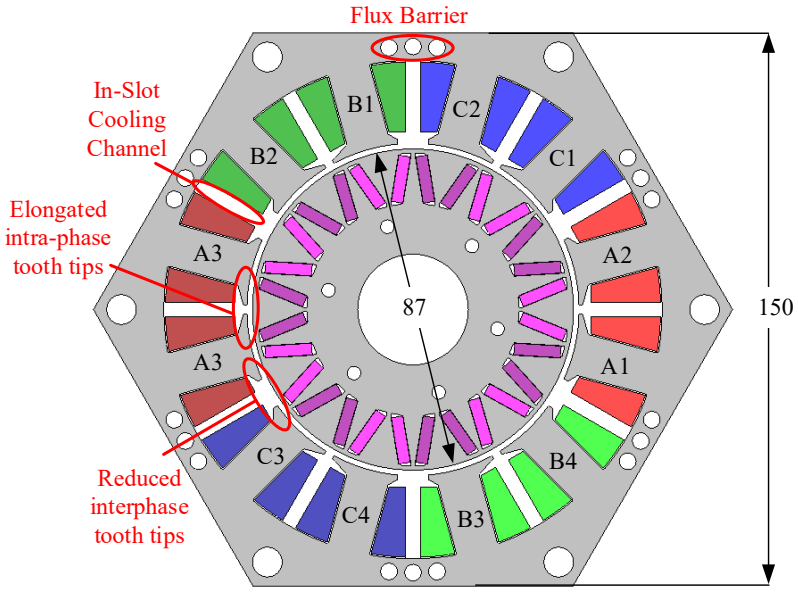

Figure 4-1.—Demonstrator isolation features, phase arrangement, and stator and rotor outer diameter dimensions in mm.

TABLE 4-1.—CALCULATED MACHINE RATINGS AND EQUIVALENT CIRCUIT PARAMETERS AT LOW TEMPERATURE

Machine Module Metric	Quantity
Speed [rpm]	3,000
Torque [N-m]	7.2
Shaft Power [kW]	2.3
Rated Module Phase Current [A_{pk}]	15.3
Rated Module Phase Voltage [V_{pk}]	213.9
Module flux linkage Magnets at 25 °C [Wb]	0.0232
Module q-axis Inductance [mH]	1.69
Module d-axis Inductance [mH]	1.88
Characteristic Current [A_{pk}]	11.5
Module DC Phase Resistance at 25 °C [mΩ]	180.0

Machine ratings and calculated circuit parameters are summarized in Table 4-1. Only room temperature resistances and magnet flux linkages are provided due to observed low operating temperatures during the test. Further, shared performance characteristics are limited to 3000 rpm reflecting the maximum operating speed in this test. The machine was originally designed for operation at 8000 rpm where its rated power would be 6.1 kW, but a compatible dyne was not available for the test. As a result, the entries in Table 4-1 are based on the maximum achievable speed of 3000 rpm, resulting in a lower rated power of 2.3 kW. A self-dyne technique was attempted to test the machine at 8000 rpm in order to reach the higher original target (>6 kW), but could not be successfully completed because of unbalanced magnet pull (UMP) associated with the self-dyne operation that caused significant vibration.

The demonstrator machine has been fully tested up to 3,000 rpm (speed limit of the test dyne) under both healthy and faulted conditions. The implemented machine test sequence is given in Table 4-2. Low-risk tests were performed first in order to insure the collection of valuable data from the test machine before the more aggressive testing associated with the turn-to-turn faults and overload conditions was performed. The test results are presented in an order that provides a natural flow of the material rather than the actual test order found in Table 4-2.

TABLE 4-2.—TEST SEQUENCE AND ASSOCIATED MODULE CONFIGURATION

Test Sequence #	Test (measurement)	Configuration
1	Static Testing (inductance, resistance)	1
2	No-load (back emf)	1
3	Light load testing (torque)	1
4	Full-load testing (torque, temperature)	1
5	Initial OC and SC terminal testing (fault performance, drag torque estimation)	1
6	Full-Load Testing (reconfigured)	2
7	OC and SC terminal fault testing (reconfigured)	2
8	Turn-to-turn fault testing (current amplitude)	2
9	Static Isolation Testing (mutual coupling)	2
10	OC and SC terminal fault response testing (transient response and post-fault operation)	2
11	Aggressive turn-to-turn fault testing and SC fault response (thermal response, transient response, fault amplitudes)	2
12	Overload test and thermal heat run (torque, temperature)	2

Also given in Table 4-2 is a configuration number related to the module coil arrangements during the associated test (M_1 representing module-1 and M_2 representing to module-2). Configuration-1 refers to coil combinations: M_1[A1, A2, C1, C2, B1, B2] and M_2[A3, A4, C3, C4, B3, B4] (see Figure 4-1 for coil placement). Configuration-2 refers to coil combinations: M_1[A1, A2, C3, C4, B1, B2] and M_2[A3, A4, C1, C2, B3, B4]. In other words, configuration 1 represents a split or halved stator arrangement, and configuration 2 represents an interleaved phase arrangement.

Before discussing test results, details related to the machine fabrication and test setup are provided.

4.2 Machine Fabrication

Details related to the fabrication of the demonstrator machine are summarized in this section. Machine fabrication details are presented based on assembly step and subassembly.

4.2.1 Stator Assembly

Components consisting of the stator assembly include bonded lamination stacks, slot liner material, 3D printed onyx endplate material, 20 AWG magnet wire, and end winding thermocouples. Rotor lamination stack bonding is discussed here due to the concurrence of stator and rotor core fabrication.

Stator and rotor laminations are laser cut from 0.356 mm thick M19 steel. A total of 72 laminations are stacked and bonded per core using 3M Scotchcast 265. Based on the machine final stack length, a machine stacking factor of 0.97 is estimated. Figure 4-2(a) shows stator and rotor cores after bonding. 3D printed onyx endplates (4 mm thick) are attached axially to the machine to avoid winding on sharp stator core edges. A 0.007 in. Nomex 410 is formed and taped in place inside the stator slot as shown in Figure 4-2(b).

Each stator tooth is wound with 47 turns of 20 AWG wire (x2 in parallel). A 37.2 percent fill factor is calculated for the winding window (25.4 percent fill factor for entire slot area). Wedges are placed between coils to prevent coil relaxation into the coolant channel space. A 0.015 in. thick NKN555 laminate strip is placed between the coil and tooth tips to hold coils in place and to further insulate coils from exposed tooth tip iron. Final machine winding is shown in Figure 4-2(c). Last, type-K thermocouples from TC Direct (201-301) are taped to machine end windings as shown in Figure 4-2(d).

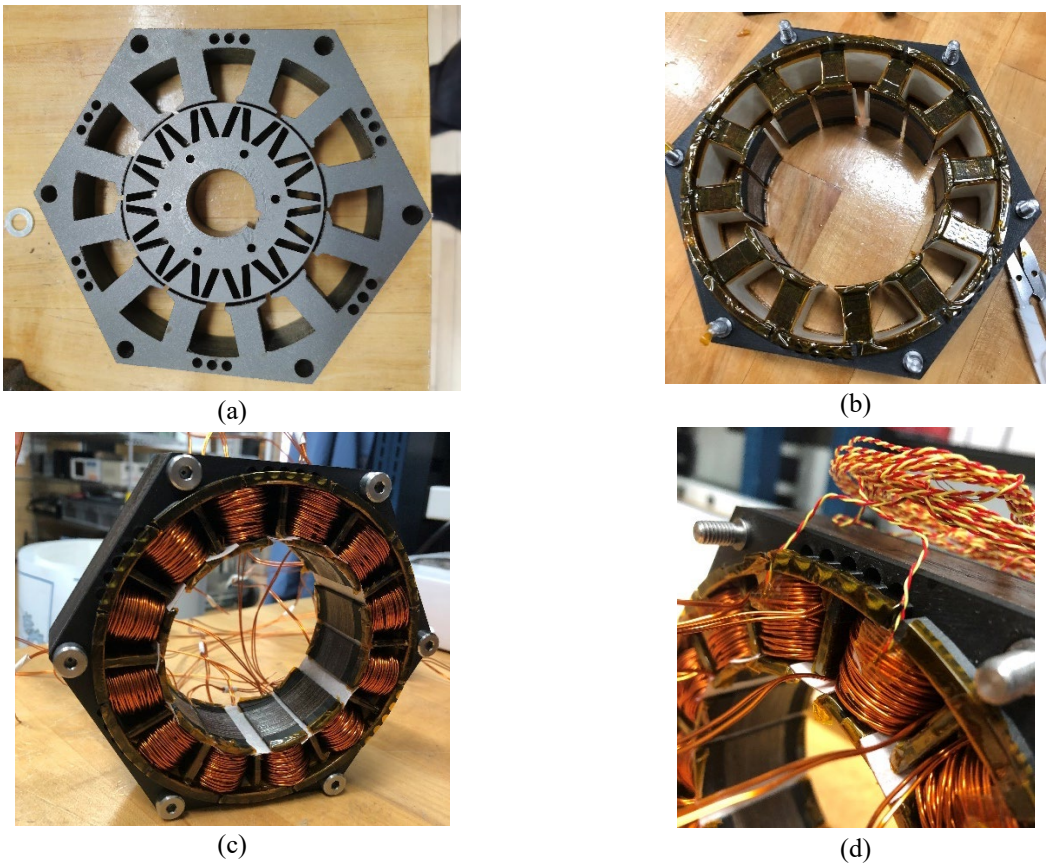

Figure 4-2.—Stator fabrication steps: (a) lamination bonding; (b) endplate and slot liner installation; (c) completed wound stator with spacer wedges; and (d) thermocouple installation.

4.2.2 Cooling Assembly

Stock alumina tubing with inner and outer diameters of 0.063 in. and 0.125 in. is purchased and cut to 95 mm length. The wound stator in Figure 4-2 is inserted into a specially designed potting fixture, spacing wedges are removed from the coils, and the cut alumina tubes are inserted and held in place by the potting fixture as shown in Figure 4-3(a). Epic Resins S7527 potting material is mixed and poured into the potting fixture, placed under vacuum to remove air bubbles, and cured at room temperature. Final potting result is shown in Figure 4-3(b).

Two 3D printed PLA endpieces are used to connect and seal tube endings. The first endpiece (EP1) is placed around tube endings as shown in Figure 4-3(b) and (c). Gaps between the tubes and EP1 are filled with gap filling Loctite 416, with the sealed result shown in Figure 4-3(c). The second endpiece (EP2) seals against the outer rectangular surface of EP1 using the same Loctite 416. This EP2 has a tapped 1/8 in. NPT hole and a quick disconnect fitting (with universal threads and a gasket seal) is attached. EP2 is designed to direct fluid radially outward toward the mentioned quick disconnect fitting in Figure 4-3(d). Each cooling channel is plugged and pressurized with air up to 10 psi to identify leaks which are later sealed. The combined stator and cooling assembly is shown in Figure 4-3(d) before general machine assembly.

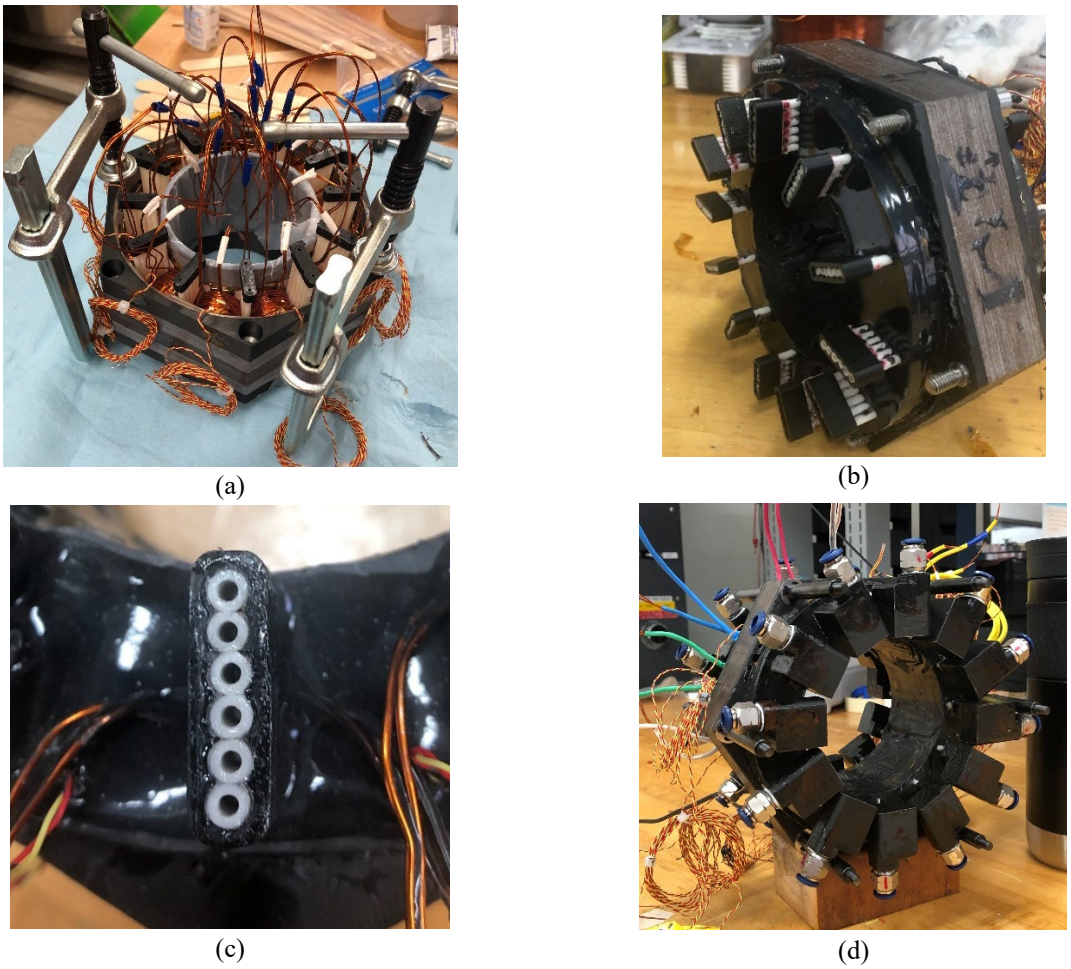

Figure 4-3.—Cooling assembly fabrication steps: (a) alumina tubing insertion into the stator and potting assembly fixturing; (b) post cure potting result; (c) endpiece 1 (EP1) attached to end of alumina tubes; and (d) final stator assembly with cooling endpiece 2 (EP2) and quick disconnects installed.

4.2.3 Rotor Assembly

The bonded rotor core lamination stack is described and shown above in Figure 4-1(a). Next, NdFeB rotor magnets (B842SH) from K&J Magnetics are bonded inside the rotor core magnet slots using Loctite 332 structural adhesive. Each magnet has a length of 6.35 mm so four magnets per slot are required for the 25.4 mm stack length, leading to a total of 112 magnets inserted in all slots. The rotor core assembly with all magnets installed is shown in Figure 4-4(a).

After, the rotor shaft (custom Misumi stepped shaft) and key is pressed into the rotor core as shown in Figure 4-4(b). A 1/16th stainless steel 316 plate is designed with magnet cutouts to axially support the lamination stack and is installed (Figure 4-4(c)). This is a modified version of the plate design presented in Section 3.0 since magnet and rotor core surfaces are not axially flush (i.e., some magnets extend outside the rotor core). This endplate is fastened to the rotor core using 316 stainless steel fasteners and locknuts. Retaining rings on the shaft hold the core-plate assembly in place.

Last, bearing spacers and bearing (B6201ZZ) were installed onto the shaft. A fiberglass reinforced Onyx cover is placed over the rotor endplate to cover the rotor endplate and exposed magnets as shown in Figure 4-4(d). The total rotor assembly (without bearings) is balanced at 3,000 rpm.

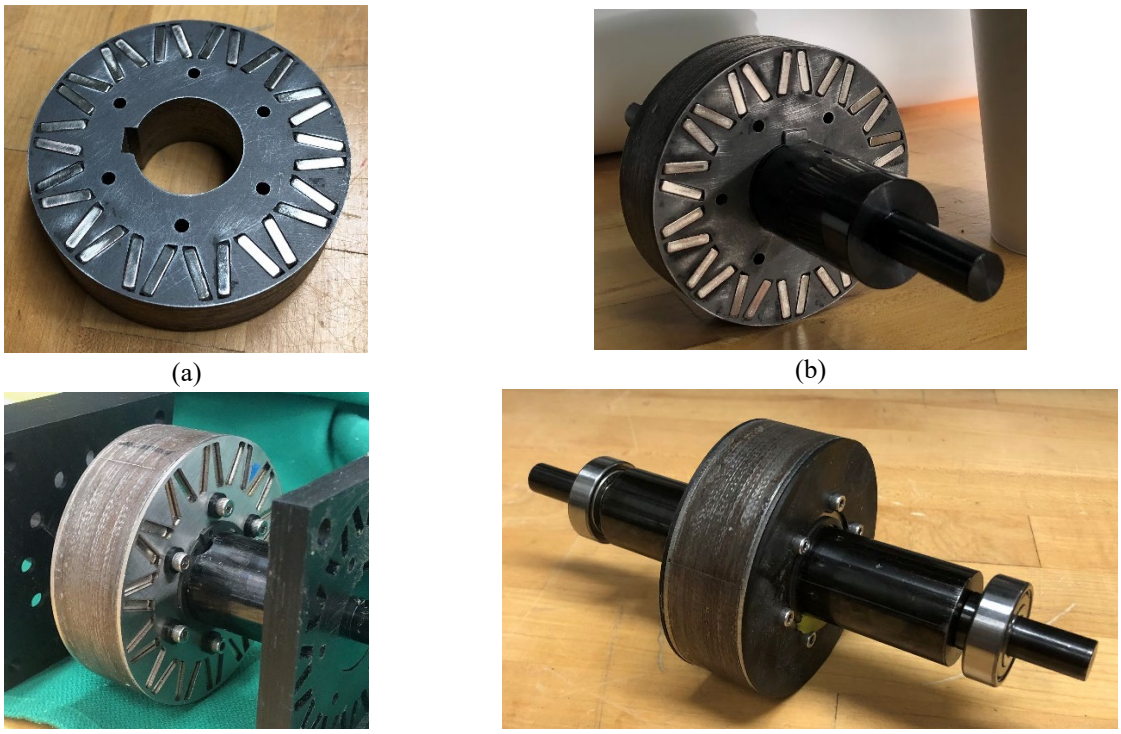

Figure 4-4.—Rotor fabrication: (a) post magnet installation; (b) after key and shaft installation; (c) modified axial support endplate for rotor laminations; and (d) final rotor assembly before general assembly.

4.2.4 General Assembly

Overall general assembly steps are provided without providing precise detail (e.g., fastener and retaining ring installation steps). This general assembly consists of insertion of stator supporting shafts into the stator core (shown in Figure 4-3(d)), non-drive end (NDE) endbell installation onto the stator supporting shafts, rotor assembly insertion into the stator assembly bore, drive end (DE) endbell installation, and the encoder installation onto the NDE shaft extension and endbell. Both endbells are made from Al6061 and the selected encoder is a US Digital E3-1800-472-IE-H-D-3. Photos of the final machine assembly are given in Figure 4-5.

Overall, the built machine has an axial length of 169.5 mm from outer surfaces of both endbells. Between endbell inner surfaces the axial length is 138 mm. The core stack length is 25.4 mm and overall axial length with end windings is a ~46 mm (a bit more if potting material is included). This leads to only 33 percent of the available endbell space being utilized by active components. The remaining 66 percent is predominantly used for coolant channel accommodations. Certainly, this can be reduced with greater design effort, though this at least highlights one of the major challenges associated with the proposed in-slot cooling method.

4.2.5 Faulted Turn Implementation

A critical step not highlighted in the winding section is the inclusion of jumper wires into one of the machine phases (coil A4 in Figure 4-1) allowing for the external application of turn-to-turn faults. Specifically strands from turns 27, 36, and 44 (of 47) are wound outside the coil. These turns were selected due to their ease of removal during the winding process, though allow for a range of faulted turn

combinations. Sufficient length is extended so the looped turns extend above the potting step shared in Figure 4-6(a). The exposed strands are stripped and soldered to 20 AWG magnet wire strands as Figure 4-6(a). After, the solder joints and exposed strands are separated using NKN555 slot liner and potted using leftover S7527 potting material in Figure 4-6(b).

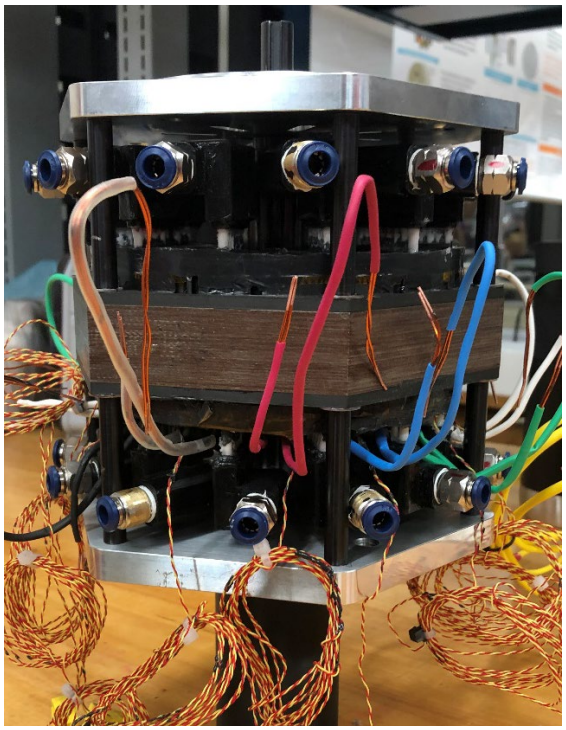

(a)

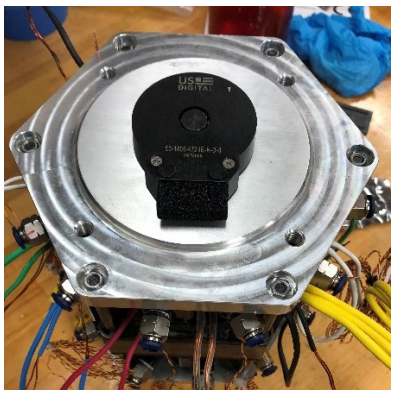

(b)

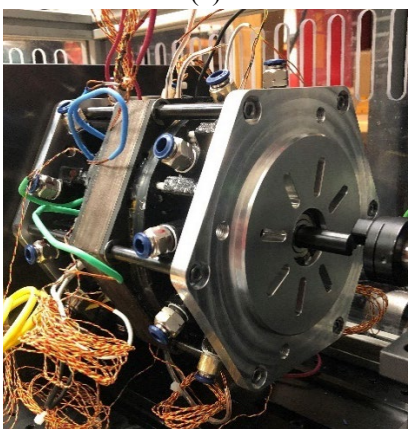

(c)

Figure 4-5.—Views of assembled machine: (a) side view that includes machine power leads, thermocouple wires, and coolant inlet/outlet fittings (b) non-drive-end view showing rotor encoder and (c) drive-end view before installation of stator winding coolant hoses.

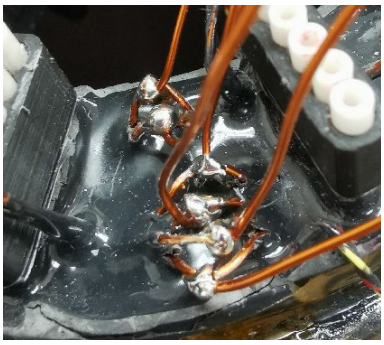

(a)

(b)

Figure 4-6.—Faulted turns 27, 36, and 47 (6 strands total) in phase A3: (a) exposed turns after solder step and (b) re-insulation of solder joints and strands.

4.3 Test Setup

Components and systems related to the test space are shown in Figure 4-7. Not shown is a 600 Vdc 40A Magna power supply and resistive load bank for the dynamometer (necessary for dyne generator operation).

4.3.1 Test Dynamometer

The dyne drive lineup is shown in Figure 4-8. Going from right-to-left in Figure 4-8, the dynamometer consists of an Allen Bradley MPL-A540K load machine and a Ultra3000 motor drive. Using this setup, the dyne is capable of 4.1 kW at 3,000 rpm. The torque transducer is an HBM T21WN/20NM with voltage output with scaling of 0.5 V/N-m.

Neutral and phase connections are made to stripped magnet wire leads using clamp terminal blocks. While convenient, this style of terminal blocks did have notable contact resistance and heating during the test. For some connections one of the two-parallel strands would disconnect, forcing rating current into a single strand (~30 A/mm^2 current density). Module leads, and faulted turns are brought out the back of the dyne towards the power electronics cabinet.

Cooling duct connection and tubing is brought out on a separate side of the machine dyne to the coolant manifolds. Cooling loop connections are discussed in a lower section.

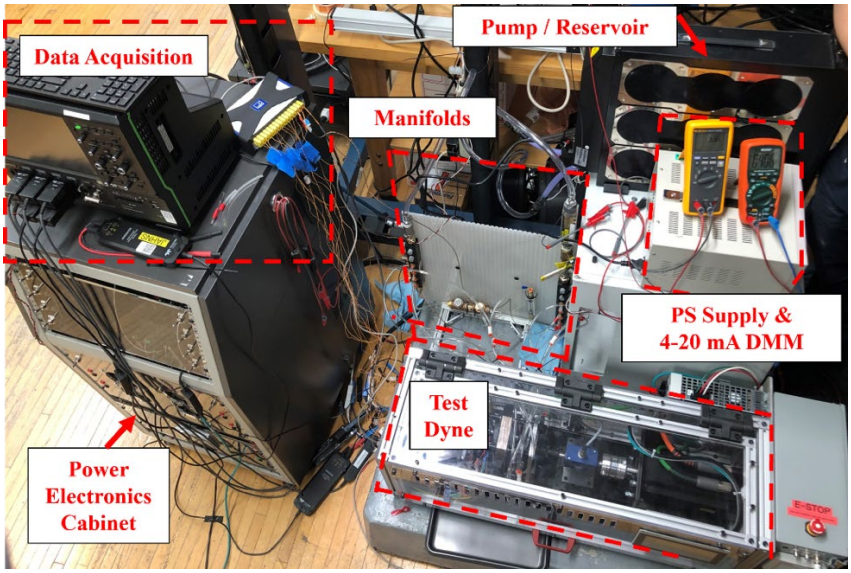

Figure 4-7.—Experimental test space layout and components.

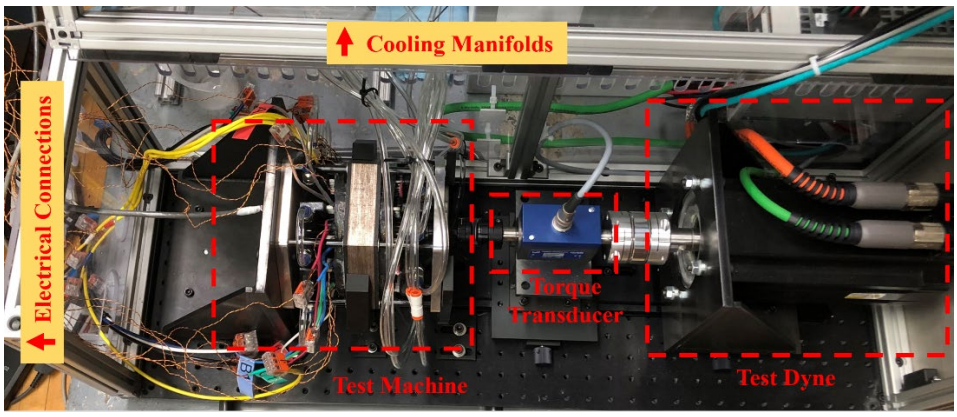

Figure 4-8.—Test dynamometer setup.

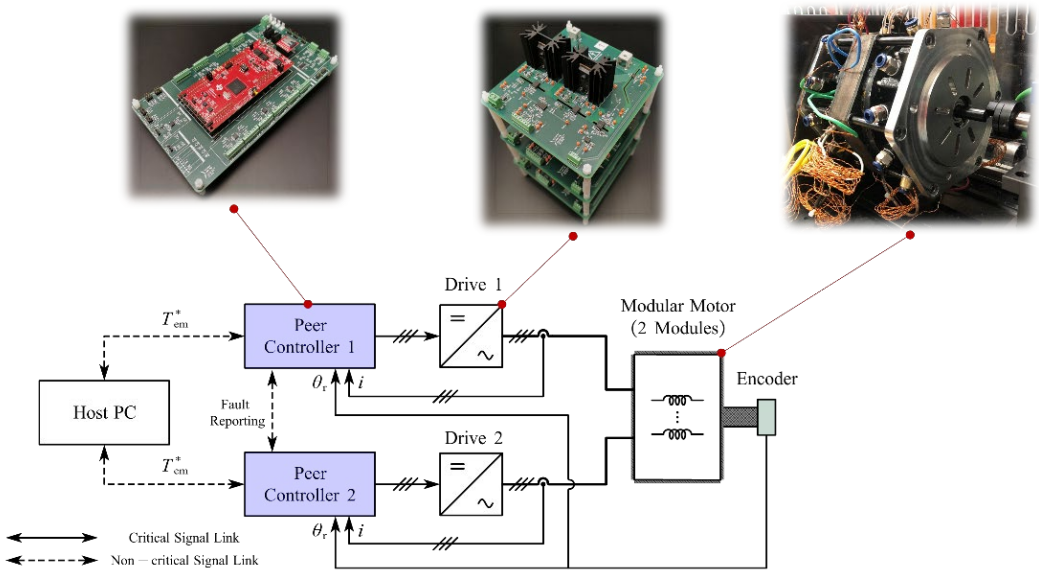

Figure 4-9.—Control, power electronics, and machine architecture (image credit: Hao Zeng, 2023).

4.3.2 Modular Power Electronics and Machine Control

The power electronics cabinet in Figure 4-7 contains modular power electronics to drive the two-different windings sets of the demonstrator machine. A detailed review of the power electronics design and the overall control is beyond the scope of this report. However, interested reader are referred to UW-Madison student Hao Zeng's PhD thesis titled "Distributed Control and Self-Sensing of Permanent-Magnet Modular Motor Drives (MMDs) for Electric Aircraft Propulsion" which discusses this power electronics design among other control related topics surrounding FT modular motor drives. An abbreviated description of the power electronics is provided in this report.

The overall architecture of the power electronics and control is summarized in Figure 4-9. Each machine-module has its own dedicated custom power-electronics consisting of SiC switching devices in stacked half-bridge configuration. Each machine and power electronics module has its own dedicated controller, receiving independent commands from the host computer. These controllers only communicate in the event of a fault and the appropriate remedial action is followed.

4.3.3 Data Acquisition

Primary data collection is made using a Teledyne Lecroy MDA810A oscilloscope that receive voltage measurement signals from HVD3102 voltage and CP031 current probes measuring machine phase voltages and currents. Additional torque transducer voltage output signals are measured using the scope. In some instances, torque measurements are recorded manually from the dyne interface (reading the same torque transducer feedback).

Temperature data from the twelve end winding thermocouples and three cooling loop thermocouples is collected using HBM QuantumX MX1609KB with data observed through the MX Assistance software. This software does not allow for exported temperature measurement data, so only screenshots of various test points are available. For thermal heat run tests, a FLIR thermal image camera is used to assess the stator core and potting temperature.

Additional test measurements are recorded manually in a test notebook during the test. These include dc supply display voltages and currents, multimeter measured 4-20 mA signals from the cooling pressure sensors shown in Figure 4-7, and flow measurements from rotameters in the cooling loop.

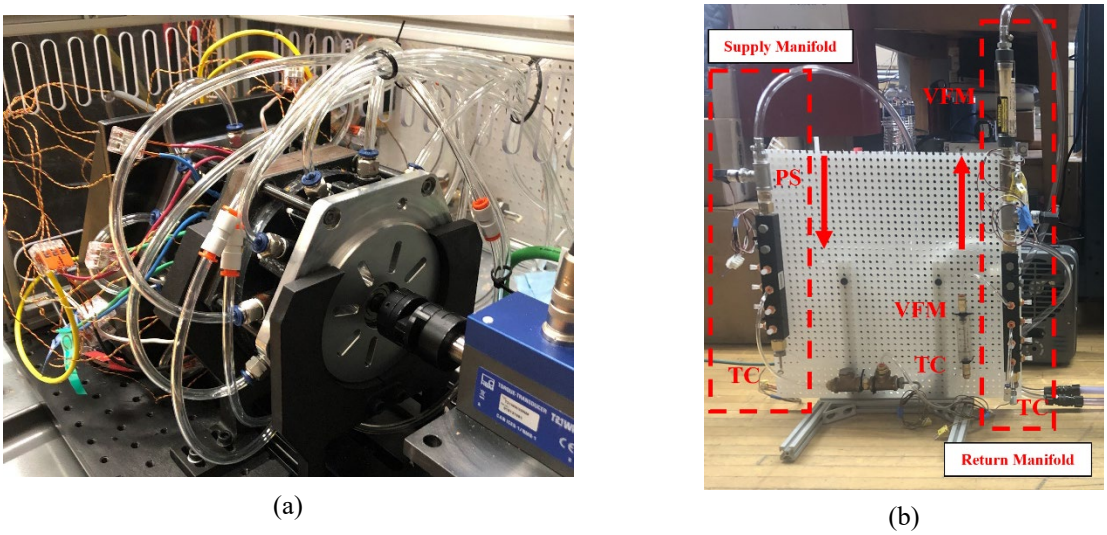

(a) (b)

Figure 4-10.—Cooling loop: (a) machine cooling connections, and (b) manifold components (PS – pressure sensor, VFM – volumetric flow meter, and TC – thermocouple).

4.3.4 Cooling Loop

Machine fluid connections are made at the quick disconnect fittings on either side of the machine using 5/32 in. ID tubing. A 6-parallel 2-series fluid connection scheme is used (discussed in Section 3.0) resulting in all inlet and outlet connections on the DE side of the machine, and tube jumpers on the NDE side as shown in Figure 4-10(a). Inlet and outlet hoses are routed to supply and return manifolds away from the dyne setup as shown in Figure 4-7. It should be noted some variation in hose length is determined acceptable due to the difficulty of connecting hoses under the machine while mounted.

The manifold layout and components are given in Figure 4-10(b). Each manifold has 12 connection ports allowing a 12-parallel test configuration if required, though remaining 6 ports per manifold are plugged for the presented experiment. Each manifold is equipped with a thermocouple to measure bulk flow temperatures and a pressure senor. The return is equipped with a inline volumetric flow meter. The overall system is driven by a Koolance ERM-3K3U pump-reservoir with Koolance 705 (propylene glycol) fluid.

After filling the machine will fluid, the measurements are made for various pump speed settings (1-10 with 10 being maximum speed). Measurements were stopped at a pump speed of 6 due to excessive bubbling coming from the pump supply at higher speeds. Table 4-3 and Table 4-4 provides recorded pressure/flow measurements for pump setting 6. These pressure-flow characteristics are consistent throughout all of the presented experiments.

Several observations can be made from Table 4-3. First, the estimated bulk flow of this system is less than the 3.5 LPM assumed in Section 3's thermal analysis (approximately 22.9 percent lower). Next, there is a notable difference between the estimated branch flow (from the bulk calculation) and the flow measured from a single branch. Some difference may be attributable to the wide error bands of the sensors (±5 percent) and human error in reading the rotameter, though the level of measurement difference indicates some level of unbalanced flow in the system. Another likely source is the asymmetry associated with the branch that has the flowmeter. In any case, these measurements suggest the observed thermal performance will be worse than simulated due to lower flows, and some unbalanced heating will likely be observed related to the uneven branch flows.

TABLE 4-3.—TEST VOLUMETRIC FLOW MEASUREMENTS

Pump Setting	Bulk Volumetric Flow			Branch Volumetric Flow		
	Measured GPM	S.G. Corrected LPM	Est. Branch Flow [LPM]	Measured GPH	S.G Corrected LPM	ΔBranch Flow [LPM]
6	0.8	2.90	0.483	12	0.756	0.273

TABLE 4-4.—TEST MANIFOLD PRESSURE MEASUREMENTS

Pump Setting	Pressure Measurement				
	Supply (mA)	Supply (psi)	Return (mA)	Return (psi)	Pressure Difference (psi)
6	8.02	3.8	5.64	1.5375	2.2

TABLE 4-5.—MEASURED COIL RESISTANCES IN OHMS AFTER WINDING

Coil	Resistance (low)	Resistance (high)	Resistance (average)	Resistance deviation
1	0.090057	0.090207	0.090132	0.1%
2	0.089053	0.090103	0.089578	–0.5%
3	0.090135	0.090205	0.090170	0.2%
4	0.088930	0.089530	0.089230	–0.9%
5	0.090206	0.090317	0.090262	0.3%
6	0.090473	0.090571	0.090522	0.6%
7	0.089243	0.089381	0.089312	–0.8%
8	0.089980	0.090068	0.090024	0.0%
9	0.088864	0.088889	0.088877	–1.3%
10	0.090910	0.091350	0.091130	1.3%
11	0.090827	0.090965	0.090896	1.0%
12	0.089549	0.090225	0.089887	–0.1%
--------	--------	**Overall Average**	**0.090002**	--------

4.4 Machine Parameters Validation

Machine parameters are estimated using a series of static and rotating measurements to validate the machine parameters provided in Table 4-1. These parameters include machine phase resistances, inductances, magnet flux linkage, characteristic current, and module isolation ratio MIR.

4.4.1 Phase Resistance Measurement

Machine coil resistances are measured using a six-digit digital multimeter after the fabrication of the machine. These coil resistances are summarized in Table 4-5.

The phase resistance given in Table 4-5 reflect the measured coil resistances in Table 4-1. All measured machine resistances are well balanced within 3 percent of the overall average. Initial analytical calculations overestimated the coil resistance by approximately 7.5 percent due to differences in end winding geometry. The as-built machine has much smaller end windings compared to what was modeled in Section 3.0.

TABLE 4-6.—MEASURED FAULTED TURN RESISTANCES IN OHMS

Measurement Location	Average Resistance (Ω)
Turn 1—Turn 27	0.057151
Turn 1—Turn 36	0.074178
Turn 1—Turn 44	0.089770

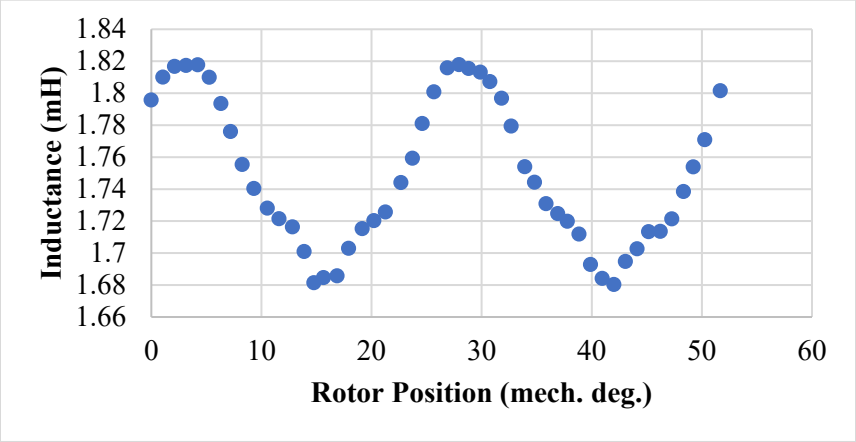

Figure 4-11.—Measured phase inductance for rotor position.

4.4.1.1 Faulted Turns Resistances

Additional resistances related to the faulted turns in Figure 4-6 are measured using the same six-digit digital multimeter. These measured turn resistances relative to the phase lead (turn 1) are given in in Table 4-6.

4.4.2 Inductance Measurement

Machine inductances are measured using RLC meter 4263B (500 mV 1 kHz) at various rotor positions while the machine is coupled to the dyne. The rotor position is moved manually and locked in place for each inductance measurements. Rotor position is recorded using the dyne encoder. Inductance measurements for A1-neutral connection are given in Figure 4-11 for approximately $1/6^{th}$ of a mechanical rotation.

The shown inductances are sinusoidal in shape with peak values corresponding to the d-axis inductance (1.817 mH) and minimum values corresponding to q-axis inductance (1.685). In general, both inductance measurements agree very well with the calculated 1.88 and 1.69 mH d- and q-axis inductances, respectively.

4.4.3 Magnet Flux Linkage Measurement

Magnet flux linkage can be determined from no-load phase voltage measurements capturing the back-emf of the machine. The magnet flux linkage is calculated from the fundamental component of the back-emf E_{i1} and electrical frequency:

$$\lambda_{pm1} = E_{i1} / \omega_e \tag{4.1}$$

No-load back-emf voltage measurements are made for machine speeds up to 3,000 rpm. Figure 4-12 shows the three-phase back-emf voltages (from phase to neutral) from module 1 at 3,000 rpm. At 3,000 rpm the plateau of the back-emf voltage is approximately 48 V. The frequency components of the measured back-emf voltage at 3,000 rpm are calculated with results provided in Figure 4-13. These are contrasted against JMAG design back-emf FFT results also given in Figure 4-13.

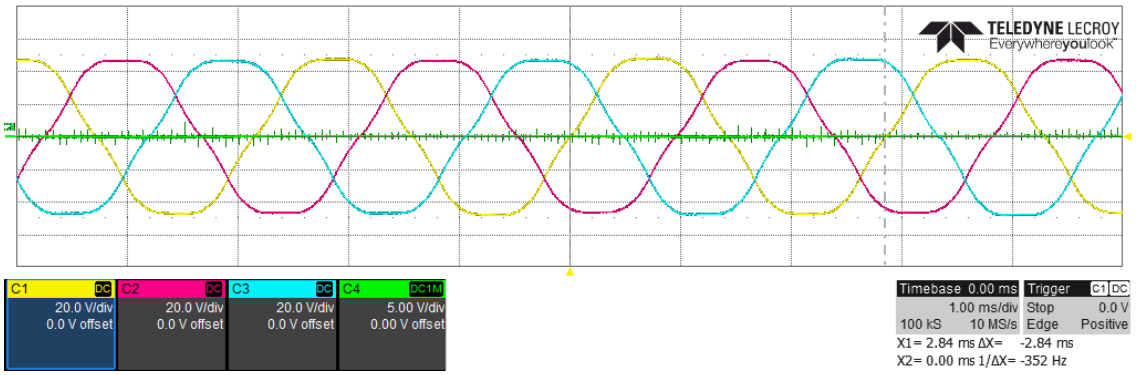

Figure 4-12.—Module 1 back-emf line-neutral voltages at 3,000 rpm.

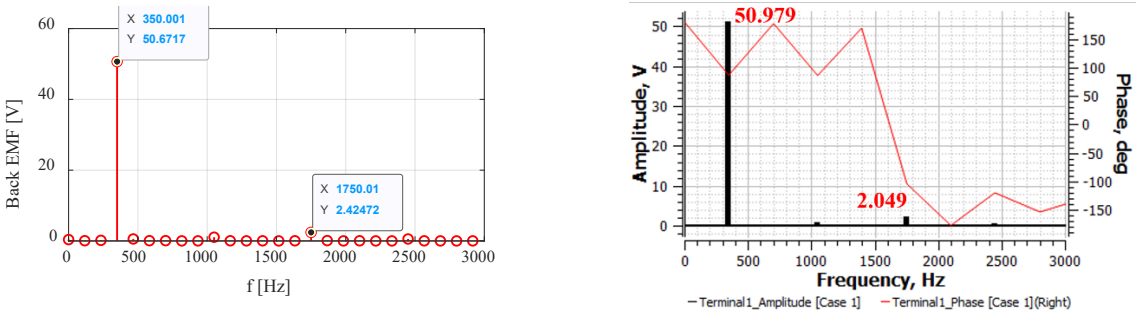

Figure 4-13.—Back-emf measurement FFTs (left) and JMAG designer calculated FFT (right) at 3,000 rpm.

Using the fundamental component of the voltage measurement in Figure 4-13, a magnet flux linkage of 0.0230 Wb is calculated which is within 1 percent of the JMAG calculated 0.0232 Wb. A notable difference between the two calculations is the amplitude of the fifth harmonic which is about 0.4 V higher than simulation.

4.4.4 Characteristic Current Measurement

The machine characteristics current is calculated by applying three-phase shorts to both modules and ramping machine speed. Module-1 phase currents at 3,000 rpm under the three phase currents is shown in Figure 4-14(a) showing peak currents of 11.4 A. This compares to the 11.5 A calculation from JMAG. Measured peak short-circuit current different operating speeds is given in Figure 4-14(b) showing a current amplitude plateau of 11.4 Apk.

The terminal short-circuit test allows for the evaluation of machine braking torque T_{brk}. This is calculated analytically using machine parameters (Ref. 21):

$$T_{\text{brk}} = -\frac{3P}{4} r_s \lambda_{\text{pm}}^2 \omega_e \frac{r_s^2 + \omega_e^2 L_q^2}{\left(R^2 + \omega_e^2 L_q L_d\right)^2} \tag{4.2}$$

Measured braking torque is compared to an analytical calculation using Equation (4.2) and the machine parameters defined in Table 4-1 and shown in Figure 4-15. In general, both curves have the same general shape with peak torques occurring near 140 rev/min. However, a small difference in peak drag torque is observed. The measured result is approximately 0.3 N-m lower than the analytical and can be attributed to non-linearities in the machine parameters.

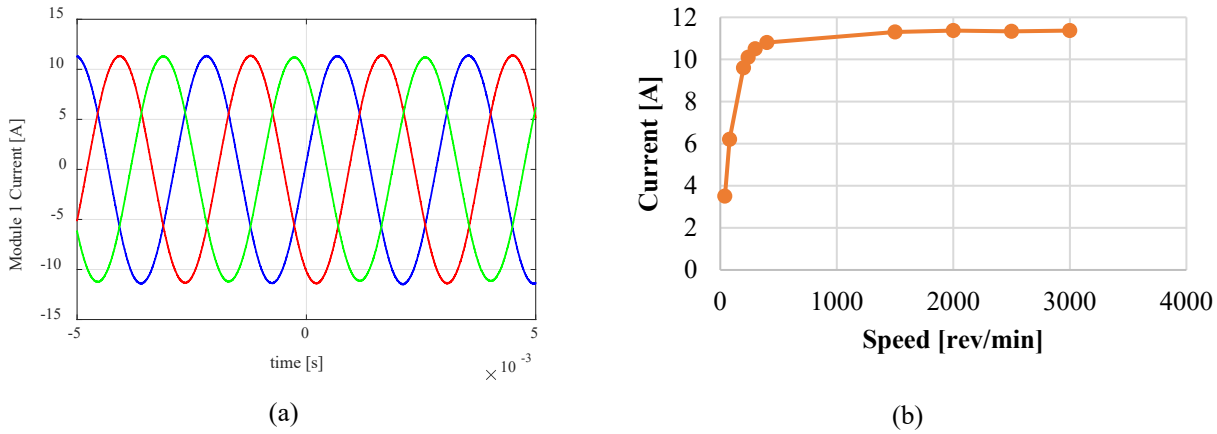

(a) (b)

Figure 4-14.—Measured machine currents after a fault: (a) 3000 rpm module 1 currents; and (b) observed peak current amplitude over tested speed range.

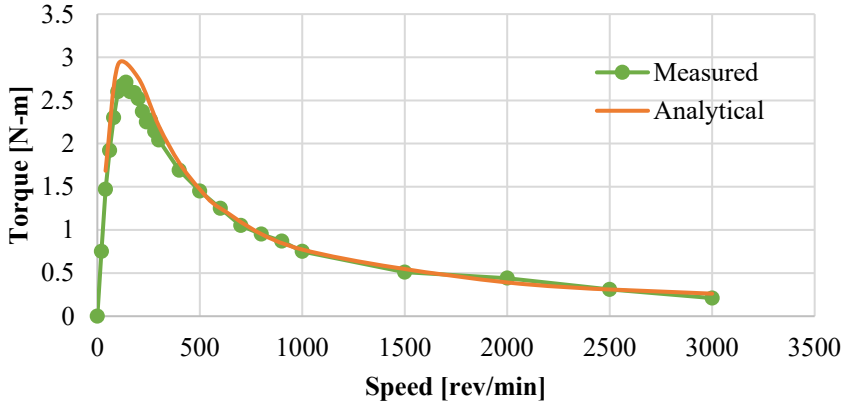

Figure 4-15.—Measured and analytical braking torques for three-phase short circuits applied to modules 1 and 2.

4.4.5 Module Isolation

Finally, the machine's magnetic isolation capability is tested by exciting one module with high frequency current i_{abc1} and measuring the other modules voltage v_{abc2} at zero speed. Since the machine is not spinning (no back emf) and no current is flowing in the machine windings, then the measured voltage on phase v_{a2} equals

$$v_{a2} = M_{lkg} \cdot \frac{d}{dt}(i_{b1} + i_{c1}) \tag{4.3}$$

for adjacent coils current i_{b1} and i_{c1} (for an interleaved configuration) and mutual leakage coupling M_{lkg}. Assuming balanced current I_{s1} on Module 1 and steady state operation allowing derivative terms to be replaced with $j \cdot \omega_e$, leads to a mutual leakage calculation

$$M_{lkg} = \frac{V_{a2}}{\omega_e \cdot I_{s1}} \tag{4.4}$$

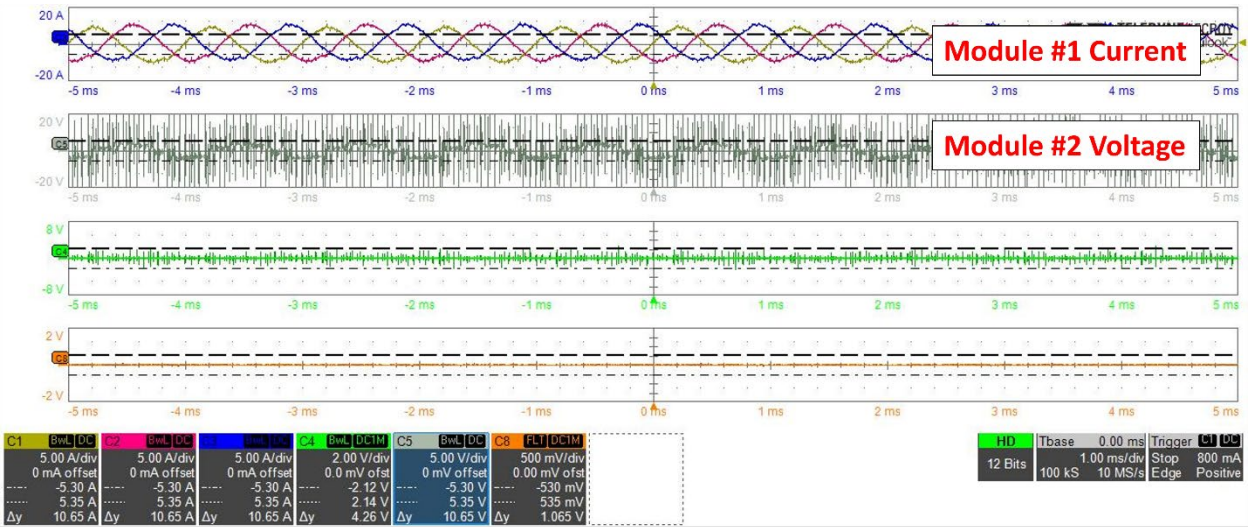

Figure 4-16.—Scope measurement of module 2 open-circuit voltage with module 1 excited with 15.3 A of current at 1 kHz.

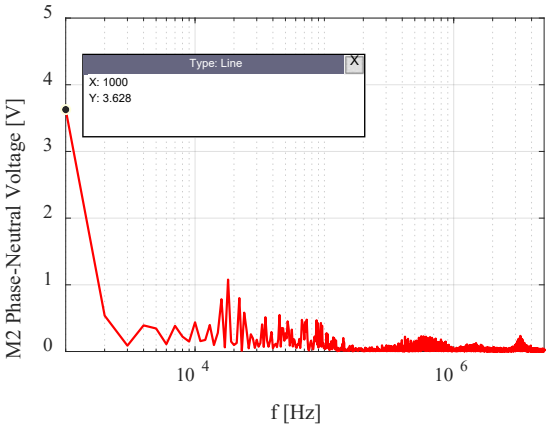

Figure 4-17.—Magnetic isolation test voltage FFT of module 2 phase voltage.

This is implemented experimentally by providing module 1 with 10 A_{pk} of current at 1 kHz and measuring a single phase of Module 2. A scope capture of the measured excitation currents and voltage is shown in Figure 4-16. Significant voltage ripple from Module 1 switching current affects the voltage measurement though a fundamental component is apparent. A frequency analysis of the voltage waveform is completed to extract the 1 kHz component with result share in Figure 4-17. A 3.63 V peak amplitude is observed at 1 kW with other predominant harmonics observed near 20 kHz (drive switching frequency).

Applying Equation (4.4) yields an approximated mutual leakage inductance of 57.8 µH. The ratio of this leakage against the average phase inductance in 4-11 (1.75 mH) results in a module isolation ratio of 3.3 percent—approximately double than the estimate in Section 3.0. The source of the error stems from the method of simulated MIR calculation and differences in saturation state. The presented MIR calculations in this report disable the magnets, resulting in the stator being in a different magnetization state during the calculation. This decision was made to give comparisons between topologies uncoupled from saturation effects. If saturation is considered, then the experimental and simulated MIR metrics agree. Furthermore,

TABLE 4-7.—HEALTHY TEST DATA SUMMARY

Test	Torque [N-m]	Torque Error [%]	Torque Ripple [N-m]	Shaft Power [W]	DC Link Voltage [Vdc]	DC Link Current [Apk]	DC Link Power [W]
FEA, 50% load	3.6	-------	0.4	-------	-------	-------	-------
1000 rpm, 50% load	3.571	0.8%	0.3	374.0	75	5.82	436.5
2000 rpm, 50% load	3.561	1.1%	0.3	745.8	150.2	5.48	823.1
3000 rpm, 50% load	3.540	1.7%	0.4	1112.1	175.1	6.87	1202.9
FEA, 100% load	7.2	-------	0.6	-------	-------	-------	-------
1000 rpm, 100% load	7.079	1.7%	0.5	741.3	75	12.64	948.0
2000 rpm, 100% load	6.997	2.8%	0.5	1465.4	150.2	11.34	1702.3
3000 rpm, 100% load	6.984	3.0%	0.5	2194.1	175.1	14.04	2458.4
FEA, 137% load	9.6	-------	0.4	-------	-------	-------	-------
1000 rpm, 137% load	9.351	2.3%	0.65	979.2	110.3	12.34	1361.1
FEA, 150% load	10.3	-------	0.4	-------	-------	-------	-------
1000 rpm, 150% load	9.949	3.4%	0.69	1041.9	110.3	13.72	1513.3

this highlights the potential negative effects that saturation can have on leakage mutual coupling. Although this metric is degraded, a 3.3 percent MIR is still an appealing level of magnetic isolation for a FT modular machine.

4.5 Healthy Testing

The machine is operated under healthy (non-faulted) conditions to validate torque and thermal performance. This section reviews test results from speeds 1000, 2000, and 3000 rpm capturing torque output for 50 and 100 percent current rating points. An additional two overload points at 1.37x and 1.50x current rating to fully test the developed in-slot cooling methods.

4.5.1 Torque Validation

A summary of measured healthy operating measurements is provided in Table 4-7. Machine phase currents, single phase line-to-neutral voltages, and torque transducer voltage outputs are provided for the 3000 rpm operating point in Figure 4-18 for 50 and 100 percent current. Overloaded operating points can be found in Figure 4-19.

4.5.1.1 3000 rev/min Test Speed

The 3000 rpm 50 percent (7.6 A) and 100 percent (15.3 A) test operating point data is given in Figure 4-18 (for winding configuration #1). This test was completed with a 175.1 Vdc bus. An average torque of 3.540 N-m is observed for the 50 percent load case, which aligns well with the expected 3.6 N-m (1.7 percent error). Based on the measured torques and speeds, the shaft output power is 1112.1 W. An average torque of 6.984 N-m is observed for the 100 percent load case, which is below the expected 7.2 N-m (3.0 percent error). Based on the measured torques and speeds, the shaft output power is 2194.1 W.

A dc bus current of 6.87 A (1202.9 W power in) and 14.04 A (2458.4 W power in) is observed for the 50 and 100 percent test, respectively. This corresponds to measured system efficiencies of 92.5 and 89.2 percent and loss levels of 90.8 and 264.3 W divided between the drive and the machine.

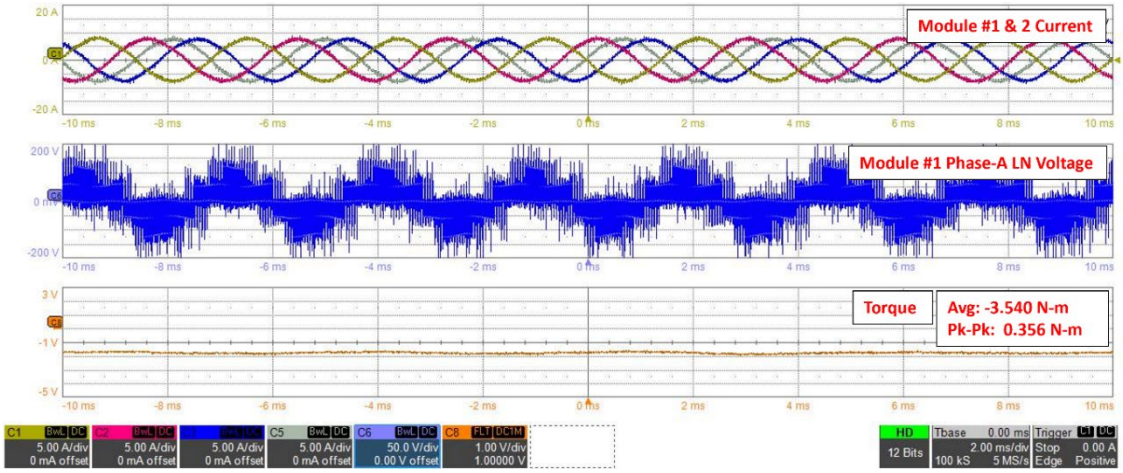

(a)

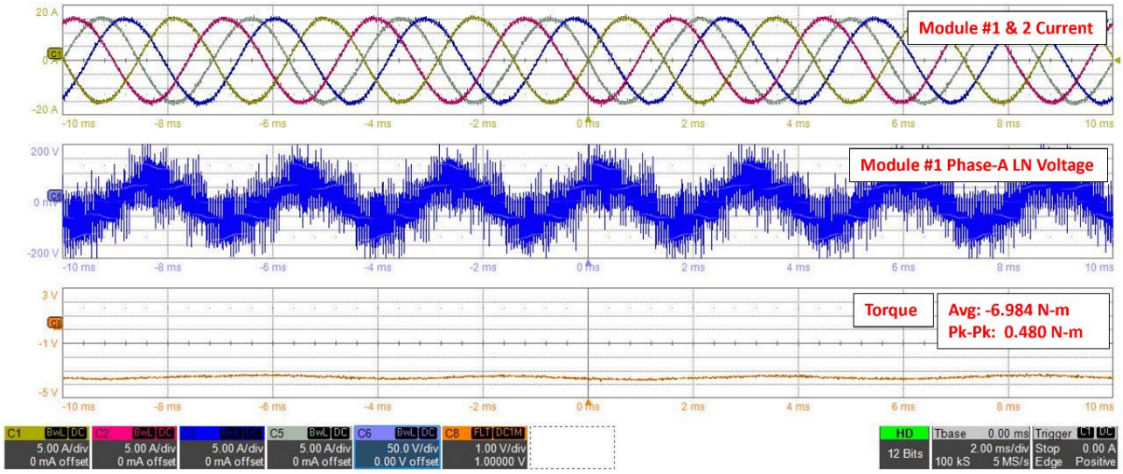

(b)

Figure 4-18.—The 3000 rpm operating points: 50 percent current; and (b) 100 percent current.

4.5.1.2 Overload Testing at 1000 rev/min

An additional two overload points at 1.37x and 1.50x current ratings at 1000 rpm speed are completed (for winding configuration #2) to further test the thermal performance of the machine. Recorded torque, current, and voltage waveforms are given in Figure 4-19. Note the contact resistance related unbalance on module 2 related to the mentioned connector issues above. The dc bus voltage during this test is measured at 110.3 V.

An average torque of 9.351 N-m is observed for the 1.37x overload case (21 A command), which is somewhat lower than FEA calculated 9.6 N-m (2.6 percent error). Based on the measured torque and speed, the corresponding shaft power is 979.2 W.

An average torque of 9.949 N-m is observed for the 1.5x overload case (23 A command), which is also lower than FEA calculated 10.3 N-m (3.4 percent error). At this operating point an apparent resonance was observed on the machine leads causing them to flap. This experiment was cut short after a couple minutes due to a lead short to ground. In any case, the observed average torques reasonably align with the simulated results. Based on the measured torque and speed, the corresponding shaft power is 1041.9 W.

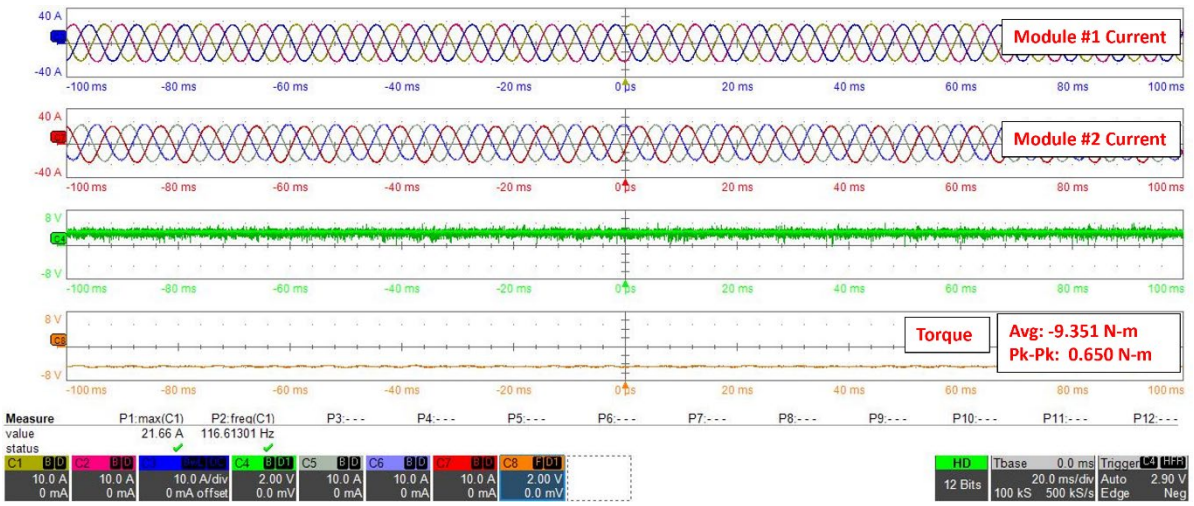

(a)

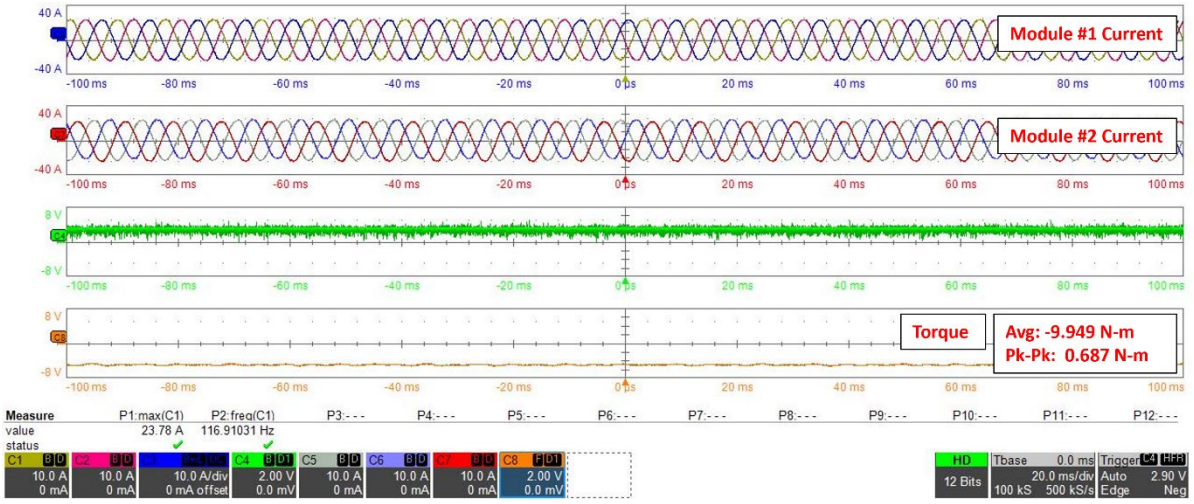

(b)

Figure 4-19.—Overload testing at 1000 rpm: (a) 21 A command (1.37x overload); and (b) 23 A command (1.5x overload).

A dc bus current of 12.34 A (1361.1 W power in) and 13.72 A (1513.3 W power in) is observed for the 50 and 100 percent test, respectively. This corresponds to measured system efficiencies of 71.9 and 68.8 percent and loss levels of 381.8 and 534.1 W divided between the drive and the machine. While these efficiencies are poor, these losses predominately belong to the machine windings approximating 238.1 W for 1.37x overload and 285.7 W for 1.50x overload (assuming room temperature windings).

4.5.2 Thermal Testing

The machine thermal performance is evaluated at each healthy operating point with a limited set of results shared here. Each thermal test is run for 6 to 8 min (approximately when temperature data begins to plateau) to evaluate thermal trends with transient temperature data recorded. The presented set of results correspond to the cases given in Section 3.0 (Table 3-11): 1000 rpm 50 percent current (case 1), 1000 rpm 100 percent current (case 2), 3000 rpm 100 percent current (case 3), and 1000 rpm, 137 percent current (case 6). Results related to the 150 percent overload current case are shared, though this experiment was unable to reach the time threshold mentioned.

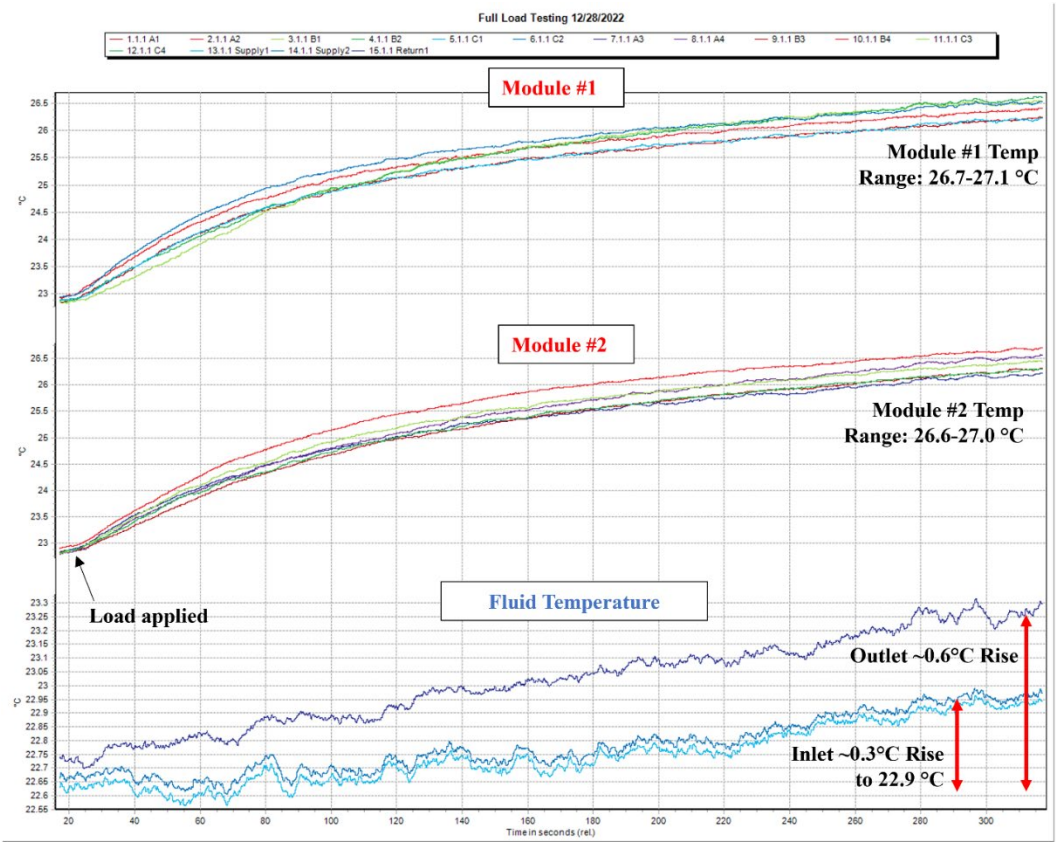

Figure 4-20.—Transient end winding and cooling loop temperature measurement for case 1 load.

4.5.2.1 Case 1: 1000 rev/min, 50 percent current

Machine end winding, supply and return manifold fluid temperatures are measured while the demonstrator machine is operating at 1000 rpm and 50 percent rated current. A transient waveform of the observed temperatures is given in Figure 4-20 for a period of seven minutes after the application of the load.

In general. all machine thermocouple reading transients are similar and generally agree with one another. The peak temperature rise in the winding is 4.2 °C at the end of the recording. This value is expected to slightly increase as the machine reaches final steady state, but strongly tracks with the expected end winding temperature rises presented in idealized model in Section 3.0 (Table 3-11) which estimates a rise of 2.3 to 3.9 °C.

To validate the stated transient assumption, the temperatures from the Figure 4-20 have been fitted with a first-order exponential curve to estimate the thermal time constant. The time constant is estimated to be approximately 120 s. The experimental results shared in this section are measured after six minutes (3x the thermal constant) which should give a valid indication of the final steady state result.

4.5.2.2 Case 2: 1000 rev/min, 100 percent current

Machine end winding, supply and return manifold fluid temperatures are measured while the demonstrator machine is operating at 1000 rpm and 100 percent rated current. A transient waveform of the observed temperatures is given in Figure 4-21 for a period of six minutes after the application of the load. At the end of the recording a maximum end winding temperature rise of 17.2 °C is observed compared to the inlet fluid temperature. Similar to case 1, this tracks well the steady-state FEA result of 9.7 to 15.3 °C temperature rise within the end winding, and a 16.2 °C rise at the winding hot spot.

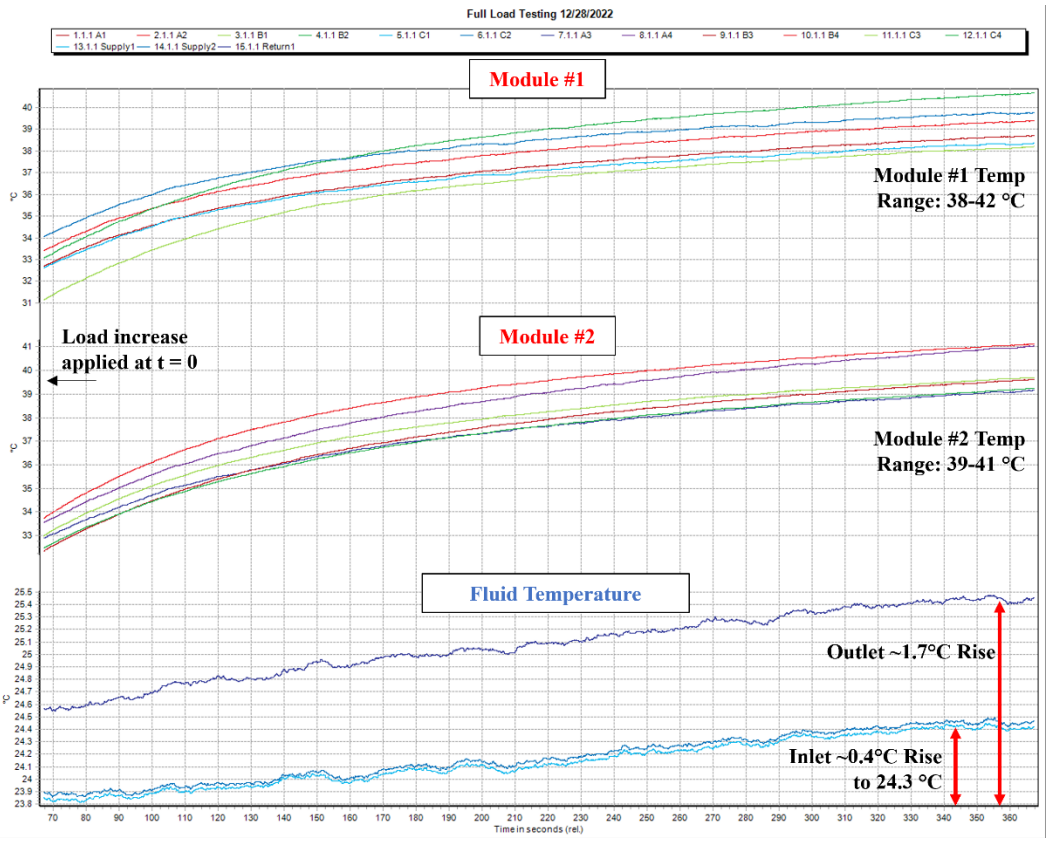

Figure 4-21.—Transient end winding and cooling loop temperature measurement for case 2 load.

4.5.2.3 Case 3: 3000 rev/min, 100 percent current

Machine end winding, supply and return manifold fluid temperatures are measured while the demonstrator machine is operating at 3000 rpm and 100 percent rated current. A transient waveform of the observed temperatures is given in Figure 4-22 for a period of seven minutes after the application of the load. At the end of the recording a maximum end winding temperature rise of 18.7 °C is observed compared to the inlet fluid temperature. This also tracks well the steady-state FEA result of 10.8 to 18.0 °C temperature rise within the end winding. A thermal image of the stator is taken after the test showing a maximum stator temperature of 44.4 °C (or a 20.1 °C rise from fluid temperature) which is close to the modeled 17.2 °C shown in Figure 4-23.

It is worth noting that there is some difference between thermocouple groupings in Figure 4-21 and Figure 4-22. This difference is likely attributable to the unbalanced flows into each of the channels (discussed in the cooling setup section above).

4.5.2.4 Case 6: 1000 rev/min, 37 percent overload

Machine end winding, supply and return manifold fluid temperatures are measured while the demonstrator machine is operating at 1000 rpm and 137 percent rated current. A transient waveform of the observed temperatures is given in Figure 4-24 for a period of eight minutes after the application of the load. At the end of the recording a maximum end winding temperature rise of 31.2 °C is observed compared to the inlet fluid temperature. This measurement tracks on the higher end of the steady-state FEA result of 18.2 to 28.7 °C temperature rise within the end winding, and even closer to maximum FEA coil temperature of 30.6 °C.

The previously observed difference in phase coil temperatures worsens in this case due to the increased heat loads. Once again this difference is related in unbalanced fluid flow in phase ducts (approximately 6 °C between coils).

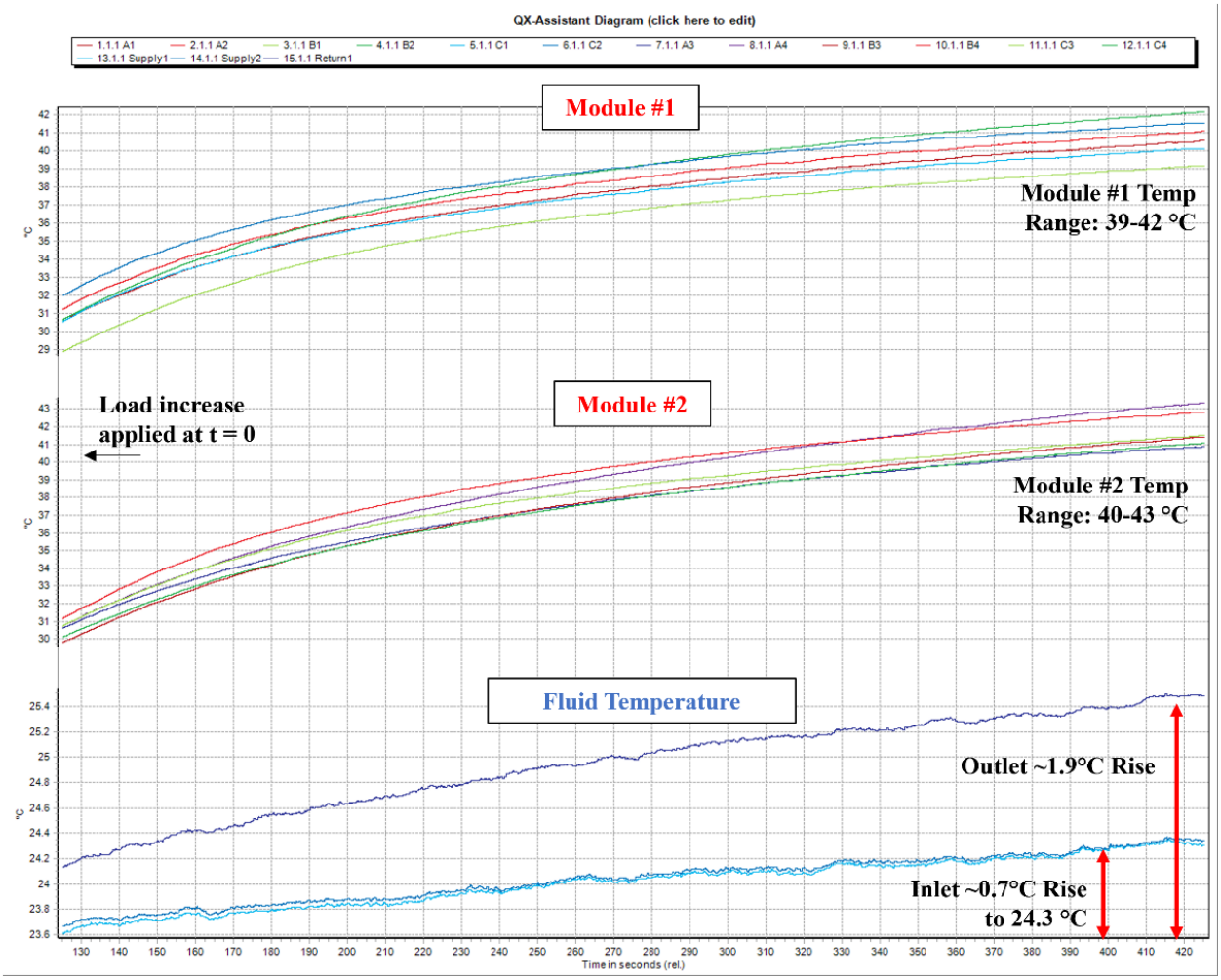

Figure 4-22.—Transient end winding and cooling loop temperature measurement for case 3 load.

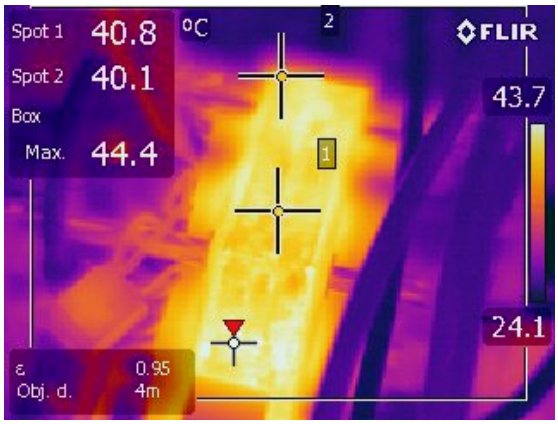

Figure 4-23.—Thermal image of demonstrator stator after case 3 test.

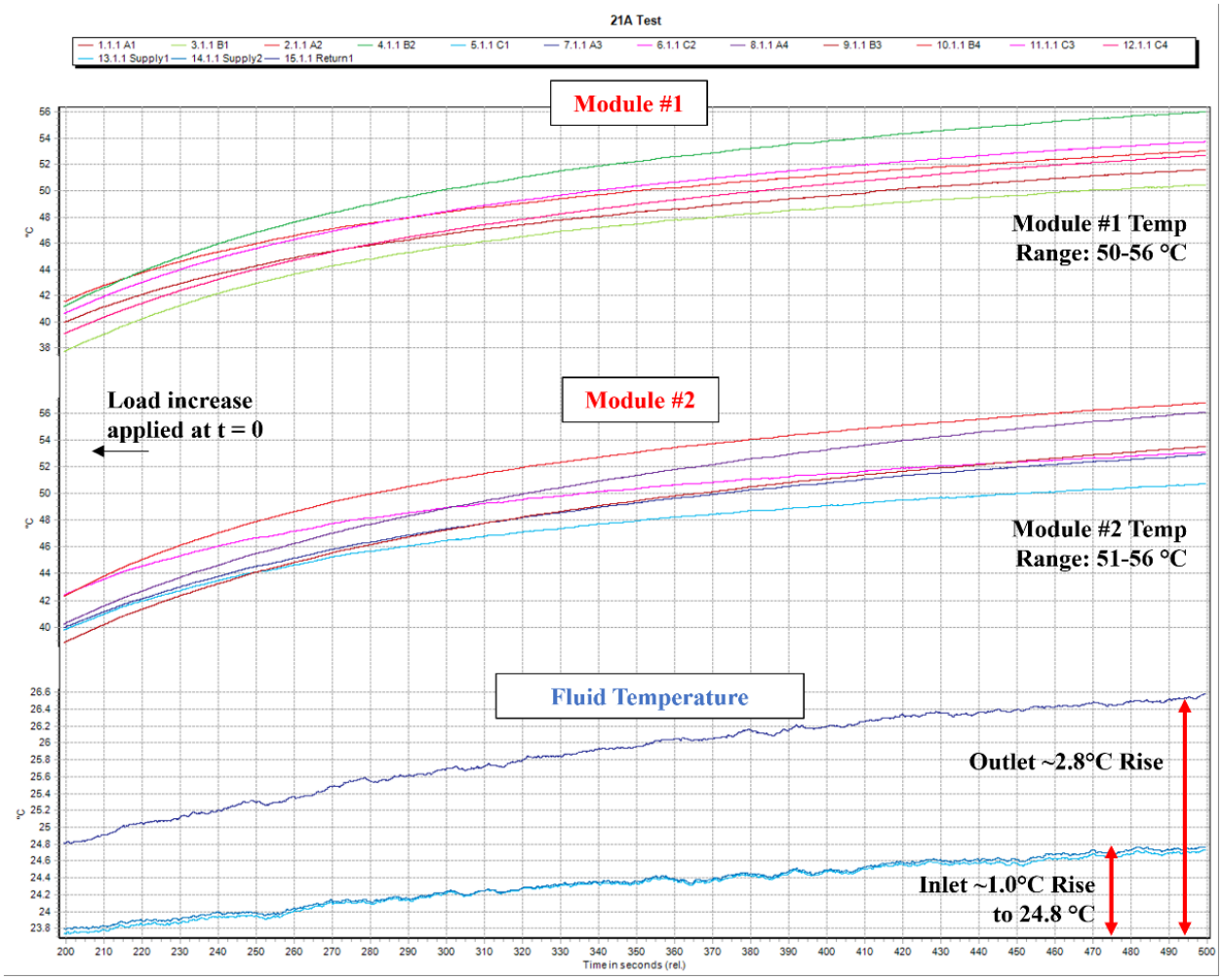

Figure 4-24.—Transient end winding and cooling loop temperature measurement for case 6 load.

4.5.3 Overload Testing: 1000 rev/min and 150 percent Current

Machine end winding, supply and return manifold fluid temperatures are measured while the demonstrator machine is operating at 1000 rpm and 150 percent rated current. Transient measurements are shown in Figure 4-25. The machine only operated in this state for approximately four minutes before a fault unrelated to the thermal system occurred, ending the experiment at that time. Right before the fault the machine reached peak end winding temperatures of 65 °C. The Figure 4-26 thermal image of the stator immediately after the experiment shows the potting material just above the end windings at 62.9 °C validating the measurement. Peak stator core temperature after the test is 52.8 °C.

4.6 Faulted Testing

This demonstrator possesses modular motor drive features representing a class of FT used in applications requiring high reliability, where motor drive expected to continue operation after a stator or power electronics failure. This section summarizes tests completed on the machine under stator failure modes related to terminal open circuit, terminal short circuit, and internal-short circuits between turns. The tests shared in this section are up to 1000 rpm and use configuration 2 module arrangement.

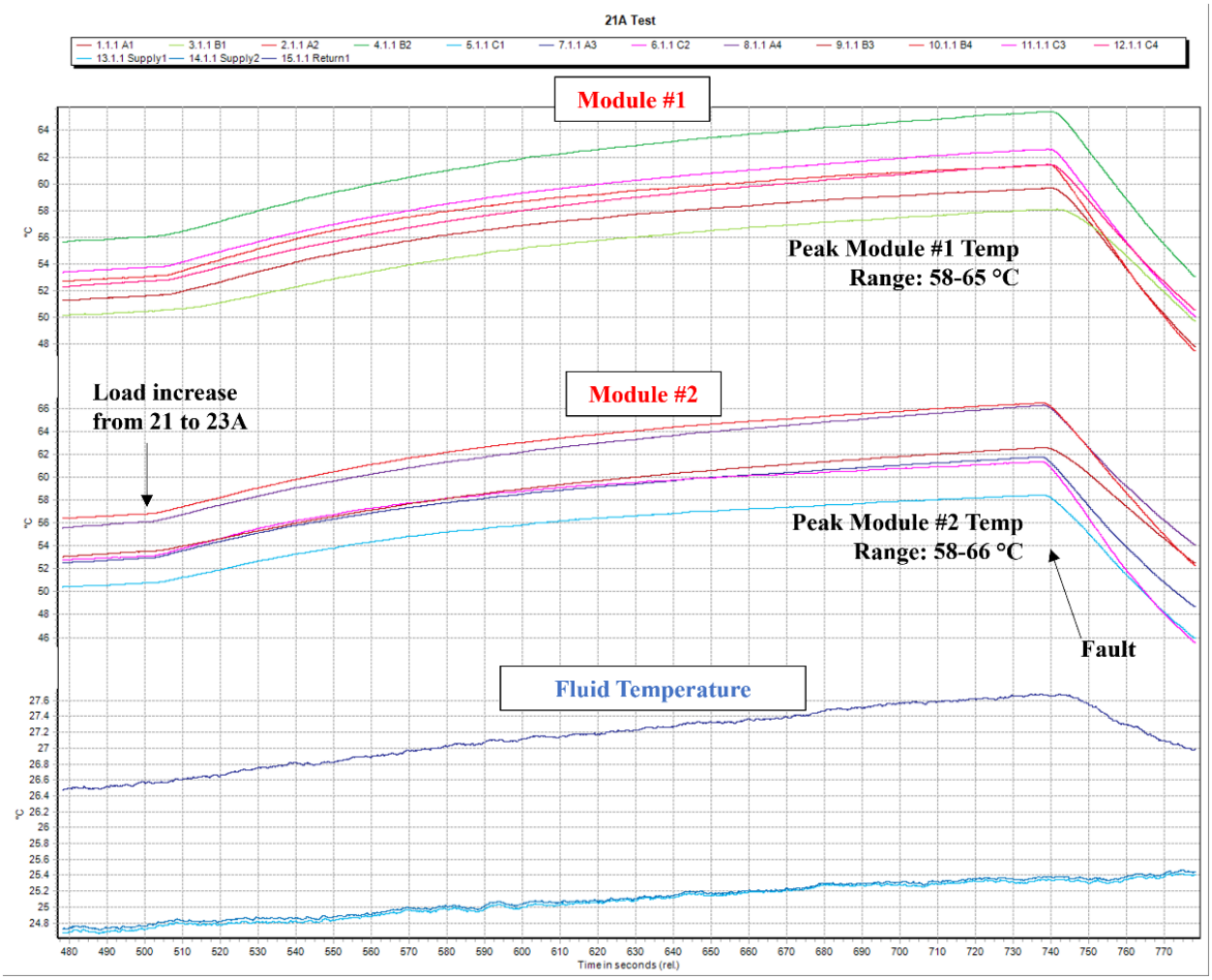

Figure 4-25.—Transient thermal results for 150 percent overload condition.

Figure 4-26.—Stator thermal image after 150 percent overcurrent test.

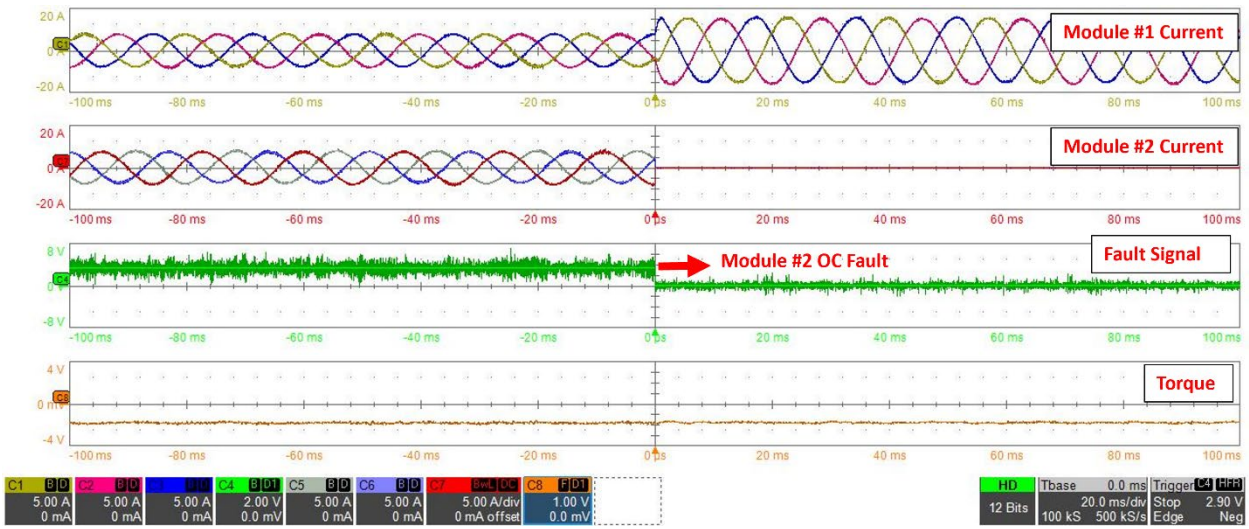

Figure 4-27.—Open-circuit fault demonstration at 500 rpm showing healthy operation, fault event and post fault response.

4.6.1 Terminal Open-Circuit Operation

Perhaps the most benign of the range of faults stated is the terminal open-circuit fault. A demonstration of an open-circuit fault and associated response is shown in Figure 4-27. At t<0, both modules are operating in a healthy state at 50 percent current load. A fault occurs (channel 4 signal dipping to zero) where module 2 is open-circuited. Module 1 immediately responds by increasing its current by a factor of 2 to make up for the lost module without any interruption in shaft torque or noticeable difference in torque ripple. The test results in Figure 4-27 demonstrate the developed modular motor drive system is capable of FT operation during open-circuit transients.

4.6.1.1 Module Thermal Isolation

Thermal isolation between phases is a critical aspect of FT machine design. The developed design uses in-slot cooling channels to thermally buffer interactions between modules in the event of a failure. This is demonstrated under a full-current open-circuit test where module 2 is open-circuit and module 1 delivers rated current—matching the post fault condition in Figure 4-27.

Thermocouple transients are shown for this condition in Figure 4-28. The healthy module temperatures rise to expected levels observed under 100 percent current conditions (nearing 40 °C) while the open-circuit coils remain at lower temperatures near the coolant temperature (and in fact are still being cooling from a previous test). The observed sustained difference in temperature agrees with the thermal isolation simulation results in Section 3.0.

A similar thermal response is expected for a terminal short-circuit faults on module 2. Primary difference being the module 2 temperatures will rise to temperatures related to the characteristic current I^2R losses. For this reason, thermal isolation discussions related to terminal faults is limited to the presented open-circuit demonstration.

4.6.2 Terminal Short-Circuit Operation

A more serious failure mode for PMSMs is high current transients from a terminal three-phase short-circuit and post-fault characteristic current that can potentially demagnetize rotor magnets. The required steps for mitigating these risks were taken for this machine design: high inductance to minimize fault

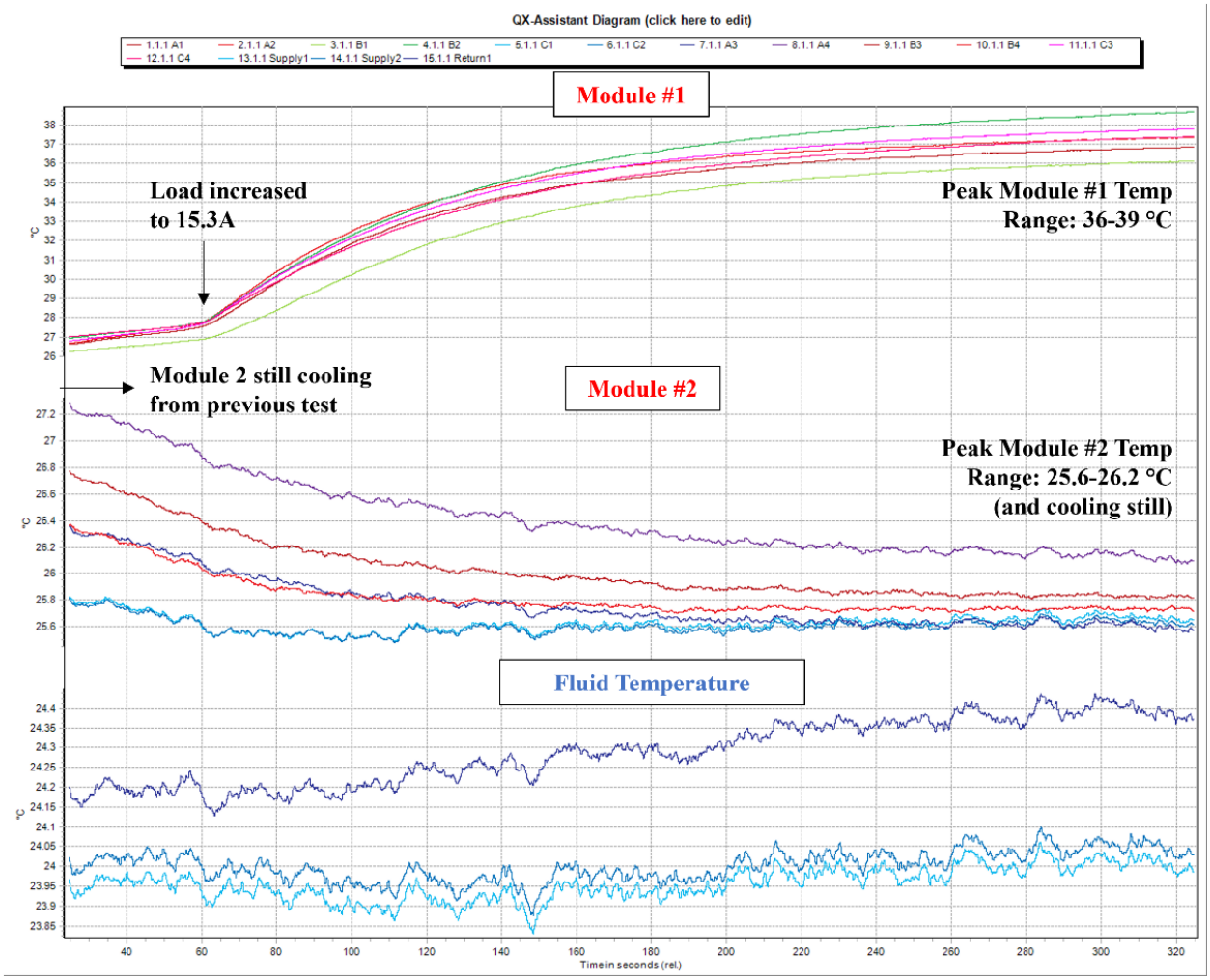

Figure 4-28.—Thermal isolation demonstration under full-load module 2 open-circuit fault.

currents, and magnet material selection with strong coercivity at high temperatures to withstand peak transient currents 3x rated current.

The short-circuit characteristics of the built machine is presented above confirming characteristic current calculations. This demonstration follows a similar methodology to the open-circuit case shared in Figure 4-27, both modules operate under healthy conditions until a t = 0 where the terminal short-circuit is applied. The healthy module responds by increasing its current to compensate for the lost torque. The results of the test are shown in Figure 4-29. After the application of a three-phase short, a peak transient current of 15.3 is observed. Additionally, the overall output torque of the machine is reduced after the fault due to braking torque from the shorted module. Complete machine (both modules shorted) braking characteristics are measured in Figure 4-15. Further, module #1 healthy currents are balanced and unaffected by adjacent faulted coils. The test results in Figure 4-29 demonstrate the developed modular motor drive system is capable of FT operation during short-circuit transients.

4.6.3 Internal Short-Circuit Operation

Internal short-circuit faults are the final fault mode considered for this FT demonstration. For PMSM machines these faults can be devasting due to significant current being driven through shorted turns by the

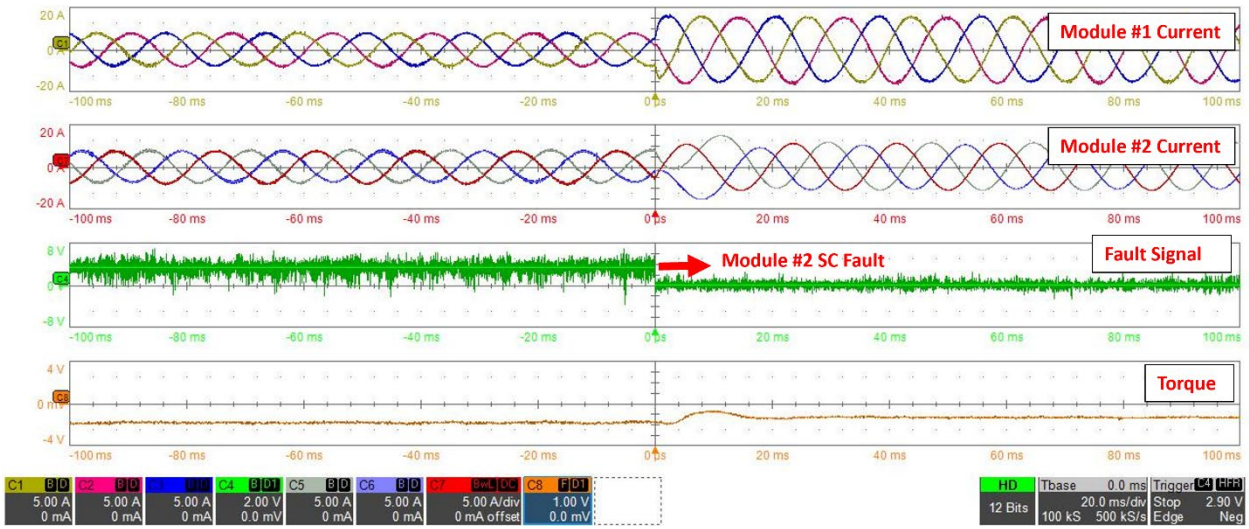

Figure 4-29.—Short-circuit fault demonstration at 500 rpm showing healthy operation, fault event and post fault response.

TABLE 4-8.—FAULTED TURN COMBINATIONS

Studied Faulted Turn Combinations
Turn 27—Turn 44
Turn 27—Turn 36
Turn 44—Turn 47

TABLE 4-9.—FAULT RESISTANCE USED IN TURN-TO-TURN FAULT STUDY (20 °C)

External Fault Resistor Label	Resistance Measurement (Ω)
RF5	5.12447
RFp22	0.22845
RF0	direct short

rotor permanent magnets. To study these faults, three-turns are brought out of a single phase in module 2 allowing for the external application of faults. Initial testing is passive (no drives) where the amplitude of fault current for varying fault resistance is measured 1000 rpm. After, an active turn-to-turn fault demonstration is completed using the developed modular drives.

4.6.3.1 Passive Turn-to-Turn Fault Testing Parameters

Turns 27, 36, and 44 are tapped from the end winding of phase A4. Measured turn resistances are given in Section 4.4.1. The studied turn-to-turn fault combinations are provided in Table 4-8. Power resistors are used to simulate expected fault resistance with values given in Table 4-9. Each of the faulted turn combinations in Table 4-8 is tested with the resistors defined in Table 4-9. A final test will be conducted with turns directly connected.

The turn-to-turn fault resistor is connected to the studied faulted turns before spinning the machine. For each resistance, speed is ramped up to 1000 rpm or until fault current exceeds 32 A (approximately 2x the rated current) to avoid damaging the machine. Peak amplitudes of fault current are recorded.

4.6.3.2 Passive Turn-to-Turn Faults (0-1000 rev/min)

The observed peak currents for the above faulted turn scenarios are plotted in Figure 4-30 for each of the different resistance and fault combinations stated above.

The results in Figure 4-30 show how quickly fault currents develop with speed in the event of an internal short circuit and it is clear to see how these can faults can quickly become destructive. In the case of the turn 27-36 fault scenario, testing was halted at 800 rpm due to the rapidly increasing currents exceeding the defined current thresholds.

Other observations include higher fault currents at lower speeds for turns 27-44 faults, though the observed current begins to plateau at higher speeds for a direct short. Conversely, the turns 44-47 case had the lowest observed currents. At higher speeds, it is expected the 44-47 fault currents will dominate. Next, although not clear from Figure 4-30, there is observable current through the 5 Ω fault resistor in all cases, reaching as much as 0.625 A at 1000 rpm for the 27-44 fault scenario.

For all tests, audible noise and vibration were observed for higher amplitude fault currents further highlighting some of the possible techniques for fault detection.

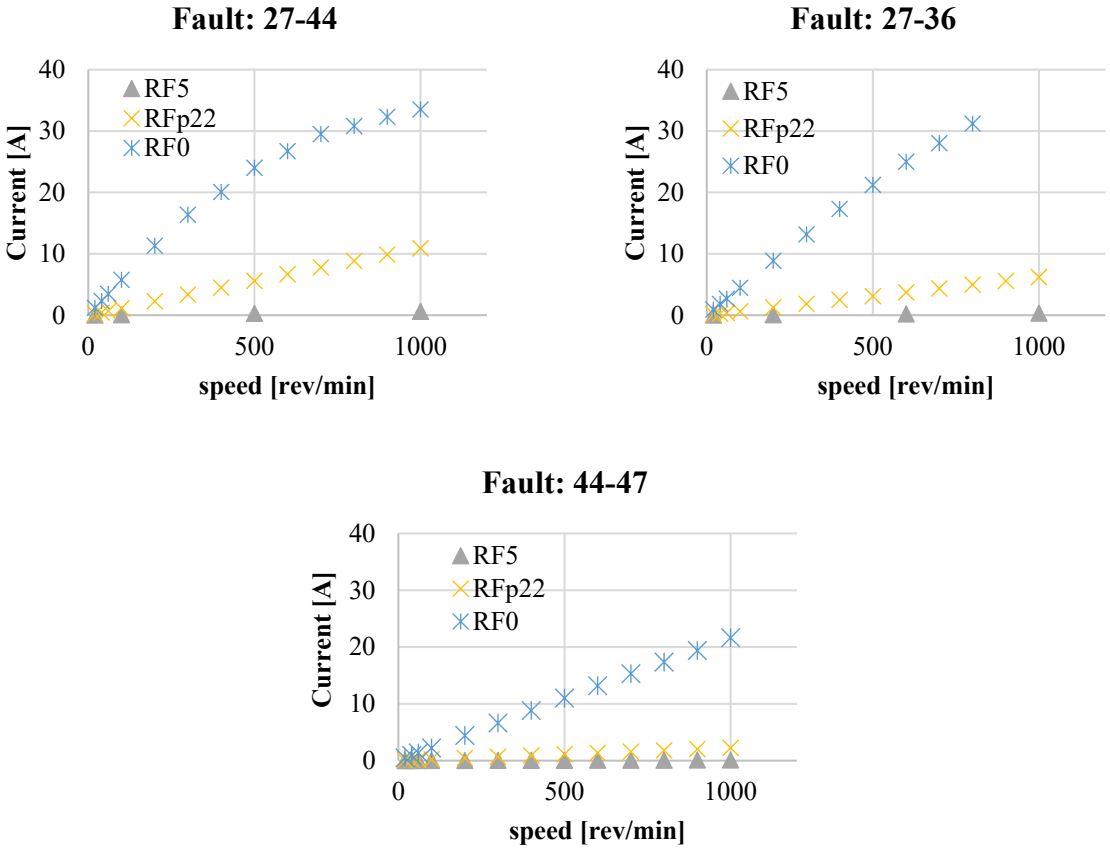

Figure 4-30.—Peak short-circuit currents for varying fault resistances.

4.6.3.3 Turn-to-Turn Fault Thermal Isolation

The passive turn-to-turn fault testing allows for additional evaluation of the proposed thermal isolation scheme. This is illustrated for the turn 27-44 direct short fault test at 1000 rpm corresponding to peak fault current 33.5 A. Thermocouple measurements of the fault transient are shown in Figure 4-31. The faulted coil temperature rises dramatically in 2 min while only minor increases in temperature are observed in adjacent coils (~0.3 °C).

This experiment demonstrates the specific role in-slot cooling has in fault tolerant machines for higher levels of fault current (e.g., single turn faults at high speed): in-slot cooling provides sufficient thermal isolation on a transient basis to blunt the impact of elevated fault related losses, giving time for the implemented fault detection scheme to identify the problem and react.

4.6.3.4 Internal short-circuit operation response

The response to an internal short circuit is demonstrated for a direct short between turns 44-47 at 500 rpm in Figure 4-32. Before t = 0, the machine is operating in an undetected fault state with a sustained internal short inside Module 2 phase A. At t = 0 the fault is detected and a three-phase terminal short is applied to the windings, suppressing the faulted turn current. Healthy module 1 responds by increasing its phase current to compensate for the lost module 2 torque contributions.

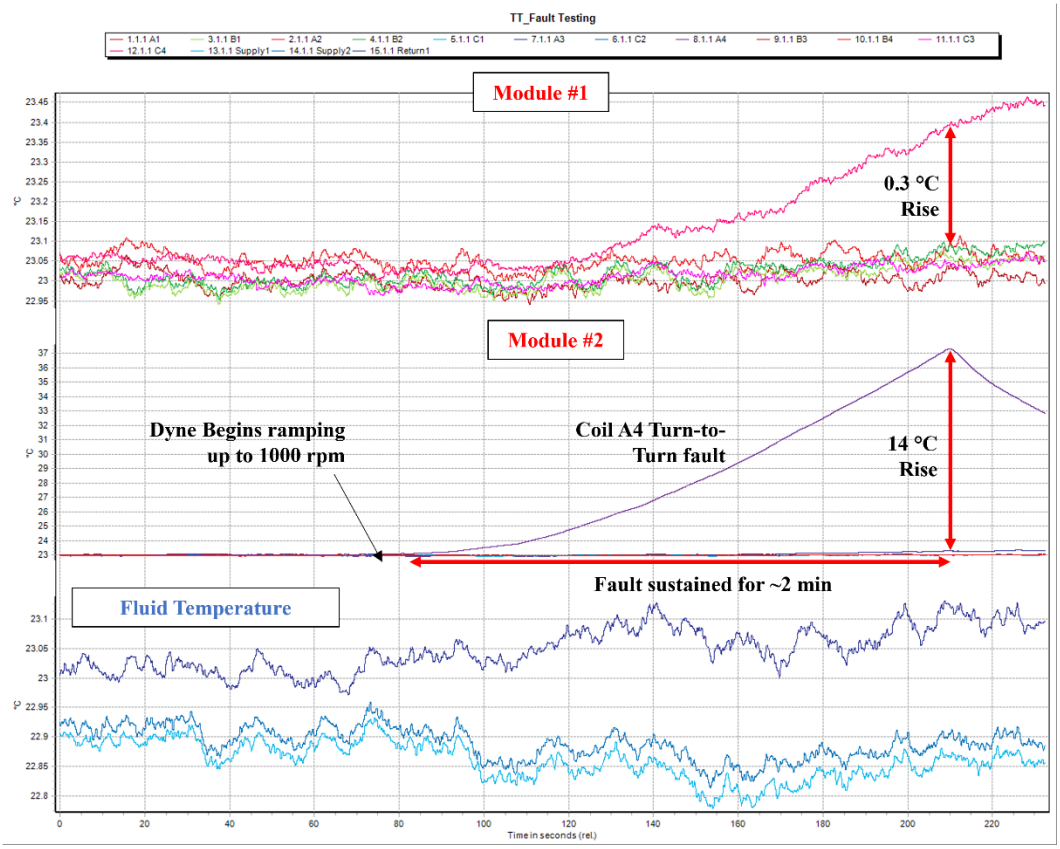

Figure 4-31.—Thermal transient during turn-to-turn fault between turns 27 and 44 inside A4.

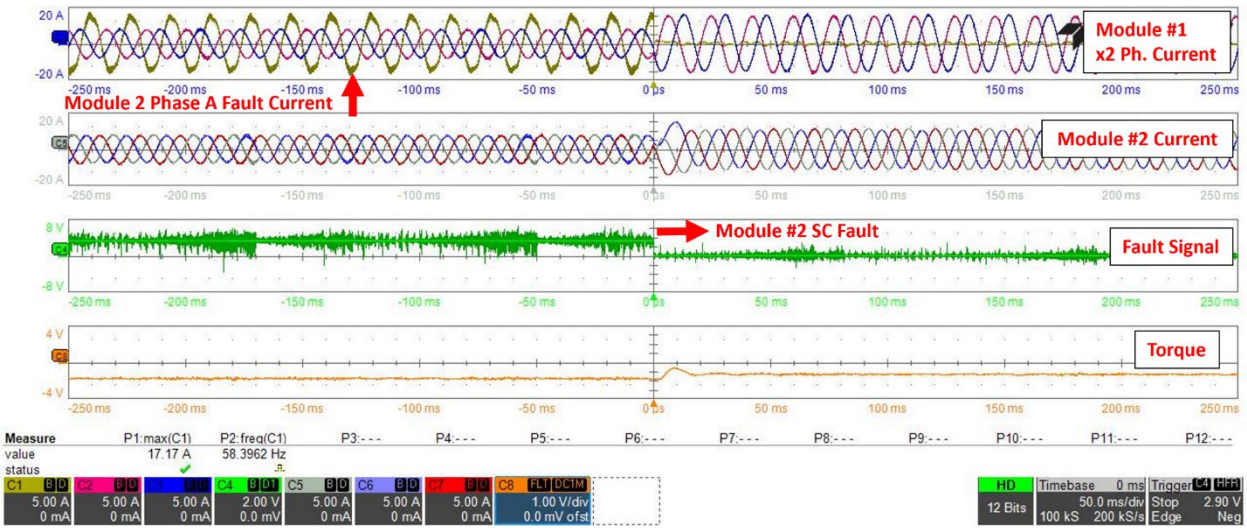

Figure 4-32.—Internal Short-circuit fault demonstration at 500 rpm showing internal short-circuit current, fault response trigger and post fault response.

4.7 Summary

This section has presented the experimental results from testing a low-power fault-tolerant demonstrator machine that incorporates the electromagnetic isolation and in-slot cooling features which lie at the heart of this research program. These features include the introduction of flux barriers in the stator back-iron, an asymmetric tooth tip implementation that minimizes the leakage flux between phases and maximizes the self-leakage inductance, and an in-slot heat exchanger to cool the windings using alumina tubes. Details related to the fabrication and test configuration have been presented. A brief overview of the machine parameters (discussed in greater detail in Section 3.0) and the aforementioned features has been provided together with the developed test plan.

The experimental test program has succeeded in accomplishing the following objectives arising from the analytical results presented in Section 3.0: (1) validation of the designed machine equivalent circuit parameters; (2) validation of the predicted electromagnetic isolation; (3) validation of the rated torque output; (4) validation of the predicted thermal performance at defined operating points; (5) successful demonstration of fault tolerance capabilities for terminal and internal short-circuit fault modes; (6) demonstration of the desired thermal isolation; and (7) validation of the self-dyne concept for modular machines. Key observations are summarized in the following paragraphs.

Designed machine resistance, magnet flux linkage, inductance, and characteristic current values were all confirmed to be within 3 percent of predicted values via static measurements and rotational testing. Electromagnetic isolation was confirmed by locking the rotor and applying high-frequency current to one module and measuring the open-circuit voltage of the other module. These tests resulted in a measured Module Isolation Ratio MIR value of 3.3 percent which is higher than the original design value due to saturation, but still quite appealing for MMD applications and a strong indicator of high electromagnetic isolation. The rated machine torque operation was confirmed via dyne testing up to 3,000 rpm. For the tested operating points (< 15.3 Apk per module), the observed torque is within 3 percent of the predicted values. For overloaded operating point #3, the observed torque is within 5 percent of the design value.

Thermal performance has been tested by operating the machine under load for extended periods of time. The presented results track well with the idealized model in Section 3.0, but the measured temperatures are slightly higher than the predicted values. This can likely be attributed to lower operating coolant flow rates than initially planned, combined with the impact of simplifying assumptions made in the

Section 3.0 model. Overall, the observed test temperatures are well below maximum temperature ratings of the utilized components.

The machine fault tolerance capability has been successfully validated via a series of fault demonstrations. These include the sudden application of terminal faults (open- and short-circuit) during healthy testing and observations of the resulting post-fault responses. These demonstration tests were extended to turn-to-turn faults that were intentionally applied, and the machine response was observed.

Part of this fault tolerance demonstration included examining coil temperatures during fault events and determining whether there are significant thermal interactions between healthy and faulted coils. The presented results show these interactions are minimal, confirming that the implemented thermal isolation technique using in-slot cooling tubes is a promising approach for realizing both effective coil cooling and high-quality thermal isolation.

5.0 Fault Tolerance Figures of Merit

The original report reliability analysis in Reference 4 presents an approach with a predominant focus on modular machines with multiple independent sets of three-phase windings. However, there are numerous candidate FT topologies for power electronics and electrical machines that have been presented in the literature, but an established methodology for selecting a preferred motor drive FT approach for a given application does not exist. To illustrate, the FT motor drive concepts shown in Figure 5-1(a) all can operate in a remedial state such as the one identified in Figure 5-1(b). Each Figure 5-1(a) FT system is capable of continued operation after a motor drive failure, but the preferred approach for a given application is not readily determined without clear criteria for making the selection.

Figures of Merit (FoMs) provide a useful method to evaluate the goodness of electrical machines and drives for achieving performance objectives. For example, FoM performance metrics such as machine shear stress and winding current density are commonly used to evaluate the electromagnetic and thermal performance of electrical machines (Ref. 22). For power electronics components, Baliga FoMs in References 23 and 24 are often used to compare the capabilities of power semiconductor switch devices at

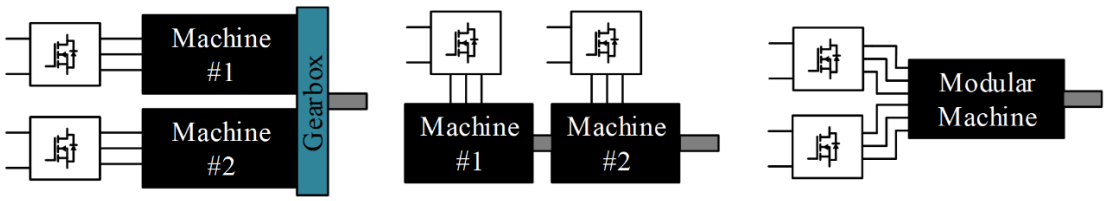

(a)

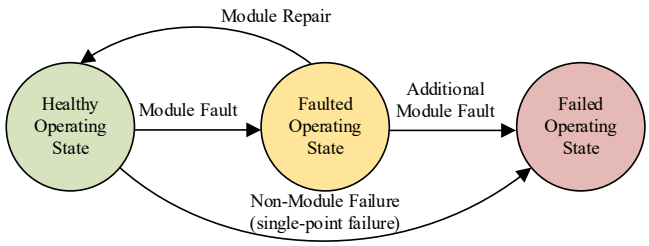

(b)

Figure 5-1.—(a) Example of FT machine drive topologies: direct redundancy using two machines and a shared gearbox (left), two stators on a common shaft (center), and modular machine drives (right); (b) State diagram showing operating states (healthy, faulted, and failed) of a FT system and corresponding transitions.

high switching frequencies. For FT machine drives, FT performance/degradation FoMs have been proposed in the literature, including the Silicon Overrating Cost Factor (SOCF) and the Fault Power Rating Factor (FPRF) in Reference 25.

This section proposes a set of fault tolerance FoMs (FT-FoMs) to better quantify and compare the achievable system reliability benefits of candidate motor drive topologies, including the impact of undesired performance penalties (e.g., component overrating) in an attempt to expand and enhance the more specialized performance-oriented metrics defined in Reference 25. The intent of these metrics is to provide users some new tools to perform high-level quantitative comparisons between candidate FT topologies that can be helpful for carrying out down-selection exercises. This section also provides a proposed procedure for calculating and applying these metrics using Markov Chains, as well as a discussion on how to use the proposed metrics with FT machine drive topologies.

Before introducing the definitions of these FT-FoMs, some guidelines are provided to help inform potential users about some of the key characteristics of these metrics, the parameters that affect their values, and, finally, their design value and limitations.

1. The units of these FoM metrics vary widely and depend entirely on their definitions. While several are unitless because they are ratios of two parameters with the same units, others have unusual units such as hr/kg.
2. The quantitative values of the FoM metrics vary widely among the metrics, and any attempt to compare the quantitative values of two different FoM metrics is a futile exercise. The value of these figures of merit comes from comparing the quantitative values of the same FT-FoM metric for different candidate fault-tolerant motor drive topologies.
3. All of the FoM metrics in this report have been defined so that higher values are better when comparing their values among different candidate topologies for the same FT-FoM metric.
4. Each FoM metrics is defined so that its value for a candidate topology depends on the ratio of the topology's mean time to failure (MTTF) to one of the other performance metrics such as the MTTF of the motor drive modules, the frequency of repairs, the likelihood of single-point failures, etc. As a result, the "winning" topology for one of the FT-FoM metrics among a group of topologies that all share the same set of parameters may no longer be the winner for a different FT-FoM where the performance metric used to evaluate the FoM metric is changed.
5. The values of the FoM metrics depend heavily on the basic parameter values (e.g., module failure rate, repair rate, and single-point failure rate) assumed for a candidate FT configuration. As a result, the ranking order of several candidate FT topologies evaluated for any selected FoM metric can change significantly as the values of these basic parameters are changed. This highlights the observation that the sensitivity of any chosen FoM metric to changes in any of the parameters, such as repair rate, can be conveniently investigated.

5.1 Proposed Fault Tolerance Figures of Merit (FT-FoMs)

The goal of the developed FoMs is to provide quantifiable metrics to simultaneously evaluate the reliability improvement delivered by a candidate FT motor drive topology and the degree to which these improvements are offset by selected performance penalties associated with the topology (e.g., number of parts, component derating, frequency of service, etc.). In general, these Fault Tolerance FoMs take the form

$$\text{FT-FoM} = f(\Delta\text{Reliability, Performance Impact}) \tag{5.1}$$

when the reliability and performance impacts are estimated and quantified using analytical formulas. This allows the user to perform quantifiable high-level comparisons of candidate topologies in order to perform down-selections for specific application.

In real applications, it is impractical to define a single universal FT-FoM that can be trusted to carry out the down selection process due to the complexities and nuances of the candidate FT motor drive topologies and the intended application. Given this reality, three sub-classes of FT-FoM metrics are proposed in this report to help evaluate and distinguish FT topologies in terms of their reliability improvements and offsetting performance penalties. In total, seven distinct FT-FoM metrics are presented that can be used to draw comparisons between FT topologies, or customized to better fit the user's needs. These includes two FoM metrics focused on evaluating the topology's reliability improvement features, two highlighting the candidate topology's single-point failure (SPF) and repairability characteristics, and three designed to evaluate the topology's reliability-performance tradeoffs.

5.1.1 System Reliability Metrics

The first sub-class of FoM metrics is focused on assessing the reliability improvement of candidate FT motor drive topologies. The first metric $FTFOM_1$ is defined as

$$FTFOM_1 = MTTF / MTTF_{std} \quad [\text{unitless}] \tag{5.2}$$

where the candidate FT motor drive's Mean Time to Failure (MTTF in hours) is compared with the expected MTTF of the baseline (standard) topology without fault-tolerant features, $MTTF_{std}$, by taking the ratio of these two values. This metric provides a first-pass quantified indicator for evaluating the level of expected reliability benefits achieved by replacing a baseline topology with a more fault-tolerant alternative. The higher the value of $FTFOM_1$, the greater the benefits of the topology's FT features for improving the motor drive's system reliability compared to the selected baseline (typically a two-level VSI).

The second FoM metric in this sub-class is $FTFOM_2$ that quantifies the improvement of the motor drive system reliability achieved by a candidate topology over that of the baseline topology ratioed to the reliability of the group of modular drive units that comprise the candidate topology (i.e., the level of reliability improvement achieved by adopting a modular topology with repairable drive unit modules). $FTFOM_2$ is defined as

$$FTFOM_2 = \Delta MTTF / MTMF \quad [\text{unitless}] \tag{5.3}$$

where the improvement in the candidate topology's MTTF over that of the baseline topology, $\Delta MTTF$, is expressed as

$$\Delta MTTF = MTTF - MTTF_{std} \quad [\text{hrs}] \tag{5.4}$$

and the module group mean time to failure (MTMF) is defined as the expected time to the first failure of the total population of n_m identical FT drive modules used to implement the candidate topology. That is, if the mean time to failure of a single module is $MTTF_m$, then the value of the MTMF would be $MTTF_m / n_m$ assuming that all of the modules are operating under the same baseline conditions. Summarizing, this metric can be interpreted as the reliability improvement achieved by a candidate topology normalized by the mean time to the first failure among the group of n_m modular drive units. A higher value of $FTFOM_2$ is desirable

because it indicates that a candidate FT topology is achieving a larger increase in its system MTTF for the same value of module group mean time to failure (MTMF).

5.1.2 Single Point Failure and Repairability Characterization Metrics

The two FT-FoM metrics in the second sub-class, $FTFOM_3$ and $FTFOM_4$, are useful for assessing the impact of single point failures (i.e., failure modes that bypass the FT modular drive components) and the system repair rate (i.e., the frequency of repairing faulted modules) on the overall drive system reliability.

The first of these two FoM metrics, $FTFOM_3$, is defined as

$$FTFOM_3 = MTTF/MTTSPF \qquad [\text{unitless}] \tag{5.5}$$

where Mean Time to Single Point Failures (MTTSPF) represents the expected time to failure for non-redundant components in the drive system (e.g., bearings in a standard motor). A $FTFOM_3$ value that is close to one indicates that a candidate FT drive topology is predominantly determined by the single point failure rate. This means that increasing the number of redundant modules or improving the repair rate will have a negligible effect on increasing the drive system MTTF value. As a result, the value of $FTFOM_3$ is valuable for helping the user to decide whether reliability improvements efforts should be focused on reducing single point failures or improving the FT module reliability and/or repair rate.

The second of these FT-FoM metrics, $FTFOM_4$, provides a measure of the sensitivity of a candidate FT drive topology's MTTF value to the drive system's repair rate. It is defined as

$$FTFOM_4 = MTTF_{HR} \,/\, MTTF_{NR} \qquad [\text{unitless}] \tag{5.6}$$

where $MTTF_{HR}$ is the candidate topology's MTTF with a specified high repair rate, and $MTTF_{NR}$ is the topology's MTTF value without any repairs. A FT candidate system with a higher value of $FTFOM_4$ indicates that it is benefiting more from a selected repair rate compared to another topology with a lower $FTFOM_4$ value evaluated at the same repair rate.

5.1.3 Reliability/Performance Tradeoff Metrics

The third and final sub-class of FoM metrics provides a means of quantifying the reliability improvement achieved by a candidate FT drive topology in comparison to a second metric that represents a performance penalty (e.g., mass) of the candidate topology. Each of these reliability/performance FoM metrics takes the following form

$$FTFOM = \frac{\Delta MTTF}{P} \tag{5.7}$$

where P is any quantifiable performance penalty metric that applies to the candidate topology. Three examples of this sub-class of FT FoMs that are applicable to aerospace propulsion applications are defined in this section using the following three performance penalty metrics of candidate FT drive topologies: FT drive system mass, module steady-state power overrating, and topology maximum steady-state kVA output power capability.

Minimizing the added system mass (Δkg) associated with the incorporation of FT features is arguably the most important performance penalty in aerospace applications. The first of the reliability/performance FT-FoM metrics, $FTFOM_5$, directly captures this tradeoff by forming the ratio of the MTTF improvement

achieved by the candidate topology to the mass penalty Δkg (i.e., increase in FT topology mass above baseline system mass):

$$\text{FTFOM}_5 = \Delta\text{MTTF} / \Delta\text{kg} \qquad [\text{hrs/kg}] \tag{5.8}$$

Unfortunately, determining the mass penalty Δkg in (5.8) is often difficult during concept studies and not easily determined using analytical formulas. In this situation, the use of power overrating factors can be used as a simplified stand-in for the mass penalty. Such overrating factors also have a correlation with the cost of the fault-tolerant drive system which is another important overall drive system metric that may be more important than mass in some applications.

Throughout this study, it is assumed that a FT drive system requires module power overrating compared to a baseline drive without fault tolerance in order to maintain output performance equivalent to that of the original healthy drive system until the system enters its final failed state. It can be expected that this power overrating will be accompanied by increased mass, volume, and cost due to the impact of the increased combined power rating of the components used to build the FT drive system. A basic overrating factor *F* is defined in Reference 4 to capture the impact of this overrating of both the machine and power electronics in a simplified manner. This leads to the second FT-FoM in this sub-class, FTFOM_6, that is defined as the ratio of the candidate FT topology's MTTF improvement to its overrating factor, expressed as

$$\text{FTFOM}_6 = \Delta\text{MTTF/F} \qquad [\text{hr}] \tag{5.9}$$

A candidate FT topology with a high value of FTFOM_6 indicates that it can provide a larger improvement in the drive system mean time to failure with a smaller amount of module steady-state power overrating than other topologies.

A modified version of this FT-FoM metric can be defined using a different version of the overrating factor that focuses on the total cumulative steady-state kVA rating of the power electronics inverters in a candidate FT topology compared to the kVA rating of the single module inverter in the baseline (standard) topology. This alternative kVA overrating factor, KVAOF, is defined as

$$\text{KVAOF} = \frac{\text{Summed total kVA ratings of all inverter modules}}{\text{kVA rating of inverter in baseline design}} \qquad [\text{unitless}] \tag{5.10}$$

Where all of the kVA ratings are based on steady-state operation. This KVAOF overrating factor reflects the same overrating characteristics captured by the overrating factor *F* but does so with an additional level of detail by focusing on the total cumulative kVA ratings of the power electronics modules included in a candidate FT topology rather than simply using the number of modules. This leads to a different version of the overrating FoM metric in Equation (5.9) that is expressed as

$$\text{FTFOM}_7 = \frac{\Delta\text{MTTF}}{\text{KVAOF}} \qquad [\text{hr}] \tag{5.11}$$

Further, this this kVA factor can also be modified based on expected increased inductance from the machine and its associated power factor. Generally, FT machines with a power factor of 0.7 are expected to have a characteristic current of 1 per-unit. An important metric for the machine but certainly to the detriment of drive kVA sizing.

Both versions of this overrating FT-FoM, $FTFOM_6$, and $FTFOM_7$, can prove to be useful alternatives to the mass-based FT-FoM, $FTFOM_5$, in cases where the mass scaling relationships associated with modular topologies are poorly understood with large error bands, or cases where drive system cost is more important than mass.

It is recognized that power converter modules can be designed in some cases to deliver overload power values higher than their rated values for limited periods of time. In some applications, it may be possible to take advantage of these overload power capabilities during fault conditions. As a result, the steady-state power ratings of these modules can be reduced, thereby reducing the mass and penalty associated with the modular drive configuration. In fact, the value of KVAOF can be reduced to 1 if the modules all have sufficient short-term power overload capability so that no increase in the module steady-state kVA ratings is needed to handle the fault cases. This benefit will automatically be reflected in the value of $FTFOM_7$ since lower values of KVAOF result in higher values of this metric.

This discussion could lead to the over-simplified conclusion that designing FT drive topologies that take advantage of the overload power operation of drive modules during faults will always be superior to other candidate topologies that are designed using the more conservative approach based entirely on module steady-state power ratings. The tradeoffs between these two approaches are more complicated in reality because operating the modules in their overload mode increases their electrical and thermal stresses which, in turn, reduces the configuration's ΔMTTF value that appears in the numerator of these FT-FoM definitions. As a result, the increased level of machine drive stress associated with overload operation must be reflected in the MTTF calculation, a topic that is discussed in Section 5.4.5.

5.1.4 Proposed Fault Tolerance Figure of Merit Summary

A summary of the proposed FT-FoM metrics introduced in this section is provided in Table 5-1. Each metric provides a different insight into specific attributes of a candidate FT drive system topology from

TABLE 5-1.—SUMMARY OF PROPOSED FT FoMs

Metric Group	FT-FoM	Calculation	Measure
System Reliability Improvement	1	$MTTF/MTTF_{std}$	Measure of FT topology reliability normalized by MTTF of a baseline topology (often 2-level VSI)
	2	ΔMTTF/MTMF	Measure of topology reliability improvement normalized by MTTF of the module group (MTMF)
SPF and Repairability Characterization	3	MTTF/MTTSPF	Metric indicating the dominance level of the single point failure rate in determining FT topology reliability
	4	$MTTF_{HR}/MTTF_{NR}$	Measure of the influence level of the repair rate on the reliability of a FT drive topology
Performance Tradeoff Metrics	5	ΔMTTF/Δkg	Measure of FT drive topology reliability improvement gained per increment in topology mass
	6	ΔMTTF/F	Measure of FT drive topology reliability improvement in relation to the level of required module overrating
	7	ΔMTTF/KVAOF	Variant of $FTFOM_6$ that uses the combined steady-state kVA overrating of the modules for the normalization

5.2 Determining Mean Time to Failure (MTTF) Using Markov Chains

The performance metric that appears in the definitions of all of the FT-FoM metrics provided in Section 5.1 is the Mean Time to Failure (MTTF) of the candidate fault-tolerant motor drive system. For these FT-FoM metrics to be useful, it is critical to develop MTTF calculation methodologies that allow users to quickly make comparisons and draw conclusions about alternative FT motor drive topologies. This paper presents an evaluation methodology using Markov Chains and component failure rates, although other evaluation methods such as those described in References 26 and 27 can be used depending on the level of detail desired by the user. This section summarizes a methodology for evaluating the MTTF value for a candidate FT motor drive topology using Markov Chains.

Continuous-time Markov Chains break a system into multiple unique states dependent on the operating mode of the system (e.g., healthy, failed, faulted, aged, etc.). An individual state that is a member of an *n*-state system will have transitions entering and leaving the studied state as shown in Figure 5-2 and can be described by the following differential equation

$$\frac{dM_i}{dt} = \sum_{k=1,k\neq i}^{n} (\lambda_{m,ki} \cdot M_k - \lambda_{m,ik} \cdot M_i) \tag{5.12}$$

where M_i represents the probability of being in state-M_i at time t and $\lambda_{m,ik}$ representing the probability of a transition occurring from state-M_i to state-M_k. For reliability evaluation and calculation of MTTF, these transition probabilities are derived from failure rates of the underlying system components at the source state (e.g., transition $\lambda_{m,ik}$ represents the failure rate associated with operation in state-M_i shown in Figure 5-2, causing a transition into a different fault or failure state k).

These states can be assembled into a complete system diagram such as the generic FT system example in Figure 5-3 using a simplified notation following the FT categorization of states. At a minimum, FT systems are separated into three groups of states: healthy (state-H), faulted (state-M), and failed (state-F). Similar designations can be adopted for transition probabilities. Transitions from healthy-to-faulted, faulted-to-faulted, and faulted-to-failed states are referred as module failure rates ($\lambda_{m,k}$), from healthy-to-failed states as single point failure (SPF) rates ($\lambda_{s,k}$), and return transitions from faulted-to-healthy states as repair rates (μ). The failed state in Figure 5-3 is shown to be absorbing (no transitions from failed to healthy) to reflect applications where operation in a failed state leads to a catastrophic outcome.

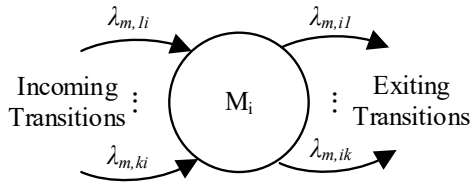

Figure 5-2.—Single Markov chain state with incoming and exiting transitions shown.

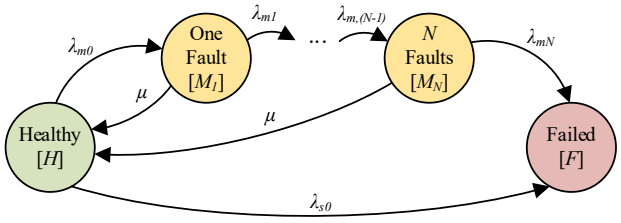

Figure 5-3.—Generic FT-system with simplified transition notation showing with healthy, faulted, and failed states shown.

Each state shown in Figure 5-3 has a defining state equation similar to Equation (5.12), which can be assembled into the $n \times n$ system

$$\begin{bmatrix} \dot{H} \\ \dot{M}_1 \\ \dot{M}_2 \\ \vdots \\ \dot{M}_{N-1} \\ \dot{M}_N \\ \dot{F} \end{bmatrix} = \begin{bmatrix} -\lambda_{m0} - \lambda_{s0} & \mu & \cdots & \mu & 0 \\ \lambda_{m0} & -\lambda_{m1} - \mu & \cdots & 0 & 0 \\ 0 & \lambda_{m1} & \cdots & 0 & 0 \\ \vdots & \vdots & \ddots & \vdots & 0 \\ 0 & 0 & \cdots & 0 & 0 \\ 0 & 0 & \cdots & -\lambda_{mN} - \mu & 0 \\ \lambda_{s0} & 0 & \cdots & \lambda_{mN} & 0 \end{bmatrix} \begin{bmatrix} H \\ M_1 \\ M_2 \\ \vdots \\ M_{N-1} \\ M_N \\ F \end{bmatrix} \tag{5.13}$$

which is in the general form and corresponding solution

$$\begin{aligned} \dot{x} &= Ax \\ x &= e^{At} x_0 \end{aligned} \tag{5.14}$$

with state probability vector x, transition probability matrix A, and x_0 represents the initial state of the system. Since the system is assumed healthy at the beginning of its life, the initial state is represented as $x_0 = [1, 0, \ldots, 0]^T$. State probabilities can be determined by calculating the matrix exponential in Equation (5.14) that is valuable for calculating the system MTTF according to

$$\text{MTTF} = \int_0^\infty (1 - F)dt = \int_0^\infty (H + \sum\nolimits_{i=1}^{N} M_i)dt \tag{5.15}$$

The process of determining the matrix exponential in Equation (5.14) to find the state probabilities and then evaluating (5.15) to determine the MTTF is cumbersome for large and complex systems. Alternatively, MTTF can more easily be determined by taking advantage of Laplace transform properties. The Laplace transform of Equation (5.14) is

$$X(s) = (sI - A)^{-1} x_0 \tag{5.16}$$

where I is the identity matrix. The MTTF of a system can be determined using the Final Value Theorem.

$$\begin{aligned} \text{MTTF} &= \lim_{s \to 0} \left[s \cdot \mathcal{L} \left\{ \int_0^t \left(H + \sum\nolimits_{i=1}^{N} M_i \right) dt \right\} \right] \\ &= \lim_{s \to 0} \left[s \cdot \frac{1}{s} \cdot \left(H(s) + \sum\nolimits_{i=1}^{N} M_i(s) \right) \right] \\ &= H(0) + \sum\nolimits_{i=1}^{N} M_i(0) \end{aligned} \tag{5.17}$$

Two critical observations can be made about Equation (5.17). First, Equation (5.17) clearly quantifies the non-failed state contributions to the overall reliability, or MTTF, of a FT system. This ability to segregate the added reliability hours per FT state can be beneficial to the user for determining whether the expected gain in reliability justifies the cost and complexity of adding another FT state.

A second critical observation from Equation (5.17) is that the determination of MTTF is independent of the failed state probability F allowing for the direct calculation of MTTF from the transition matrix and initial conditions. This is to be expected since a key assumption of the system diagram in Figure 5-3 is that the failed state is absorbing (i.e., no exiting transitions). This means that the final row and column of the A transition matrix can be eliminated leading to a reduced matrix A' with dimensions $(n\text{-}1)\times(n\text{-}1)$. Similarly, the initial conditions vector can be reduced to x_0' with the failed state row removed. The MTTF is directly determined from the matrix inverse of A' and modified initial conditions matrix x_0' by combining Equations (5.16) and (5.17)

$$\begin{aligned} X'(0) &= -\left[A'\right]^{-1} x_0' \\ \text{MTTF} &= \sum_{i=1}^{n-1} X'[i](0) \end{aligned} \tag{5.18}$$

The result in Equation (5.18) can be easily implemented in most coding environments allowing for simplified calculation of MTTF for any FT-system Markov Chain which is a key step in the evaluation of the proposed FT-FoMs presented in Section 5.1. A similar expression is presented in Reference 28, but Equation (5.18) is noteworthy because of its rigorous derivation based on Laplace transform theory.

5.2.1 Three-State Analytical MTTF Example

In some instances, it is desirable to produce analytical MTTF formulas for a given FT-system to better understand the relationship between the underlying failure transitions and component failure rates. This process is illustrated using the elementary FT-system state diagram in Figure 5-1(b) consisting of a single faulted state. These states are represented by a set of three differential equations.

$$\begin{aligned} \dot{H} &= \mu \cdot M_1 - (\lambda_{m0} + \lambda_{s0}) \cdot H \\ \dot{M}_1 &= \lambda_{m0} \cdot H - (\mu + \lambda_{m1}) \cdot M_1 \\ \dot{F} &= \lambda_{s0} \cdot H + \lambda_{m1} \cdot M_1 \end{aligned} \tag{5.19}$$

As mentioned above, the failed state probability F is not used in the MTTF derivation in Equation (5.17) and will be ignored moving forward since the failed state is absorbing, thus reducing the relevant number of equations to two. The corresponding Laplace-transformed versions of the first two equations in Equation (5.19) are

$$\begin{aligned} H(s) \cdot s - 1 &= \mu \cdot M_1(s) - (\lambda_{m0} + \lambda_{s0}) \cdot H(s) \\ M_1(s) \cdot s &= \lambda_{m0} \cdot H(s) - (\mu + \lambda_{m1}) \cdot M_1(s) \end{aligned} \tag{5.20}$$

which can be solved for both $H(s)$ and $M_1(s)$

$$\begin{aligned} H(s) &= \frac{(s + \mu + \lambda_{m1})}{(s + \mu + \lambda_{m1}) \cdot (s + \lambda_{m0} + \lambda_{s0}) - \lambda_{m0} \cdot \mu} \\ M_1(s) &= \frac{\lambda_{m0}}{(s + \mu + \lambda_{m1}) \cdot (s + \lambda_{m0} + \lambda_{s0}) - \lambda_{m0} \cdot \mu} \end{aligned} \tag{5.21}$$

As the final step, the FT-system MTTF is calculated by applying Equation (5.17):

$$\begin{aligned} \text{MTTF} &= H(0) + M_1(0) \\ &= \frac{\lambda_{m0} + \lambda_{m1} + \mu}{\lambda_{m0} \cdot \lambda_{m1} + \lambda_{s0} \cdot \mu + \lambda_{s0} \cdot \lambda_{m1}} \end{aligned} \tag{5.22}$$

matching the derived equation in Reference 29.

The derivation of analytical formulas for MTTF increase rapidly in complexity as the number of states and transitions grows. Powerful software tools like MAPLE can be used to assist with the extraction of analytical expressions for MTTF in these more complicated cases. Critical to the calculation of MTTF is the underlying component failure data and the subsequent determination of the failure rates for all the fault and failure state transitions. These items are discussed in upcoming sections.

5.3 Procedure for Use of FT-FoMs

A recommended four-step procedure for evaluating the FT-FoMs defined in Section 5.1 is summarized in Figure 5-4 and described in this section. The purpose of this procedure is to assist users with the task of developing Markov Chain models for candidate FT-systems, including the determination of faulted states and transition values. The developed state model can then be used to estimate the MTTF of the FT-system which is critical to evaluating the FT-FoMs.

5.3.1 Step 1: Define FT System and Components

The first step in the Figure 5-4 procedure is the definition of the FT-system and its components. More specifically, this process involves identifying all relevant components in the FT-system (e.g., switches, capacitors, machine windings, etc.), the associated fault modes and their interactions, the impact of repairing any faults, and the ultimate system failure mode. In addition, the user must define the desired system operating capabilities during each of the fault and failure modes.

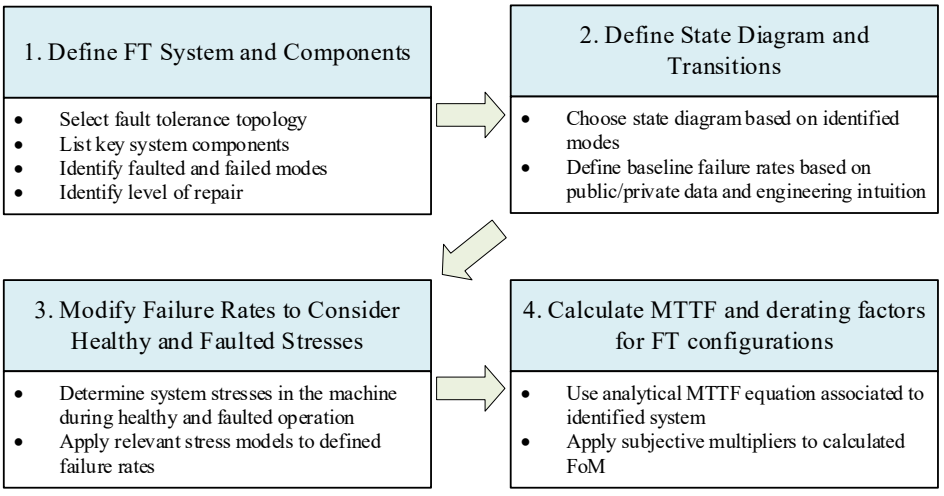

Figure 5-4.—Recommended procedure for the evaluation of FT-FoMs for candidate FT-systems.

5.3.2 Step 2: Define State Diagram and Transitions

The next step in the procedure is to organize the fault and failure modes identified in Step 1 into healthy, faulted, and failed states based on their effects leading to development of a state diagram. In FT-systems, simplifications are typically made when modeling a single module that any component failure inside the module results in the same fault state which, typically, is inoperability of the module. If there are *n* identical modules in the system with the same fault state, the fault modes for these *n* modules can be grouped together into a single equivalent fault state with a combined module failure rate that is *n* times that of a single module.

Transitions between states is initiated by component failures and other failure events (e.g., damage from foreign objects), each of which is quantified by its associated failure rate. In many cases, the fault states are associated with several different component failures and other failure events. When this is the case, the overall fault transition probability λ is determined by forming the sum of the failure rates. Typical values of component failure rate can be secured from either user internal sources, component data sheets, or from the published literature. Sample data for the modular machine study can be found in Reference 4. A FT-system state diagram will almost always also have two additional important transition paths for single point failures (λ_{s0}) and repair transitions (μ). The effects of both of these variables is discussed in the modular machine study in Reference 4.

5.3.3 Step 3: Modify Failure Rates to Consider Operating Stresses

The Step 2 failure transition values can be modified to reflect expected operating stresses during both healthy and faulted operation. In many cases it may be challenging to make significant modifications if this procedure is being used early in a FT topology screening process and specific design details of the studied FT topologies are unknown. However, parametric studies exploring the impact of post-fault stress on the FT-system reliability are still possible and valuable in some cases.

Some basic pre- and post-fault stress details can be determined by understanding the FT topology itself and how the system reconfigures itself after a failure. In this procedure, the operating stress factors will be selected based on the concept of pi-factors suggested in MIL-HDBK-217F (Ref. 30) where a baseline component failure rate λ_{BL} is modified by multisource stress factors π_i, leading to an overall stressed failure rate of λ_{STR}

$$\lambda_{STR} = \prod_{i=1} (\pi_i) \cdot \lambda_{BL} \tag{5.23}$$

In general, it is recommended that users apply physical principles underlying component life-calculation formulas or by looking at datasheets of module components. Using this approach, the pi-factors can be extracted by ratioing life-estimation results

$$\pi_i = \frac{\lambda_{STR,i}}{\lambda_{BL}} = \frac{L_{BL}}{L_{STR,i}} \tag{5.24}$$

where L_{BL} represents the baseline life under healthy operating conditions and $L_{STR,i}$ refers to stressed-state life operating under stressed condition *i*. Formulas for component lifetimes and pi-factors for typical electric machine components together can be found in the modular machine study report cited above.

5.3.4 Step 4: Calculate MTTF and Derating Factors for FT Configurations

A fully assembled Markov chain state diagram of the studied FT-system with numerically determined failure transitions should be assembled before initiating this step, with equations in a form matching those in Section 5.1.

These techniques for calculating the value of MTTF set the stage for evaluating the FT-FoMs $FTFOM_1$ to $FTFOM_4$ described in Section 5.1 and summarized in Table 5-1. $FTFOM_6$ and $FTFOM_7$ require determination of the overrating factors F and KVAOF defined in Reference 4 and Equation (5.10), respectively. The remaining FT-FoM, $FTFOM_5$, requires calculation of the added mass required for implementing the studied FT system topology compared to the baseline topology without fault tolerance features:

$$\Delta\text{kg} = m_{\text{FT}} - m_{\text{BL}} \tag{5.25}$$

where Δkg is the difference in masses, m_{BL} is the mass of the baseline system, and m_{FT} is the mass of the FT system topology that is being investigated. The determination of Equation (5.25) is likely impractical at an early design stage when the objective is to compare multiple FT topology concepts. However, it may be possible to estimate the mass of a candidate FT topology using available reference designs with comparable power and voltage ratings. The reference motor design mass m_{ref} must first be divided into the power electronics and machine mass contributions as shown in

$$m_{\text{ref}} = m_{\text{em}} + m_{\text{pe}} \tag{5.26}$$

where m_{em} is the machine mass and m_{pe} is the power electronics mass. Mass scaling factors for the FT system can be estimated from derating factors or component part counts leading to

$$\Delta\text{kg} = \text{MMF} \cdot m_{\text{em}} + \text{DMF} \cdot m_{\text{pe}} - m_{\text{ref}} \tag{5.27}$$

where MMF is the machine-mass scaling factor and DMF is the power electronics drive-mass scaling factor. The estimation of these FT mass scaling factors can take a wide variety of approaches. For the example FT topologies used as examples in Section 5.4, the value MMF is proportional to the overrating factor F (Section 5.4.3) and DMF is proportional to the ratio of the power electronics drive component counts in the candidate FT topology and the baseline configuration, shown as

$$\begin{aligned} \text{MMF} &= k_{\text{MMF}} \cdot F \\ \text{DMF} &= k_{\text{DMF}} \cdot n_{\text{pe,FT}} \,/\, n_{\text{pe,ref}} \end{aligned} \tag{5.28}$$

where the power electronics component count ratio is $n_{\text{pe,FT}} / n_{\text{pe,ref}}$, and the k_{MMF} and k_{DMF} are user-selected tuning factors for the machine and power electronics equations, respectively. Despite the obvious limitations of this approach, it provides a suggested starting point for the user to estimate the candidate FT topology mass penalty Δkg that is needed to evaluate $FTFOM_5$.

5.4 FT-FoM Case Study

This section demonstrates the evaluation of the proposed FT-FoMs presented in the preceding sections and the types of insights that can be gained from this exercise. Four topologies are considered that include the five-phase motor drive shown in Figure 5-5(a) and a direct redundant topology shown in Figure 5-5(b). In addition, a two-module MMD and a four-module MMD are included which were described during

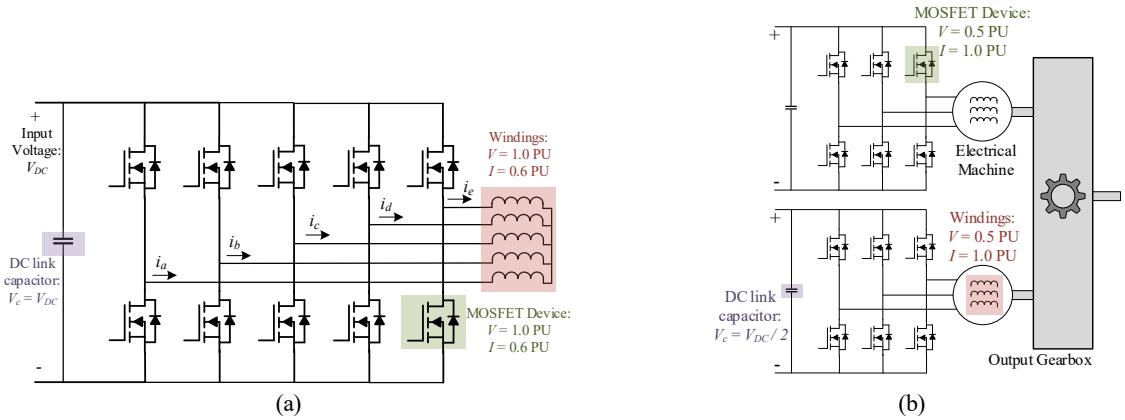

Figure 5-5.—Case study topologies not yet presented: (a) five phase FT topology with component ratings under healthy conditions; and (b) direct motor drive redundant topology with component ratings under healthy conditions.

the quadcopter machine reliability evaluation above. A fifth variant topology is added that consists of a modified four-module system that moves two of the significant single-point-failure (SPF) components (resolver and cooling system) into the module paths by making them redundant, leaving only bearings in the SPF failure path. In addition, the failure rates of all of the SPF components identified in Reference 4 are reduced by a factor of 17 for all five topologies, reflecting aspirational improvements of their reliability that result in more meaningful comparisons of the topologies. Application of the FT FoM evaluation steps presented in Figure 5-4 are briefly addressed in the following discussion.

5.4.1 Definition of FT Topologies and Components

As noted above, four basic FT topologies are compared in this study: 1) five-phase machine drive with two allowable switch failures; 2) direct redundant motor drive; 3) two-module MMD; and 4) four-module MMD. A two-level VSI has been selected for the baseline topology. The basic VSI topology consists of MOSFET devices with anti-parallel diodes (x6), a single dc-link capacitor (x1), and a three-phase machine winding set (x1). Other components include machine bearings pair (x1), coolant system (x1), current sensors (x3), gate drivers (x6), controller (x1), and rotor angular position resolver (x1). Other components (rotor structure, magnets, etc.) are assumed to have much lower failure modes compared to the preceding identified components and are ignored in this evaluation.

The five-phase VSI enables drive reconfiguration by adding phase legs to the baseline concept that provide phase redundancy for open-circuit faults as shown in Figure 5-5(a). In the event of a switch or winding open-circuit fault, the faulted phase leg is isolated by opening the corresponding complementary switch. The remaining healthy phases are then able to continue operating, perhaps with some phase angle changes in their excitation, to retain a large fraction of the healthy drive's original output power capability. In this study, the five-phase VSI assumes that two open-circuit phase-leg faults can be tolerated before a failure.

The second FT topology is the simplest, applying redundancy directly to the baseline three-phase motor drive system (i.e., direct redundant) by adopting a dual motor drive redundant topology. These two redundant motor drives are coupled together mechanically using a gearbox as shown in Figure 5-5(b). In the event of a motor drive failure, the failed unit is decoupled from the gearbox, and operation continues using the remaining healthy motor drive.

It is also assumed that each of the two drives in the two-module topology is excited using a DC link voltage that is 50 percent of the value used for the baseline topology, lowering the voltage rating of all of the inverter switches while their current rating is unchanged. If one of the two modules fails, the remaining

healthy module must deliver approx. twice the current it supplies during normal healthy operation in order to return the topology to its full power capability. This increases the electrical and thermal stress on the healthy power switches that must be reflected in the stress factors for the inverter switches.

The final two FT topologies each takes the form of a modular motor drive (MMD) where redundancy is implemented at both the power electronics and machine windings level. This is accomplished by dividing the single stator assembly into multiple three-phase winding sets, each supplied by its own independent power electronics and control as described in the quadcopter machine reliability study. For the first of these two topologies, there are two modules that each delivers half of the rated power during healthy operation, similar to the direct redundant topology. Each module is assumed to operate with Vdc/2 and the same rated current as the baseline VSI topology (Vdc/4 for the four-module case). It is important to note that the two-module MMD configuration is only capable of continuing operation following a single module fault. In comparison, the four-module MMD configuration is capable of continued operation following two module faults.

As noted in the introduction of this subsection, a fifth topology is included in the study that is almost identical to the four-module topology described above except that the total single-point failure rate is significantly reduced by adding modular redundancy for the resolver and the cooling system, thereby removing them from the SPF path. In addition, the values of the failure rates for the SPF components in Reference 4 have been reduced substantially by a factor of 17 for all of the considered topologies in order to prevent the single-point failure rate from dominating the FT-FoM values and thereby interfering with the objective of highlighting the key fault tolerance differences among the 5 topologies.

A summary of the studied FT topologies and fault coverage capability for each of the five studied topologies is provided in in Table 5-2.

TABLE 5-2.—STUDIED FT TOPOLOGIES AND FAULT COVERAGE CAPABILITY

Topology	PE Failure Protection (x – yes, o – no)			Machine Failure Protection (x – yes, o – no)			Non-Power Electronics or Machine Failure Protections and Vulnerabilities	
	Switch Short Ckt.	Switch Open Ckt.	Cap.	Term. Ph. Open	Term. Ph. Short	Internal Short	Redundant Comp.	Single Pt. Failures
Baseline (two-level VSI)	O	O	O	O	O	O	----------	Controller, resolver, current sensors, bearings, cooling system
Five-Phase VSI	O	X	O	X	O	O	----------	Controller, resolver, current sensors, bearings, cooling system
Direct Redundancy	X	X	X	X	X	X	Controller, resolver, current sensors, bearings	Gearbox, cooling system
2-Module Independent MMD	X	X	X	X	X	X	Controller, current sensors	Resolver, bearings, cooling system
4-Module Independent MMD	X	X	X	X	X	X	Controller, current sensors	Resolver, bearings cooling system
4-Module Independent MMD with reduced SPF	X	X	X	X	X	X	Controller, current sensors, resolver, cooling system	Bearings

5.4.2 Developing Markov Chain Models

A detailed discussion of the development of the Markov chains models is provided in Reference 4. Summarizing, fault-states are added to the state-space diagram based on their failure mode effects. Transitions between states corresponds to relevant failure rates that initiate changes between states. Technique for assembling transfer matrices and developing analytical equations for calculating MTTF are outlined in Section 5.2.

5.4.3 Baseline Failure Rates and Modifications for Impact of Operating Stresses

Baseline failure rates for evaluating the MTTF values of the shared FT topologies are summarized in Reference 4. Readers are reminded that the failure rates for all of the single-point failure components are reduced by a factor of 17 for all five topologies when calculating the FoM values. For the direct redundant configuration, the failure rate of the gearbox, one of the major single point failure sources in this topology, is assumed to be equal to the bearing failure rate.

The same failure rates are applied to each topology in its healthy state in order to provide meaningful comparisons of the reliability characteristics for these topologies. However, the topologies operate with varying levels of post-fault stress that will be represented by π stress factors defined previously by (5.24). The calculated stress factors for this analysis are summarized in Table 5-3 with corresponding justifications addressed briefly in the following paragraphs.

Post-fault stresses are heightened in all topologies because they are assumed to deliver full power output after a fault for this case study. The post-fault healthy module phase current must increase in proportion to the machine overrating factor F defined in Reference 4, and the corresponding winding losses scale as F^2. For purposes of this analysis, it is assumed that the machine and power electronics thermal system experience post-fault temperature rises proportional to F^2.

Similar simplifications are made to consider the impact of unbalanced magnetic pull (UMP) on the rotor after the loss of a module (i.e., increased dynamic load on the bearing) which worsens as the number of faulted modules increases. For this analysis, it is assumed that the increase in bearing dynamic load ratio (C/P) is proportional to the machine overrating factor F. In some instances, the loss of a subsequent phases or modules could reduce or completely cancel the unbalanced pull on the rotor (e.g., opposite modules). However, the possibility of unbalanced force cancellation will be ignored during this case study.

The direct redundant and modular configurations are defined to be connected in series resulting in higher module voltages after a fault. Machine winding voltage stress factors are estimated using the insulation life-time relationships. Capacitor and device voltage stresses are assumed to use relationships presented in component datasheets. Voltage ratings of healthy device and winding insulation are assumed to be overrated to 200 percent of the component nominal operating voltages to allow for more reasonable voltage stress ratio values.

5.4.4 Repair Rate

For all of the MTTF and FT-FoM calculations, it is assumed that machine failures will be repaired within 24 operating hours on average, corresponding to a repair rate of $\mu = 1/24 = 0.0417$ hrs^{-1}. As noted earlier, it is assumed that the system retains its ability to deliver its rated steady-state power until the system failure event occurs. The alternative of allowing for partial degradation of the system steady-state power delivery following a module fault is not considered here in order to avoid the additional complications it would introduce.

A single dc input supply value is assumed for all of the candidate FT topologies. For topologies with multiple dc inputs, it is assumed these inputs are connected in series. In the event of a module fault, it is

TABLE 5-3.—DEVELOPED STRESS FACTORS FOR CASE STUDY

Topology	Component	Post-Fault Stressor (π-factor)	π-Factor Quantity	Notes
Five-Phase Design	Winding (M_1 state)	Temp. ($\pi_{cls,T,1}$)	3.0	Stresses related to first faulted state
	Device (M_1 state)	Temp. ($\pi_{sw,T,1}$)	2.5	
	Winding (M_2 state)	Temp. ($\pi_{cls,T,2}$)	6.7	Stresses related to second faulted state
	Device (M_2 state)	Temp. ($\pi_{sw,T,2}$)	5.1	
Direct Redundant	Winding	Temp. ($\pi_{cls,T}$)	16.0	
	Winding	Voltage ($\pi_{cls,V}$)	32.0	
	Capacitor	Voltage ($\pi_{cap,V}$)	41.3	
	Device	Temp. ($\pi_{sw,T}$)	10.4	
	Device	Voltage ($\pi_{sw,V}$)	403.0	
2-Module MMD	Winding	Temp. ($\pi_{cls,T}$)	16.0	
	Winding	Voltage ($\pi_{cls,V}$)	32.0	
	Capacitor	Voltage ($\pi_{cap,V}$)	41.3	
	Device	Temp. ($\pi_{sw,T}$)	10.4	
	Device	Voltage ($\pi_{sw,V}$)	403.0	
	Bearing	UMP (π_{brg})	8.0	
4-Module MMD	Winding (M_1 state)	Temp. ($\pi_{cls,T,1}$)	3.4	Stresses related to first faulted state
	Winding (M_1 state)	Voltage ($\pi_{cls,V,1}$)	3.2	
	Capacitor (M_1 state)	Voltage ($\pi_{cap,V,1}$)	3.5	
	Device (M_1 state)	Temp. ($\pi_{sw,T,1}$)	2.8	
	Device (M_1 state)	Voltage ($\pi_{sw,V,1}$)	7.4	
	Bearing (M_1 state)	UMP ($\pi_{brg,1}$)	2.4	
	Winding (M_2 state)	Temp. ($\pi_{cls,T,1}$)	16.0	Stresses related to second faulted state
	Winding (M_2 state)	Voltage ($\pi_{cls,V,2}$)	32.0	
	Capacitor (M_2 state)	Voltage ($\pi_{cap,V,2}$)	41.3	
	Device (M_2 state)	Temp. ($\pi_{sw,T,2}$)	10.4	
	Device (M_2 state)	Voltage ($\pi_{sw,V,2}$)	403.0	
	Bearing (M_2 state)	UMP ($\pi_{brg,2}$)	8.0	

assumed the faulted module is bypassed by a short circuit across its dc input terminals, resulting in the total supply voltage being applied to the remaining series-connected healthy modules.

5.4.5 Calculation of MTTF and Derating Factors for FT Configurations

Module component failure rates defined in Reference 4 are multiplied by the corresponding π stress factors presented in Table 5-3 to establish their post-fault failure rates. Next, the MTTF values are evaluated for the five topologies. $FTFOM_1$, $FTFOM_2$, and $FTFOM_3$ can be directly determined from these MTTF values and previously calculated transitions. $FTFOM_4$ is evaluated by making the drive system MTTF calculation using repair transition rates of $\mu = 0.99$ hrs^{-1} (highly frequent repairs, corresponding to repairs every 1.01 hours of operation, representing a limiting case) and $\mu = 0.0$ hrs^{-1} (no repairs).

Derating factors *F* and KVAOF have been calculated for each topology using the provided formulas and the established component ratings. These derating factors are used to calculate $FTFOM_6$ and $FTFOM_7$. A summary of performance derating factors is provided in Table 5-4. Note that the KVAOF metrics reflect the 50 percent voltage derating for topologies capable of full output torque after one fault for the direct-redundant and two-module topology, and after two faults for the four-module topologies, as discussed.

TABLE 5-4.—SUMMARY OF DERATING FACTORS AND MASS MULTIPLIER FACTORS FOR FT-FoMs 5, 6, AND 7

Topology	Derating Factors		Mass Multipliers		Notes
	F	KVAOF	MMF	DMF	
Five-Phase	1.25	1	1.25	1.59	Added devices: 4-devices, 4-gate drives, 2-current sensors
Direct-Redundant	2	2	4	2	Added devices: 6-devices, 6-gate drives, 3 current sensors, 1-controller, 1-capacitor Subjective multiplier of 2 applied to MMF to reflect gearbox mass, multiple housings, cooling loops, etc.
Two MMD	2	2	2	2	Added devices: 6-devices, 6-gate drives, 3-current sensors, 1-controller, 1-capacitor
Four MMD	1.33	2	1.33	4	Added devices: 18-devices, 18-gate drives, 9-current sensors, 3- controllers, 3-capacitors

$FTFOM_7$ requires the estimation of mass differences between the studied FT topology and baseline configuration using Equations (5.25) to (5.28). The machine described in Section 2.0 is used as a reference with an estimated power electronics mass m_{pe} = 6 kg and machine mass m_{em} = 14 kg. Resulting topology-specific mass multiplying factors MMF and DMF are included in Table 5-4.

5.4.6 Evaluation and Interpretation of FT-FoM Values for Fault-Tolerant Topologies

Case study FT-FoM metric values have been calculated using the failure rates, stress factors, derating factors, and mass multiplier values described in the preceding subsection. For this discussion, only four of the seven metrics (FT-FoMs 1, 3, 4, and 5) are plotted in Figure 5-6. A complete set of calculated FT-FoMs are summarized in Table 5-5.

The bar charts for these four FT-FoM values exhibit some notable differences between the topologies that are helpful for highlighting their individual strengths and limitations. Some of the differences between the topologies that become visible in these FT-FoM bar charts will be discussed here.

1. The five-phase topology exhibits the worst FoM metrics, particularly for $FTFOM_1$, due to its insufficient fault coverage to realize significant MTTF benefit for the motor drive system.
2. The direct redundant topology achieves a significant MTTF improvement as observed in $FTFOM_1$ due to its improved fault mode coverage compared to the five-phase topology, which can be further improved with higher repair rates since it is the least saturated among the five topologies by the SPF rate as indicated in $FTFOM_3$. However, it is disadvantaged by a mass penalty compared to the three modular machine topologies that is reflected in is lower value of $FTFOM_5$.
3. Comparing the 2- and 4-module MMD topologies without the enhanced SPF rate, the 4-module MMD topology achieves significantly higher values of both $FTFOM_1$ and $FTFOM_5$, highlighting its advantages in terms of higher drive system MTTF and reduced mass penalty. This suggests the desirability of increasing then number of modules in the MMD topology to values higher than 2.
4. The fact that the value of $FTFOM_3$ for the 4-module topology without the enhanced SPF rate is 1.0 indicates that the single-point failure rate is limiting its ability to achieve still higher values of drive system MTTF. This is confirmed by the dramatic increase in the $FTFOM_1$, $FTFOM_4$, and $FTFOM_5$ values that results from reducing the SPF rate for the 4-module topology.

Taken together, the results of this FT-FoM case study reinforce previous observations in Reference 4 about the most promising approach to overcoming the daunting motor drive reliability gap in aerospace applications. More specifically, these FT-FoM values support the conclusion that the path to achieving the highest possible drive system reliability consists of maximizing the repair rate (i.e., fast response to

failures), and suppressing all single point failures using the most-effective available techniques including health monitoring, redundancy, etc. The results also suggest that increasing the module count in modular drives to a value higher than two is desirable for reducing the over-rating factors and associated mass penalty.

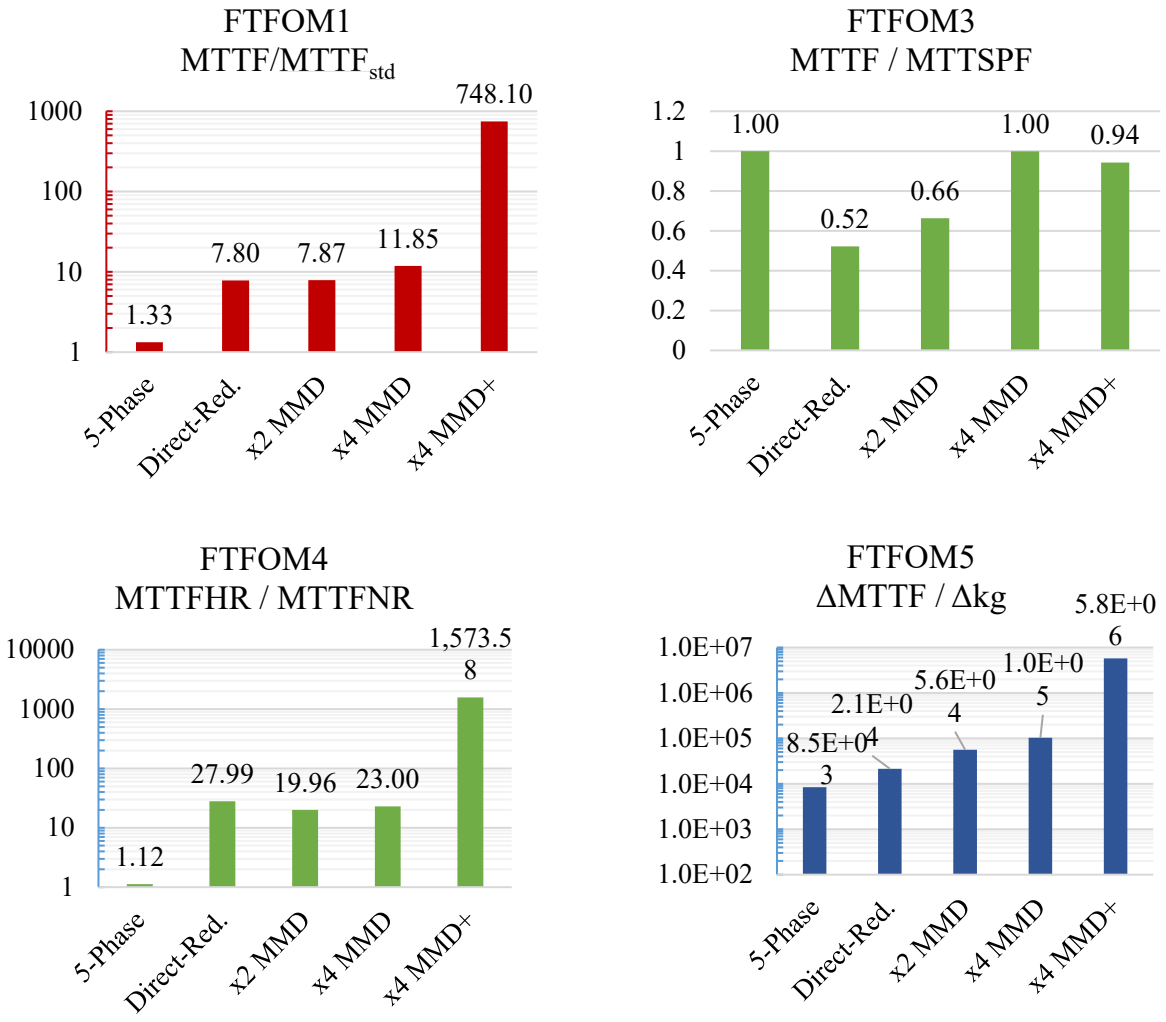

Figure 5-6.—FT-FoM case study results for five-phase (5-Phase), direct redundancy through a gearbox (Direct-Red), two-module MMD (x2 MMD), four-module MMD (x4 MMD), and four-module MMD with reduced single-point failures (x4 MMD+).

TABLE 5-5.—SUMMARY OF CASE STUDY FoM RESULTS

FT-FoM		5-Phase	Direct-Red.	x2 MMD	x4 MMD	x4 MMD+
1	MTTF/MTTF$_{std}$	1.33	7.80	7.87	11.85	748.10
2	ΔMTTF/MTMF	0.13	6.45	5.67	7.29	541.50
3	MTTF/MTTSPF	1.00	0.52	0.66	1.00	0.94
4	MTTF$_{HR}$/MTTF$_{NR}$	1.12	27.99	19.96	23.00	1573.58
5	ΔMTTF/Δkg	8.5E+03	2.1E+04	5.6E+04	1.0E+05	5.8E+06
6	ΔMTTF/F	4.3E+04	5.6E+05	5.6E+05	1.3E+06	9.2E+07
7	ΔMTTF/KVAOF	5.4E+04	5.6E+05	5.6E+05	8.9E+05	6.1E+07

5.5 Summary

This section is dedicated to the development and demonstration of newly created Fault Tolerance Figures of Merit (FT-FoMs). These FoMs provides new quantitative metrics for comparing different FT topologies by highlighting the level of predicted system reliability improvement and the degree to which this improvement is offset by penalties in other drive system performance metrics such as drive system mass or the required component power ratings. The seven FT-FoMs that are defined fall into three classes: (1) relative system reliability improvement compared to the reliability of the baseline topology or single module; (2) dependence of reliability improvement on key variables such as repair rate and single point failure rate; and (3) relative reliability improvement achieved by a FT configuration offset by its mass and cost penalties. Since the calculation of configuration's MTTF is essential to these metrics, analytical formulas for the MTTF have been developed and presented that enable faster evaluation. Step-by-step instructions are presented for evaluating the FT-FoMs.

A case study that applies the FT-FoMs to five FT motor drive topologies has been presented to explore the reliability differences between these topologies and to investigate the usefulness of the FT-FoMs for making these comparisons. Among the five candidates, the FT modular motor drive topology with four modules and a low single-point failure rate achieved significantly higher predicted reliability levels than the other four topologies. This comparison achieved its objectives of confirming the appealing fault tolerance potential of modular motor drives with more than two modules, as well as highlighting the critical importance of maximizing the repair rate while minimizing the single-point failure rate to achieve the largest reliability improvement.

6.0 Study Summary and Conclusions

Low reliability motor drives have been identified as a potential source of catastrophic failures in future electrified propulsion applications. The use of fault tolerance (FT) features is proposed as a promising approach to decouple motor drive reliability from the aircraft catastrophic failure rate. A preceding report on the earlier stages of this work provided a detailed design and analysis of a 70 kW modular motor drive (MMD) for a six-passenger quadrotor propulsor application. Specifically, the developed design uses four sets of redundant three-phase windings and power electronics, each independent from all of the others. The developed system utilizes enhanced electromagnetic isolation features including flux barriers and asymmetric tooth tips, as well as in-slot cooling to thermally isolate each module. In addition, results of a Markov chain reliability analysis showed that the combination of modularity, high repair rates, and a focus on eliminating single point failures (SPF) provides a promising path for closing the identified reliability gap.

This report is an extension of the initial quadcopter design and reliability analysis. The developed quadrotor FT modular machine-drive has been studied further to consider rotor demagnetization, turn-to-turn faults, and switch failure modes. Opportunities for alternative FT-MMD implementations have been investigated including current source inverters (CSIs) that exhibit desirable FT responses to short-circuit faults.

The developed quadcopter machine's back-iron flux barriers and modified tooth tip features have been evaluated in FT machine designs rated at 2 MW and 7 kW power levels to assess the scalability of these features. For both of these widely differing power ratings, the flux barrier and tooth tip design features have been shown to be effective for electromagnetically isolating the machine phases. However, the scalability of the in-slot cooling was shown to be ineffective at higher power levels due to basic well-known constraints imposed by geometric scaling laws. In contrast, the proposed in-slot cooling technique has been shown to scale well downward to lower power levels, effectively cooling and thermally isolating the machine phases

as desired. A 7 kW demonstrator machine has been fabricated and successfully tested, confirming the developed models and the effectiveness of the electromagnetic and thermal isolation features.

In the later stages of this study, the viewpoint was broadened to consider alternative FT machine-drive topologies beyond MMDs by developing generalized FT figures of merit (FoMs). In total, seven FoM metrics have been proposed that capture the benefits of Mean Time to Failure (MTTF) improvements contributed by FT features offset by any of the known penalties (weight, etc.) associated with FT-MMD configurations. These FT FoMs have been applied to a streamlined case study in order to illustrate their usefulness for developing quantitative comparisons among candidate FT topologies. The results of the case study highlight the strengths and tradeoffs associated with alternative MMD configurations as a means of improving system reliability.

6.1 Summary of Key Study Results and Observations

The principal study results and observations are summarized below:

Fault-Tolerant Electric Machine

- A review of the developed quadrotor integrated MMD architecture design has been provided. The combination of a fractional-slot, concentrated winding (FSCW) stator and surface permanent magnet rotor utilizing a Halbach magnet array is capable of achieving the desired power density and performance. In-slot cooling using a 3D-printed ceramic bobbin wrapped around each tooth is effective for reducing the winding's thermal resistance to the cooling fluid.
- Specialized electromagnetic isolation features consisting of modified tooth-tips and stator back-iron cavities have been successfully applied to a stator with double-layer windings in the SPP = 2/7 family to achieve high levels of electromagnetic isolation comparable to a single-layer winding design. The 3D-printed bobbin-based in-slot cooling technique has also been applied to this design to achieve high levels of thermal isolation between phases and modules.
- The developed machine has been evaluated analytically under open- and short-circuit terminal fault conditions. The model shows that this FT-MMD configuration is capable of maintaining rated shaft output torque following these faults with minimal rotor demagnetization at the price of reduced thermal margins.
- Internal short circuits (turn-to-turn faults) have also been studied for the developed model. Analytical short-circuit current calculation methods are presented that exhibit good agreement with the results of finite element models.
- The intensity of internal short-circuit losses resulting from turn-to-turn faults requires fast action to suppress the fault effects via three-phase short circuits intentionally applied to the faulted module. The internal short-circuit model makes it possible to estimate fault-related losses that are used as inputs to a transient thermal model. The transient thermal module shows that adjacent phases are unaffected by the internal short-circuit failure for short time periods (i.e., transient thermal isolation), providing valuable time for the control system to detect and respond to the failure.
- Module power electronics switch failures have also been analyzed along with the appropriate fault-mode response. The baseline voltage source inverter (VSI) has been studied under both open-circuit (OC) and short-circuit (SC) switch failure conditions. OC faults are shown to be benign for the VSI, while SC faults are much more dangerous and difficult to manage, exhibiting significant transient currents that can be damaging to the MMD inverter and machine.
- These predicted VSI switch failure results have been compared with the corresponding fault response using a current source inverter (CSI), showing that the CSI has significantly better SC

transient fault response compared to the VSI with appropriately sized passive components. More specifically, the CSI is capable of suppressing all of the phase currents in the faulted module following a fault, protecting both the healthy switches and the machine from damage.

Isolation Features Scaling

- The 70 kW MMD has been scaled to a four-module 2 MW power level to assess MMD feature scalability. The 2 MW MMD design has been analyzed using the same technique applied to the 70 kW MMD design, showing that the MMD architecture can achieve power-density levels necessary for megawatt-scale propulsion applications.
- The same electromagnetic isolation techniques used successfully in the 70 kW MMD design consisting of proper choice of slot-pole combination, asymmetric tooth-tips, and back-iron cavities are shown to be effective for electromagnetically isolating the 2 MW machine phases and modules.
- However, the use of a ceramic in-slot cooling bobbins was shown to be ineffective for cooling the developed 2 MW design utilizing materials similar to those used in the 70 kW quadrotor MMD design. This poor result is attributed to a combination of factors including the well-known adverse effects of geometric scaling laws for larger machines, as well as higher loss densities resulting from the higher power density requirements associated with megawatt-scale propulsion machines.
- Analysis showed that the in-slot cooling approach would be feasible for use in megawatt-scale machines if the thermal conductivity of encapsulant materials could be sufficiently improved. However, encapsulant materials with these enhanced characteristics are not currently available.
- The 70 kW MMD design was also scaled down in power rating by a factor of ten to a 7 kW machine design. This design was modified to use fewer modules (i.e., 2 instead of 4) to make it more compatible with the smaller dimensions. Furthermore, some machine geometry features were simplified, and the in-slot cooling approach was modified to use thermally-conductive ceramic tubes instead of the 3D-printed bobbins used in the 70 kW machine design.
- The thermal isolation characteristics of the mid-slot ceramic tubes were analyzed to evaluate the impact of alternative series/parallel interconnections of the coolant channels in order to understand their performance tradeoffs. A fully-parallel coolant connection scheme for the stator in-slot tubes was selected to minimize the tube size as well the risks from thermal interactions caused by temperature gradients in series-connected tubes.
- Analysis of the developed 7 kW machine design showed that it meets the desired performance criteria and effectively isolates the machine modules both electromagnetically and thermally, confirming the scalability of the developed FT features to low power ratings.
- Electromagnetic analysis of the asymmetric tooth-tips confirmed the usefulness of the inner-most tooth tips, showing that they contribute >10 percent of the overall machine phase inductance.

Experimental Confirmation Testing of FT MMD

- The low-power 7 kW MMD design was fabricated as a demonstrator unit to confirm the isolation features and the performance characteristics. All key details related to the machine design and fabrication have been provided. The machine was entirely built from readily-available materials and 3D-printed components that were fabricated using in-house University of Wisconsin lab facilities.
- The measured electrical parameters (i.e., resistance, inductance, magnet flux linkage, and characteristic current) of the demonstrator machine align well with the predicted values derived from the developed machine models.

- The magnetic isolation ratio (MIR) of the demonstrator machine was assessed by locking the rotor and applying high-frequency current to a single module, and observing the terminal voltage in the unexcited module. The measured MIR was determined to be 3.3 percent compared to the model-predicted value of 1.7 percent. The higher measured value is attributed to the model calculation utilizing "air" magnets. When the magnet saturation characteristics are incorporated, the magnetic isolation calculations align. Despite this difference, the measured MIR value of 3.3 percent is excellent, demonstrating highly effective magnetic isolation between phase windings.
- All measured torque values were within 3 percent of model predictions for the rated operating space. Similarly, the thermal models track well with experimental results, although the measured temperatures were modestly higher than the predictions.
- Open- and short-circuit terminal faults were applied to one of the modules in the demonstrator machine. These experiments confirmed that the developed FT-MMD unit can sustain a terminal fault and respond appropriately with increased current in the healthy module to restore the desired torque output.
- Effective thermal isolation was validated experimentally during the terminal fault testing. The results confirm that the healthy phases and modules are unaffected by faulted modules.
- Split windings were installed in one module of the demonstrator unit, allowing controllable turn-to-turn faults to be applied. The fault current levels were measured at low speed with varying fault resistance values in order to minimize the risk of winding damage or magnet demagnetization.
- Turn-to-turn faults were applied during low-speed operation, and the impact of intentionally applying a 3-phase short circuit to the faulted module was tested, demonstrating that it is a promising technique for suppressing the fault current in the turn-to-turn short-circuit path.
- Transient thermal isolation was also demonstrated during this testing of turn-to-turn short-circuit faults, highlighting its effectiveness for protecting the adjacent winding that shares the same slot.

FT Figures of Merit (FoMs)

- A set of FT-FoMs has been developed for comparing FT topologies by quantifying their system reliability benefits offset by the performance penalties in other categories such as weight. These FT-FoMs include:
  - FoMs quantifying the relative MTTF benefit against a standard baseline (FT-FOM 1 and 2).
  - FoMs quantifying the candidate topology dependency on key variables including the repair rate and single-point failure rate ((FT-FOM 3 and 4).
  - FoMs quantifying the MTTF improvement of candidate topologies offset by penalties in weight and component overratings ((FT-FOM 5, 6, and 7).
- The evaluation of the candidate topology's MTTF using Markov chains is required for all seven of the FT-FOMs. Mathematical formulas were derived that make it possible for users to quickly calculate MTTF values for Markov chain state diagrams.
- A procedure has been proposed for the proper use of these FT-FOMs. This procedure is applied to a case study comparing different types of FT motor drive topologies. The case study results confirm that the FT-FOMs yield values that can vary widely among the candidate topologies for a given set of assumed values for key variables (e.g., module failure rate, single-point failure rate, repair rate, etc.). Closer inspections of the results yielded a number of valuable insights into the factors that cause FoM values to either rise or fall compared to those of other candidate topologies.
- The presented case study generated results that support key observations about the ability of modularized motor drives combined with rapid repair and suppression of single-point failures to

significantly boost system MTTF values, offering promise for closing the identified electrified aircraft reliability gap.

6.2 Closing Remarks and Next Steps

This investigation, combined with the results of the study that preceded it, has provided strong evidence that fault-tolerant modular motor drives represent a powerful architecture for addressing the daunting reliability gap that electric aircraft propulsor drives are facing based on the best conventional motor drive technology that is available today. It is extremely unlikely that improvements in the reliability and robustness of power electronics and electric machine components alone will be sufficient to span the 10^5x gap between the MTTF values of today's best machine drive technology and the required MTTF values of electric propulsors drives needed for future electrically-powered wide-body aircraft. It is far more likely that redundancy and modularity will provide the key to ultimately spanning this reliability chasm, just as they have done for modern jet engines and flight control systems.

The results of this investigation summarized in the preceding section make a strong case for the promising future of FT-MMDs in future electrically-powered aircraft. In addition, these results provide the seeds of a technology development roadmap by identifying the key areas where further technical advances are required for this technology to achieve its full potential. The key components of this technology roadmap consist of:

- Continually improving the reliability and robustness of power electronics and electric machine technology to boost the reliability characteristics of the individual motor drive modules as high a possible using a highly multi-disciplinary approach that addresses all of the power electronics and machine components
- Aggressively pursuing new techniques and topologies for designing electric machines and power electronics that exhibit natural advantages for avoiding dangerous fault modes and, if faults occur, minimize their impact on post-fault behavior in order to assure that all faults are safely contained.
- Investing in the development of advanced technology for implementing robust distributed control of modular motor drives that makes it possible for each motor drive module to operate as independently as possible which maintaining an appropriate level of control coordination among the modules, as well as the ability to accurately detect and respond to internal control faults leading to its safe shutdown.
- Encouraging the development of advanced technology for rapidly detecting and diagnosing every known type of fault in electric machines and power electronics so that the correct steps can be taken as rapidly as possible to extinguish any fault that appears.
- Actively pursuing advances in the design of modular machines and power electronics that will make it as easy and convenient as possible for repair crews to replace any faulted modules between flights with minimal delays.
- Launching an aggressive technology development initiative to identify and, to the greatest possible extent, suppress every potential source of single-point failure in the FT-MMD system.

In summary, much has been done already to lay the groundwork for fault-tolerant modular motor drives, but there is still much to be done to insure its successful development and integration into future electrically-propelled aircraft. There is much to be gained from the successful development of FT-MMD technology that would benefit future aerospace vehicles, as well as a wide range of terrestrial applications. We believe that NASA is in a strong position to spearhead the development of this critical technology that would benefit such a wide range of stakeholders in the industrial, commercial, transportation, and defense communities.

References

1. P.R. Darmstadt et al., “Hazards Analysis and Failure Modes and Effects Criticality Analysis (FMECA) of Four Concept Vehicle Propulsion Systems,” NASA Technical Report, 2019. [Online]. Available: https://ntrs.nasa.gov/api/citations/20190026443/downloads/20190026443.pdf?attachment=true
2. P.R. Darmstadt et al., “Reliability and Safety Assessment of Urban Air Mobility Concept Vehicles,” NASA Technical Report, 2021. [Online]. Available: https://ntrs.nasa.gov/api/citations/20210017188/downloads/1540_Boeing%20NASA%3ACR-20210017188_FINAL_013122.pdf?attachment=true
3. U.S. Department of Transportation Federal Aviation Administration, “System Design and Analysis,” FAA Advisory Circular AC, No. 25. 1309-1A. 1988.
4. J.A. Swanke and T.M. Jahns, “Design and Reliability Analysis of a Fault-Tolerant Integrated Motor Drive for a Quadrotor Urban Air Mobility (UAM) Aircraft,” Project Report, NASA, submitted March 2021.
5. N. Simpson, R. Wrobel, and P. H. Mellor, “Estimation of Equivalent Thermal Parameters of Impregnated Electrical Windings,” IEEE Trans. Ind. Appl., vol. 49, no. 6, pp. 2505–2515, Nov. 2013, doi: 10.1109/TIA.2013.2263271.
6. C. Lai, B. Aiswarya, B. Vicki, K. Lakshmi Varaha Iyer, and N. C. Kar, “Analysis of stator winding inter-turn short-circuit fault in interior and surface mounted permanent magnet traction machines,” 2014 IEEE Transp. Electrif. Conf. Expo Components, Syst. Power Electron. - From Technol. to Bus. Public Policy, ITEC 2014, pp. 1–6, 2014, doi: 10.1109/itec.2014.6861775.
7. J.G. Cintron-Rivera, S.N. Foste, and E.G. Strangas, “Mitigation of turn-to-turn faults in fault tolerant permanent magnet synchronous motors,” IEEE Trans. Energy Convers., vol. 30, no. 2, pp. 465–475, 2015, doi: 10.1109/TEC.2014.2360813.
8. C. Gerada, K. Bradley, and M. Sumner, “Winding turn-to-turn faults in permanent magnet synchronous machine drives,” Conf. Rec. - IAS Annu. Meet. (IEEE Ind. Appl. Soc.), vol. 2, pp. 1029–1036, 2005, doi: 10.1109/IAS.2005.1518481.
9. S. Foitzik and M. Doppelbauer, “Analytical model of a six-phase PMSM for the simulation of stator winding faults on turn level,” 2019 IEEE Int. Electr. Mach. Drives Conf. IEMDC 2019, pp. 185–191, 2019, doi: 10.1109/IEMDC.2019.8785351.
10. P.E. Castro Palavicino, “Analysis , Modeling , and Detection of Inter-Turn Short Circuits in Interior Permanent Magnet Synchronous Machines by,” PhD Thesis, Dept. of Electrical & Computer Engr., University of Wisconsin-Madison, 2021.
11. S. Lee, F. Chen, T.M. Jahns, and B. Sarlioglu, “Review on Switching Device Fault, Protection, and Fault-Tolerant Topologies of Current Source Inverter,” in 2021 IEEE 13th International Symposium on Diagnostics for Electrical Machines, Power Electronics and Drives (SDEMPED), Aug. 2021, pp. 489–495. doi: 10.1109/SDEMPED51010.2021.9605513.
12. Y. Zhang, W. Zhang, and T. M. Jahns, “Investigation of single-switch short-circuit fault characteristics of a PM machine drive with a current source inverter,” 2015 IEEE International Electric Machines & Drives Conference (IEMDC), Coeur d'Alene, ID, USA, 2015, pp. 967–973, doi: 10.1109/IEMDC.2015.7409178.
13. H. Dai, “Investigation of Current Source Inverter using Wide Bandgap Devices for Integrated Motor Drive Applications,” PhD Thesis, Dept. of Electrical & Computer Engr., University of Wisconsin-Madison, 2021.

14. ARPA-E, “Aviation Class Synergistically Cooled Electric Motors with Integrated Drives (ASCEND) Funding Opportunity Announcement (FOA) No. DE-FOA-0002238,” 2019. [Online]. Available: https://arpa-e-foa.energy.gov/Default.aspx?foaId=22888746-6728-479a-8b27-f53f97f587a9
15. J.A. Swanke, D. Bobba, T.M. Jahns and B. Sarlioglu, “Design of High-Speed Permanent Magnet Machine for Aerospace Propulsion,” 2019 AIAA/IEEE Electric Aircraft Technologies Symposium (EATS), Indianapolis, IN, USA, 2019, pp. 1-12, doi: 10.2514/6.2019-4483.
16. M.C. Kulan, S. Sahin, and N.J. Baker, “An Overview of Modern Thermo-Conductive Materials for Heat Extraction in Electrical Machines,” IEEE Access, vol. 8, pp. 212114–212129, 2020, doi: 10.1109/ACCESS.2020.3040045.
17. D. Bobba et al., “Multi-Physics Based Analysis and Design of Stator Coil in High Power Density PMSM for Aircraft Propulsion Applications,” 2021 AIAA/IEEE Electric Aircraft Technologies Symposium (EATS), Denver, CO, USA, 2021, pp. 1–9, doi: 10.23919/EATS52162.2021.9704820.
18. J.E. Cousineau et al., “Characterization of Contact and Bulk Thermal Resistance of Laminations for Electric Machines,” Technical Report, US National Renewable Energy Laboratory, Report No. NREL/TP-5400-63887, June, 2015.
19. T. Mulholland, R. Felber, and N. Rudolph, “Design and additive manufacturing of a composite crossflow heat exchanger,” in Solid Freeform Fabrication 2017: Proceedings of the 28th Annual International Solid Freeform Fabrication Symposium - An Additive Manufacturing Conference, SFF 2017, 2020, pp. 2641–2649.
20. G. Nellis and S. Klein, Heat Transfer. Cambridge University Press, 2012.
21. N. Bianchi, M.D. Pre, and S. Bolognani, “Design of a Fault-Tolerant IPM Motor for Electric Power Steering,” IEEE Trans. Veh. Technol., vol. 55, no. 4, pp. 1102–1111, Jul. 2006, doi: 10.1109/TVT.2006.877716.
22. T.A. Lipo, Introduction To AC Machine Design, 3rd ed. Wisconsin Power Electronics Research Center, University of Wisconsin, 2016.
23. B.J. Baliga, “Power semiconductor device figure of merit for high-frequency applications,” IEEE Electron Device Lett., no. 10, pp. 455–457, Oct. 1989, doi: 10.1109/55.43098.
24. W. Sung, K. Han, and B.J. Baliga, “Optimization of the JFET region of 1.2kV SiC MOSFETs for improved high frequency figure of merit (HF-FOM),” in 2017 IEEE 5th Workshop on Wide Bandgap Power Devices and Applications (WiPDA), Oct. 2017, vol. 31, no. 7, pp. 238–241. doi: 10.1109/WiPDA.2017.8170553.
25. B.A. Welchko, T.A. Lipo, T.M. Jahns, and S.E. Schulz, “Fault Tolerant Three-Phase AC Motor Drive Topologies: A Comparison of Features, Cost, and Limitations,” IEEE Trans. Power Electron., vol. 19, no. 4, pp. 1108–1116, Jul. 2004, doi: 10.1109/TPEL.2004.830074.
26. R.P. Heydorn and P.D.T. O’Connor, Practical Reliability Engineering, no. 4. 2011.
27. C. Carlson, Effective FMEAs: Achieving Safe, Reliable, and Economical Products and Processes Using Failure Mode and Effects Analysis. Hoboken, New Jersey: John Wiley & Sons, Inc., 2012.
28. J. Borcsok, E. Ugljesa, and D. Machmur, “Calculation of MTTF values with Markov Models for Safety Instrumented Systems,” in 7th WSEAS International Conference on APPLIED COMPUTER SCIENCE, 2007, pp. 30–35.
29. J.A. Swanke and T.M. Jahns, “Reliability Analysis of a Fault-Tolerant Integrated Modular Motor Drive for an Urban Air Mobility Aircraft Using Markov Chains,” IEEE Trans. Transp. Electrif., vol. 8, no. 4, pp. 4523–4533, Dec. 2022, doi: 10.1109/TTE.2022.3183933.
30. MIL-HDBK-217F - Military Handbook: Reliability Prediction of Electronic Equipment. 1991.